

DRAFT VERSION APRIL 2, 2019
 Typeset using L^AT_EX **preprint** style in AASTeX62

Do *Kepler* superflare stars really include slowly-rotating Sun-like stars ?

- Results using APO 3.5m telescope spectroscopic observations and *Gaia*-DR2 data -

YUTA NOTSU,^{1, 2,*} HIROYUKI MAEHARA,^{3, 4} SATOSHI HONDA,⁵ SUZANNE L. HAWLEY,⁶
 JAMES R. A. DAVENPORT,⁶ KOSUKE NAMEKATA,^{1, †} SHOTA NOTSU,^{1, 7,*} KAI IKUTA,¹
 DAISAKU NOGAMI,¹ AND KAZUNARI SHIBATA⁸

¹*Department of Astronomy, Kyoto University, Sakyo, Kyoto 606-8502, Japan*

²*Laboratory for Atmospheric and Space Physics, University of Colorado Boulder, 3665 Discovery Drive, Boulder, CO 80303, USA*

³*Okayama Branch Office, Subaru Telescope, National Astronomical Observatory of Japan, NINS, Kamogata, Asakuchi, Okayama 719-0232, Japan*

⁴*Okayama Observatory, Kyoto University, Kamogata, Asakuchi, Okayama 719-0232, Japan*

⁵*Nishi-Harima Astronomical Observatory, Center for Astronomy, University of Hyogo, Sayo, Hyogo 679-5313, Japan*

⁶*Department of Astronomy, University of Washington, Seattle, WA 98195, USA*

⁷*Leiden Observatory, Leiden University, P.O. Box 9513, 2300 RA Leiden, The Netherlands*

⁸*Astronomical Observatory, Kyoto University, Sakyo, Kyoto 606-8502, Japan*

(Received 12-11-2018; Revised; Accepted 03-29-2019)

ABSTRACT

We report the latest view of *Kepler* solar-type (G-type main-sequence) superflare stars, including recent updates with Apache Point Observatory (APO) 3.5m telescope spectroscopic observations and *Gaia*-DR2 data. First, we newly conducted APO3.5m spectroscopic observations of 18 superflare stars found from *Kepler* 1-min time cadence data. More than half (43 stars) are confirmed to be “single” stars, among 64 superflare stars in total that have been spectroscopically investigated so far in this APO3.5m and our previous Subaru/HDS observations. The measurements of $v \sin i$ (projected rotational velocity) and chromospheric lines (Ca II H&K and Ca II 8542Å) support the brightness variation of superflare stars is caused by the rotation of a star with large starspots. We then investigated the statistical properties of *Kepler* solar-type superflare stars by incorporating *Gaia*-DR2 stellar radius estimates. As a result, the maximum superflare energy continuously decreases as the rotation period P_{rot} increases. Superflares with energies $\lesssim 5 \times 10^{34}$ erg occur on old, slowly-rotating Sun-like stars ($P_{\text{rot}} \sim 25$ days) approximately once every 2000–3000 years, while young rapidly-rotating stars with $P_{\text{rot}} \sim$ a few days have superflares up to 10^{36} erg. The maximum starspot area does not depend on the rotation period when the star is young, but as the rotation slows down, it starts to steeply decrease at $P_{\text{rot}} \gtrsim 12$ days for Sun-like stars. These two decreasing trends are consistent since the magnetic energy stored around starspots

Corresponding author: Yuta Notsu
 ynotsu@kwasan.kyoto-u.ac.jp

explains the flare energy, but other factors like spot magnetic structure should also be considered.

Keywords: stars: flare – stars: activity – stars: starspots – stars: rotation – stars: solar-type – stars: abundances

1. INTRODUCTION

Flares are energetic explosions in the stellar atmosphere, and are thought to occur by intense releases of magnetic energy stored around starspots (e.g., [Shibata & Magara 2011](#)). Not only the Sun, but also many stars are known to show stellar magnetic activity including flares. In particular, young rapidly-rotating stars, close binary stars, and dMe stars tend to show high magnetic activity levels, and magnetic fields of a few kG are considered to be distributed in large regions on the stellar surface (e.g., [Gershberg 2005](#); [Reid & Hawley 2005](#); [Benz & Güdel 2010](#); [Kowalski et al. 2010](#); [Osten et al. 2016](#)). They frequently have “superflares”, which have a total bolometric energy $10 - 10^6$ times more energetic ($\sim 10^{33-38}$ erg; [Schaefer et al. 2000](#)) than the largest solar flares ($\sim 10^{32}$ erg; [Emslie et al. 2012](#)). In contrast, the Sun rotates slowly ($P_{\text{rot}} \sim 25$ days) and the mean magnetic field is weak (a few Gauss). Thus it has been thought that slowly-rotating Sun-like stars basically do not have high magnetic activity events like superflares.

Recently, however, many superflares on solar-type (G-type main-sequence) stars have been reported ([Maehara et al. 2012&2015](#); [Shibayama et al. 2013](#); [Candelaresi et al. 2014](#); [Wu et al. 2015](#); [Balona 2015](#); [Davenport 2016](#); [Van Doorsselaere et al. 2017](#)) by using the high-precision photometric data of the *Kepler* space telescope ([Koch et al. 2010](#)) ¹ ². The analyses of *Kepler* data enabled us to discuss statistical properties of superflares since a large number of flare events were discovered. The frequency-energy distribution of superflares on solar-type stars shows a power-law distribution $dN/dE \approx E^\alpha$ with the index $\alpha = (-1.5) - (-1.9)$, and this distribution is consistent with that of solar flares ([Maehara et al. 2012](#); [Shibayama et al. 2013](#); [Maehara et al. 2015](#)). Many superflare stars show quasi-periodic brightness variations with a typical period of from one day to a few tens of days and a typical amplitude of 0.1% – 10%. They are assumed to be explained by the rotation of the star with fairly large starspots ([Notsu et al. 2013b](#)), and the starspot size A_{spot} and rotation period P_{rot} values can be estimated from these brightness variations.

Using these A_{spot} values, we confirmed that the superflare energy is related to the total coverage of the starspots, and that the superflare energy can be explained by the magnetic energy stored around these large starspots ([Shibata et al. 2013](#); [Notsu et al. 2013b](#)). We then found that energetic superflares with energy up to 10^{35} erg could occur on stars rotating as slowly as the Sun ($P_{\text{rot}} \sim 25$ days), even though the frequency is low (once in a few thousand years), compared with rapidly-rotating stars ([Notsu et al. 2013b](#)). We also investigated statistical properties of starspots in relation to superflare studies, and suggested that superflare events are well characterized by the existence of large starspots and the occurrence frequency of large starspots are also consistent with that of

* JSPS Research Fellow DC1 (until March 31, 2019)

JSPS Overseas Research Fellow (from April 1, 2019)

[†] JSPS Research Fellow DC1

¹ We note here for reference that superflares on solar-type stars have been recently reported not only with *Kepler* but also with X-ray space telescope observations (e.g., [Pye et al. 2015](#)) and ground-based photometric observations (e.g., [Jackman et al. 2018](#)), though currently the number of observed events are much smaller than the *Kepler* results.

² We also note here that now there are many flare studies using *Kepler* (and *K2*) data not only for solar-type stars discussed in this study, but also for the other spectral-type stars such as K, M-dwarfs (e.g., [Walkowicz et al. 2011](#); [Hawley et al. 2014](#); [Candelaresi et al. 2014](#); [Ramsay & Doyle 2015](#) [Davenport 2016](#); [Van Doorsselaere et al. 2017](#); [Yang et al. 2017](#); [Chang et al. 2018](#)) and brown dwarfs (e.g., [Gizis et al. 2013](#); [Paudel et al. 2018](#)).

sunspots (Maehara et al. 2017). In addition, we suggested that the Sun can generate a large magnetic flux that is sufficient for causing superflares on the basis of theoretical estimates (Shibata et al. 2013). It is becoming important to find out the maximum size of starspots and superflares that can be generated on Sun-like stars, not only in solar and stellar physics (e.g., Aulanier et al. 2013; Shibata et al. 2013; Toriumi et al. 2017; Katsova et al. 2018; Schmieder 2018), but also in solar-terrestrial physics and even exoplanet studies. For example, extreme space weather events and their effects on our society (Royal Academy of Engineering 2013; Tsurutani & Lakhina 2014; Hudson 2015; Schrijver 2015; Takahashi et al. 2016; Eastwood et al. 2017; Riley et al. 2018), a history of solar activity over \sim 1000 years (e.g., Miyake et al. 2012&2013; Hayakawa et al. 2017a&2017b; Usoskin 2017), and a potential habitability of various planets (e.g., Segura et al. 2010; Airapetian et al. 2016; Atri 2017; Lingam & Loeb 2017).

The results of *Kepler* described here are now also supported from spectroscopic studies. We have observed 50 solar-type superflare stars using Subaru/HDS (Notsu et al. 2013a, 2015a, & 2015b; Nogami et al. 2014; Honda et al. 2015). We found that more than half (34 stars) of the 50 targets have no obvious evidence of being in a binary system, and the stellar atmospheric parameters (temperature, surface gravity, and metallicity) of these stars are in the range of those for ordinary solar-type stars (Notsu et al. 2015a). More importantly, Notsu et al. (2015b) supported the above interpretation that the quasi-periodic brightness variations of superflare stars are explained by the rotation of a star with large starspots, by measuring $v \sin i$ (projected rotational velocity) and the intensity of the Ca II 8542Å line. The existence of large starspots on superflare stars was further supported by Karoff et al. (2016) using Ca II H&K data from LAMOST telescope low-dispersion spectra. We also conducted lithium (Li) abundance analysis of these superflare stars (Honda et al. 2015). Li abundance is known to be a clue for investigating the stellar age (e.g., Skumanich 1972; Takeda et al. 2010). Many of the superflare stars tend to show high Li abundance, which are also consistent with Wichmann et al. (2014), but there are some objects that have low Li abundance and rotate slowly.

These results from our previous spectroscopic observations support that even old slowly-rotating stars similar to the Sun can have large starspots and superflares. However, more spectroscopic observations are still needed for the following reasons: Among \sim 300 solar-type superflare stars found from *Kepler* data, only 34 stars (\sim 10%) have been confirmed to be single solar-type stars. This means that as for the remaining \sim 90% of the 300 solar-type stars, the statistical studies on superflares using *Kepler* data are not established in a strict sense. In particular, the number of superflare stars rotating as slowly as the Sun ($P_{\text{rot}} \sim$ 25 days) that were spectroscopically investigated is only a few in the above previous studies, and are not enough for considering whether the Sun can have superflares on the basis of spectroscopic data.

In this study, we have conducted new spectroscopic observations of solar-type superflare stars that were found from *Kepler* 1-min cadence data (Maehara et al. 2015). In this new study, we used the Echelle Spectrograph of the Apache Point Observatory (APO) 3.5m telescope. This spectrograph has a wavelength coverage of 3200-10000Å, which enabled us to take both Ca II H&K (3968 & 3934Å) and Ca II 8542Å lines simultaneously. In the first half of this paper (Sections 2, 3, and 4), we report the results of these new spectroscopic observations. We describe the selection of the target stars and the details of our observations in Section 2. In Section 3 (and Appendix A), we check the binarity of the targets, and then estimate various stellar parameters on the basis of the spectroscopic data. In Section 4, we comment on the estimated stellar parameters including Li abundances, and

discuss rotational velocity and chromospheric activities comparing with the quasi-periodic brightness variations of *Kepler* data.

The recent *Gaia*-DR2 stellar radius data (e.g., Berger et al. 2018) have suggested the possibility of severe contaminations of subgiant stars in the classification of *Kepler* solar-type (G-type main-sequence) stars used for the statistical studies of superflares described in the above. The classification of solar-type stars in our previous studies (Shibayama et al. 2013 and Maehara et al. 2015) were based on T_{eff} and $\log g$ values from the *Kepler* Input Catalog (KIC) (Brown et al. 2011; Huber et al. 2014). However, most of those T_{eff} and $\log g$ values are based on photometric methods (see Brown et al. 2011 and Huber et al. 2014 for the details), and there can be large differences between the real and catalog values. For example, Brown et al. (2011) reported uncertainties of T_{eff} and $\log g$ in the initial KIC are ± 200 K and 0.4 dex, respectively. There can be a severe contamination of subgiant stars in the sample of solar-type superflare stars in our previous studies. In a strict sense, we cannot even deny an extreme possibility that all of the slowly-rotating Sun-like superflare stars in our previous studies were the results of contaminations of subgiant stars. In addition, the *Kepler* solar-type superflare stars discussed in our previous studies can include some number of binary stars. This is a problem especially for investigating whether even truly Sun-like single stars can have large superflares or not. On the basis of these current situations, in Section 5, we investigate the statistical properties of *Kepler* solar-type superflare stars originally described in our previous studies (Maehara et al. 2012, 2015, & 2017; Shibayama et al. 2013; Notsu et al. 2013b), now incorporating *Gaia*-DR2 stellar radius estimates (reported in Berger et al. 2018) and the results of our new spectroscopic observations (Subaru and APO3.5m observations).

Finally in Sections 6.1 – 6.2, we summarize the latest view of superflares on solar-type stars found from our series of studies using *Kepler* data, by including the recent updates using Apache Point Observatory (APO) 3.5m telescope spectroscopic observations and *Gaia*-DR2 data. We also mention implications for future studies in Section 6.3.

2. APO 3.5M SPECTROSCOPIC OBSERVATIONS AND DATA REDUCTION

As target stars of our new spectroscopic observations, we selected all the 23 solar-type superflare stars reported in Maehara et al. (2015) on the basis of *Kepler* 1-min time cadence data. The names of these 23 stars and their stellar parameters are listed in Table 1. 18 stars among these 23 stars are identified in Berger et al. (2018), which is the catalog combining parallaxes from *Gaia* Data Release 2 (*Gaia*-DR2) with DR25 *Kepler* Stellar Properties Catalog (KSPC) (Mathur et al. 2017). We note that there are no slowly-rotating stars with their rotation period P_{rot} longer than 20 days in these 23 target stars since no superflare stars with $P_{\text{rot}} > 20$ days were reported in Maehara et al. (2015). That might be related with the fact that the fraction of slowly-rotating stars is smaller in the *Kepler* 1-min cadence data compared with the long cadence data because of the initial target selection and observation time allocation of *Kepler* (See the second paragraph of page 5 of Maehara et al. 2015 for the details).

Table 1. Basic data of our target superflare stars.

Star name	Binarity ^a	$P_{\text{rot}}^{\text{b}}$ (d)	$N_{\text{flare}}^{\text{b}}$	K_p^{c} (mag)	$T_{\text{eff},\text{DR25}}^{\text{c}}$ (K)	$(\log g)_{\text{DR25}}^{\text{c}}$ (cm s ⁻²)	$[{\text{Fe/H}}]_{\text{DR25}}^{\text{c}}$	$R_{\text{DR25}}^{\text{c}}$ (R_{\odot})	$d_{\text{Gaia}}^{\text{d}}$ (pc)	$R_{\text{Gaia}}^{\text{d}}$ (R_{\odot})	EvoFlg ^e	BinFlg ^e
KIC10532461	no	7.14	1	8.8	5689^{+189}_{-172}	$4.24^{+0.26}_{-0.19}$	$-0.28^{+0.30}_{-0.25}$	$1.15^{+0.37}_{-0.34}$	$45.8^{+0.1}_{-0.1}$	$0.78^{+0.06}_{-0.05}$	0	0
KIC11652870	no	8.54	1	9.1	5516^{+149}_{-149}	$4.37^{+0.19}_{-0.19}$	$-0.16^{+0.30}_{-0.30}$	$0.98^{+0.27}_{-0.18}$	$51.6^{+0.1}_{-0.1}$	$0.78^{+0.06}_{-0.05}$	0	0
KIC9139151	no	6.15	2	9.2	6299^{+62}_{-81}	$4.38^{+0.01}_{-0.01}$	$0.08^{+0.10}_{-0.15}$	$1.17^{+0.03}_{-0.04}$	$102.7^{+0.3}_{-0.3}$	$1.14^{+0.05}_{-0.05}$	0	0
KIC4554830	no	7.73	1	10.3	5666^{+76}_{-76}	$4.16^{+0.01}_{-0.01}$	$0.36^{+0.10}_{-0.15}$	$1.43^{+0.07}_{-0.05}$	$173.4^{+0.7}_{-0.7}$	$1.44^{+0.06}_{-0.06}$	1	0
KIC474236 ^{f,g}	no	2.34	1	10.6	5914^{+163}_{-133}	$4.11^{+0.33}_{-0.14}$	$-0.70^{+0.35}_{-0.20}$	$1.30^{+0.28}_{-0.42}$	—	—	—	—
KIC4831454 ^f	no	5.19	8	10.7	5479^{+146}_{-146}	$4.60^{+0.05}_{-0.11}$	$-0.46^{+0.30}_{-0.30}$	$0.74^{+0.13}_{-0.06}$	$123.8^{+0.4}_{-0.4}$	$0.91^{+0.07}_{-0.06}$	0	0
KIC8656342	no	17.50	2	10.9	5959^{+80}_{-80}	$4.07^{+0.03}_{-0.03}$	$-0.02^{+0.20}_{-0.15}$	$1.59^{+0.10}_{-0.09}$	$299.8^{+2.4}_{-2.4}$	$1.70^{+0.07}_{-0.07}$	1	0
KIC9652680 ^f	no	1.47	7	11.2	5819^{+131}_{-160}	$4.57^{+0.03}_{-0.17}$	$-0.32^{+0.30}_{-0.30}$	$0.82^{+0.20}_{-0.07}$	$220.2^{+1.1}_{-1.1}$	$1.09^{+0.08}_{-0.07}$	0	0
KIC6777146	no	7.21	1	11.3	6103^{+169}_{-169}	$4.34^{+0.15}_{-0.13}$	$-0.56^{+0.30}_{-0.30}$	$1.04^{+0.19}_{-0.19}$	$331.6^{+2.9}_{-2.9}$	$1.60^{+0.12}_{-0.11}$	1	0
KIC8508009	no	2.95	1	11.5	6256^{+156}_{-188}	$4.37^{+0.09}_{-0.14}$	$-0.26^{+0.25}_{-0.30}$	$1.09^{+0.24}_{-0.15}$	$285.9^{+1.8}_{-1.8}$	$1.15^{+0.09}_{-0.08}$	0	0
KIC11610797 ^f	no	1.62	8	11.5	5868^{+78}_{-78}	$4.03^{+0.20}_{-0.09}$	$-0.02^{+0.15}_{-0.15}$	$1.67^{+0.27}_{-0.40}$	$277.1^{+1.6}_{-1.6}$	$1.17^{+0.05}_{-0.05}$	0	0
KIC1123827	no	13.40	2	11.9	5593^{+111}_{-111}	$4.45^{+0.07}_{-0.10}$	$0.02^{+0.15}_{-0.15}$	$0.95^{+0.12}_{-0.08}$	$223.7^{+1.8}_{-1.8}$	$0.90^{+0.04}_{-0.04}$	0	0
KIC6291837	no	14.30	1	12.4	6212^{+111}_{-136}	$4.31^{+0.10}_{-0.12}$	$-0.04^{+0.15}_{-0.15}$	$1.21^{+0.21}_{-0.14}$	$523.2^{+15.8}_{-14.9}$	$1.42^{+0.07}_{-0.07}$	0	0
KIC11551430 ^g	RV(+VB)	4.26	89	10.7	5648^{+113}_{-90}	$4.02^{+0.22}_{-0.11}$	$-0.08^{+0.15}_{-0.10}$	$1.61^{+0.30}_{-0.30}$	—	—	—	—
KIC4543412	RV	2.16	13	11.2	5472^{+163}_{-147}	$4.44^{+0.14}_{-0.25}$	$-0.30^{+0.30}_{-0.30}$	$0.88^{+0.24}_{-0.14}$	$148.2^{+0.6}_{-0.6}$	$0.96^{+0.07}_{-0.06}$	0	0
KIC11128041	SB2+RV	7.36	2	10.8	5913^{+133}_{-162}	$4.58^{+0.03}_{-0.14}$	$-0.50^{+0.25}_{-0.30}$	$0.80^{+0.16}_{-0.06}$	$196.5^{+0.8}_{-0.8}$	$1.21^{+0.09}_{-0.08}$	0	0
KIC10338279 ^g	SB2	6.53	4	12.0	5615^{+152}_{-152}	$4.48^{+0.10}_{-0.14}$	$-0.44^{+0.30}_{-0.30}$	$0.84^{+0.19}_{-0.10}$	—	—	—	—
KIC7093428 ^g	VB	0.51	19	11.0	6181^{+167}_{-223}	$2.77^{+0.54}_{-0.18}$	$0.07^{+0.25}_{-0.25}$	$12.27^{+1.29}_{-7.32}$	—	—	—	—
KIC6032920 ^g	—	3.16	6	13.5	5862^{+141}_{-159}	$4.58^{+0.03}_{-0.18}$	$-0.52^{+0.30}_{-0.30}$	$0.79^{+0.21}_{-0.07}$	—	—	—	—
KIC10528093	—	12.20	2	13.6	5334^{+159}_{-143}	$4.54^{+0.10}_{-0.07}$	$-0.54^{+0.35}_{-0.30}$	$0.75^{+0.08}_{-0.08}$	$1497.0^{+37.3}_{-35.6}$	$3.34^{+0.26}_{-0.24}$	1	0
KIC10646889	—	4.70	8	13.6	5674^{+152}_{-152}	$4.44^{+0.13}_{-0.13}$	$-0.36^{+0.30}_{-0.30}$	$0.90^{+0.23}_{-0.23}$	$716.1^{+7.1}_{-7.0}$	$1.35^{+0.10}_{-0.09}$	0	0
KIC9655134	—	15.50	1	13.6	5397^{+160}_{-160}	$4.55^{+0.09}_{-0.07}$	$-0.66^{+0.35}_{-0.30}$	$0.73^{+0.08}_{-0.08}$	$457.6^{+4.3}_{-4.2}$	$0.93^{+0.07}_{-0.06}$	0	0
KIC10745663	—	3.13	7	14.3	6014^{+162}_{-198}	$4.49^{+0.05}_{-0.05}$	$-0.08^{+0.25}_{-0.21}$	$0.96^{+0.30}_{-0.35}$	$1480.6^{+38.0}_{-36.3}$	$1.82^{+0.14}_{-0.13}$	1	0

Table 1 continued on next page

Table 1 (*continued*)

Star name	Binarity ^a	P_{rot} ^b (d)	N_{flare} ^b (d)	K_p ^c (mag)	$T_{\text{eff,DR25}}$ ^c (K)	$(\log g)_{\text{DR25}}$ ^c (cm s ⁻²)	[Fe/H] _{DR25} ^c (R_\odot)	R_{DR25} ^c (R_\odot)	d_{Gaia} ^d (pc)	R_{Gaia} ^d (R_\odot)	EvoFlg ^e	BinFlg ^e
-----------	-----------------------	--------------------------------------	--	-----------------------------	---	--	--	---	--	---	---------------------	---------------------

a For the details of this column, see Appendix A.1. “no” means that the star show no evidence of being in a binary system. “SB2” corresponds to stars that have double-lined profile. “RV” means that the star shows radial velocity changes. “VB” means that the star has visual companion stars. The bottom five stars (KIC6032920, KIC10528093, KIC10646889, KIC9655134, and KIC10745663) are much fainter compared with the other target stars. The data quality of our spectroscopic data for four of them (KIC6032920, KIC10528093, KIC10646889, and KIC9655134) are not enough to judge whether they show any evidence of binary system. As for the faintest KIC10745663, we have no spectroscopic data.

b Stellar rotation period (P_{rot}) and number of superflares (N_{flare}) reported in Maehara et al. (2015).

c *Kepler* band magnitude (K_p), effective temperature ($T_{\text{eff,DR25}}$), surface gravity ($\log g$)_{DR25}, metallicity ([Fe/H])_{DR25}, and stellar radius (R_{DR25}) in DR25 *Kepler* Stellar Properties Catalog (KSPC) (Mathur et al. 2017).

d Stellar distance (d_{Gaia}) and stellar radius (R_{Gaia}) in Berger et al. (2018). They derived these values by combining parallaxes from *Gaia* Data Release 2 with the DR25 KSPC.

e Evolutionary Flag (EvoFlg) and Binary Flag (BinFlg) reported in Berger et al. (2018), on the basis of R_{Gaia} values. The evolutionary flags are as follows: 0 = main-sequence dwarf and 1 = subgiant. The binary flags are as follows: 0 = no indication of binary, 1 = binary candidate based on R_{Gaia} only, 2 = AO-detected binary only (Ziegler et al. 2018), and 3 = binary candidate based on R_{Gaia} and AO-detected binary.

f As described in Appendix A.1, we have also conducted spectroscopic observations of these four stars (KIC4742436, KIC4831454, KIC9652680, and KIC11610797) using Subaru telescope (Notsu et al. 2015a & 2015b; Honda et al. 2015).

g As for these five stars (KIC4742436, KIC11551430, KIC10338279, KIC7093428, and KIC6032920), there are no d_{Gaia} and R_{Gaia} values reported in Berger et al. (2018).

Our new spectroscopic observations were carried out by using the ARC Echelle Spectrograph (ARCES: Wang et al. 2003) attached to the ARC 3.5 m Telescope at Apache Point Observatory (APO). The wavelength resolution ($R = \lambda/\Delta\lambda$) is $\sim 32,000$ and the spectral coverage is 3200-10000Å. Data reduction (bias subtraction, flat fielding, aperture determination, scattered light subtraction, spectral extraction, wavelength calibration, normalization by the continuum, and heliocentric radial velocity correction)³ was conducted using the ECHELLE package of the IRAF⁴ and PyRAF⁵ software.

For the process of wavelength calibration, we took exposures of a thorium-argon (Th-Ar) lamp at the start and end of each half night of observation. However, ARCES spectral data has some systematic drift on CCD over a few hours. This drift is most likely due to the thermal changes of the prisms with temperature, as described in Section 3.1 of Wang et al. (2003). This drift is a bit large in the early half night ($\sim 2 - 3 \text{ km s}^{-1}$) compared with that in the latter half night ($\lesssim 1-2 \text{ km s}^{-1}$). We remove this systematic drift by using the wavelength of ~ 10 telluric absorption lines around 6890-6910Å.

When we normalize the spectral orders around Ca II H&K lines (3968Å and 3934Å), as also done in Morris et al. (2017), we fit the spectrum of an early-type standard star with a high-order polynomial to measure the blaze function, and we then divide the spectra of target stars by the polynomial fit to normalize each spectral order. We use this method since there are many absorption lines in the blue part of the spectra, and it is difficult to directly fit the continuum component of spectra of the target stars. When normalizing red part of the spectra ($\gtrsim 5000\text{\AA}$), which we use for the estimations of stellar parameters (except for Ca II H&K line analyses) in this study, we directly fit the target star spectra with a high-order polynomial to measure the blaze function. After that, we shifted the normalized spectra in wavelength into the rest-frame by removing their radial velocities. We remove the radial velocity by maximizing the cross-correlation of our ARCES spectra with solar spectra in the wavelength range of 6212-6220Å, where we conduct $v \sin i$ measurements in Appendix A.4.

The observation date of each target superflare star and the obtained signal-to-noise ratio (S/N) are shown in Table 2. We selected 23 target superflare stars, and for the 18 brightest superflare stars, we obtained high enough signal-to-noise (S/N) data for scientific discussions in this paper. However, the other five stars (KIC6032920, KIC10528093, KIC10646889, KIC9655134, and KIC10745663) in the bottom of Table 1 are much fainter ($K_p \geq 13.5$ mag) compared with the other 18 relatively bright target stars ($K_p \leq 12.4$ mag). The data quality of our spectroscopic data for four of them (KIC6032920, KIC10528093, KIC10646889, and KIC9655134) are not enough for detailed scientific discussions in this paper. As for KIC10745663, we only took a slit viewer image, and we have no spectroscopic data since it is too faint ($K_p=14.3$ mag).

³ An ARCES data reduction manual by J. Thorburn is available at <http://astronomy.nmsu.edu:8000/apo-wiki/wiki/ARCES>.

⁴ IRAF is distributed by the National Optical Astronomy Observatories, which is operated by the Association of Universities for Research in Astronomy, Inc., under cooperative agreement with the National Science Foundation.

⁵ PyRAF is part of the stsci_python package of astronomical data analysis tools, and is a product of the Science Software Branch at the Space Telescope Science Institute.

Table 2. APO3.5m telescope observations of target superflare stars

Star name	Remarks ^a	Binarity ^b	date(UT) ^c	time(UT) ^c	RV ^d (km s ⁻¹)	S/N(8542) ^e	S/N(H α) ^e	S/N(HK) ^e
KIC10532461		no	2016-08-23	02:16:35.23	8.0	68	95	33
–		–	2017-04-10	08:11:00.28	8.3	68	97	22
–		–	2017-09-23	01:44:20.11	8.6	110	148	41
–		–	2017-10-31	02:01:19.03	8.5	27	36	9
–		–	comb	–	–	148	202	64
KIC11652870		no	2016-08-21	04:53:17.80	-3.9	49	68	25
–		–	2017-04-10	08:33:38.85	-3.5	70	99	26
–		–	2017-10-15	01:34:58.94	-3.4	64	86	24
–		–	2017-10-29	03:47:57.35	-3.5	65	89	19
–		–	comb	–	–	124	172	54
KIC9139151		no	2017-04-10	08:57:09.20	-28.4	68	100	33
–		–	2017-06-05	10:53:45.74	-28.2	67	99	43
–		–	2017-10-29	03:32:52.19	-28.5	71	104	28
–		–	comb	–	–	118	175	71
KIC4554830		no	2017-04-10	09:24:50.91	-21.9	54	77	22
–		–	2017-09-23	02:11:54.20	-21.2	64	88	25
–		–	2017-10-03	05:32:26.76	-22.5	43	58	12
–		–	comb	–	–	93	130	38
KIC4742436		no	2017-04-10	11:54:08.11	-54.6	34	49	20
–	(1)	–	2012-08-07	06:46:04.8	-54.5	140	210	–
–	(1)	–	2012-08-08	06:04:19.2	-54.6	140	190	–
–	(1)	–	2012-08-09	06:50:24.0	-54	100	160	–
KIC4831454		no	2017-04-10	10:30:13.61	-27.4	45	63	21
–	(1)	–	2012-08-07	07:03:21.6	-26.4	150	220	–
–	(1)	–	2012-08-08	06:21:36.0	-26.6	140	190	–
–	(1)	–	2012-08-09	07:12:00.0	-27.2	110	170	–
KIC8656342		no	2017-05-03	08:09:21.76	-4.1	49	70	21
–		–	2017-09-23	04:03:53.94	-4.6	25	34	11
–		–	2017-10-03	05:07:22.31	-4.3	45	62	19
–		–	comb	–	–	71	99	35
KIC9652680		no	2017-05-03	10:01:13.48	-20.5	43	61	23
–	(1)	–	2012-08-07	07:19:12.0	-21.6	110	170	–
–	(1)	–	2012-08-08	06:41:45.6	-20.5	90	150	–
–	(1)	–	2012-08-09	06:25:55.2	-22.3	90	140	–
KIC6777146		no	2017-05-03	10:34:00.37	-7.3	41	58	25
–		–	2017-10-03	01:51:57.37	-6.9	41	56	19

Table 2 continued on next page

Table 2 (*continued*)

Star name	Remarks ^a	Binarity ^b	date(UT) ^c	time(UT) ^c	RV ^d (km s ⁻¹)	S/N(8542) ^e	S/N(H α) ^e	S/N(HK) ^e
–		–	2017-10-29	03:07:44.74	-7.7	41	57	17
–		–	comb	–	–	71	99	42
KIC8508009		no	2017-05-03	11:06:38.23	-28.8	36	52	22
–		–	2017-10-03	02:24:30.58	-28.8	37	51	18
–		–	2017-10-07	06:30:24.29	-28.8	27	38	8
–		–	comb	–	–	58	81	34
KIC11610797		no	2017-06-05	07:42:39.45	-6.3	36	51	20
–	(1)	–	2012-08-07	08:32:38.4	-10.3	110	170	–
–	(1)	–	2012-08-08	07:17:45.6	-11.6	100	150	–
–	(1)	–	2012-08-09	07:58:04.8	-10.4	80	130	–
KIC11253827		no	2017-06-05	08:15:13.95	-13.6	32	44	16
–		–	2017-10-03	02:57:04.29	-13.5	32	44	13
–		–	2017-10-07	05:57:49.26	-14.1	26	35	7
–		–	comb	–	–	52	71	24
KIC6291837		no	2017-06-05	09:22:11.96	-34.5	34	50	23
–		–	2017-10-07	04:52:41.67	-36.7	22	31	8
–		–	comb	–	–	41	58	29
KIC11551430A	(2)	RV(+VB)	2017-04-10	11:03:00.04	-14.9	43	60	20
–		–	2017-09-23	02:46:47.94	5.4	53	71	21
–		–	2017-10-03	04:34:48.04	-54.0	53	72	20
–		–	comb	–	–	86	116	41
KIC11551430B	(2)	VB	2017-04-10	11:28:42.47	-25.5	11	16	4
KIC4543412		RV	2017-05-03	09:28:39.20	27.3	45	61	20
–		–	2017-09-23	06:28:58.19	7.6	24	31	4
–		–	2017-10-03	04:02:13.73	6.4	45	60	15
–		–	2017-10-07	05:25:15.88	-24.4	38	51	8
–		–	comb	–	–	78	103	31
KIC11128041		SB2+RV	2017-05-03	07:40:28.97	–	46	65	21
–		–	2017-09-23	03:19:21.25	–	42	57	18
–		–	2017-10-29	04:03:06.11	–	32	46	10
KIC10338279		SB2	2017-06-05	08:49:33.49	–	42	58	20
KIC7093428	(3)	VB	2017-05-03	08:56:03.72	-44.6	42	62	28
KIC6032920		–	2017-12-10	02:30:50.58	-58.3	14	21	low S/N
KIC10528093		–	2017-12-10	03:46:14.03	34.0	10	16	low S/N
KIC10646889		–	2017-12-10	03:10:31.49	-45.1	10	16	low S/N
KIC9655134		–	2017-12-10	04:20:18.10	-12.6	9	15	low S/N
KIC10745663		–	No-spectra	No-spectra	No-spectra	No-spectra	No-spectra	No-spectra

Table 2 continued on next page

Table 2 (*continued*)

Star name	Remarks ^a	Binarity ^b	date(UT) ^c	time(UT) ^c	RV ^d (km s ⁻¹)	S/N(8542) ^e	S/N(H α) ^e	S/N(H&K) ^e
-----------	----------------------	-----------------------	-----------------------	-----------------------	--	------------------------	-------------------------------	-----------------------

^a (1) As described in Appendix A.1, we also conducted spectroscopic observations of these four stars (KIC4742436, KIC4831454, KIC9652680, and KIC11610797) using Subaru telescope (Notsu et al. 2015a). RV values of these observations are included here for reference.

(2) KIC11551430 is found to be visual binary (KIC11551430A and KIC11551430B), as described in Appendix A.1. We took spectra of each component of visual binary separately, and measure parameters of each of them.

(3) As described in Appendix A.1, KIC7093428 has two fainter companion stars, and pixel data analyses suggest that flares occur on these companion stars. Since companion stars are faint, here we only measure parameters of the main (brightest) star for reference, though we do not use these values in the main discussion of this paper.

^b Same as in footnote *a* of Table 1. See also Appendix A.1.

^c Observation date (Universal Time) (format: YYYY-MM-DD) and middle time (Universal Time) (format: hh:mm:ss) of each exposure. “comb” corresponds to the co-added spectra that all APO spectra of each target star are combined into.

^d Radial velocity (See Appendix A.1).

^e Signal-to-noise ratio of the spectral data around Ca II 8542 Å(S/N(8542)), H α 6563Å(S/N(H α)), and Ca II H&K 3934/3938Å(S/N(H&K)).

In addition to the above 23 target superflare stars, we repeatedly observed 28 bright solar-type comparison stars as references of solar-type stars. The name and basic parameters of these 28 comparison stars, observation date, and S/N of each observation are listed in Table 3 (The original sources of these stars are in footnotes of Table 3). All of these 28 stars were also observed in California Planet Search (CPS) program (Isaacson & Fischer 2010), and we use these solar-type stars to calibrate Ca II H&K *S*-index in Appendix A.6.

Table 3. Observations of comparison stars to calibrate Ca II H&K *S*-index.

Star name	Remarks ^a	T_{eff} ^b	$B - V$ ^b	S_{MWO} ^c	date(UT) ^d	time(UT) ^d	$S/N(8542)^e$	$S/N(\text{HK})^e$	$r_0(8542)$	S_{APO}	S_{HK}	$\log \mathcal{F}_{\text{HK}}^+$ (erg/(cm ² s))	$\log R_{\text{HK}}^+$
HIP9519 ^e	(1)	5899	0.594	0.417	2016-11-07	08:01:15.75	134	64	0.50	0.0185	0.416	6.77	-4.07
-	-	-	-	-	2018-02-24	01:43:15.26	86	31	0.46	0.0167	0.376	6.71	-4.12
HIP19793 ^e	(1)	5833	0.620	0.347	2016-11-07	10:00:22.79	108	64	0.42	0.0165	0.372	6.66	-4.16
HIP21091 ^e	(1)	5857	0.601	0.352	2016-11-07	10:13:11.72	76	42	0.44	0.0163	0.367	6.69	-4.14
-	-	-	-	-	2018-01-05	08:29:18.26	102	21	0.44	0.0167	0.376	6.70	-4.12
HIP22175 ^e	(1)	5667	0.637	0.213	2016-11-07	10:55:47.00	116	58	0.26	0.0104	0.238	6.36	-4.41
-	-	-	-	-	2018-01-02	08:20:23.05	119	27	0.26	0.0104	0.238	6.36	-4.41
-	-	-	-	-	2018-02-24	02:18:39.39	278	37	0.26	0.0101	0.230	6.34	-4.43
HIP27980 ^e	(1)	5854	0.615	0.205	2016-11-07	10:53:12.14	105	58	0.23	0.0098	0.226	6.35	-4.48
-	-	-	-	-	2018-01-02	09:10:44.10	116	31	0.23	0.0091	0.208	6.29	-4.54
HIP35185 ^e	(1)	5830	0.601	0.341	2016-11-07	11:16:44.46	74	43	0.41	0.0150	0.338	6.64	-4.17
-	-	-	-	-	2018-01-02	10:09:19.57	97	35	0.41	0.0153	0.346	6.65	-4.16
-	-	-	-	-	2018-02-01	07:48:08.24	95	38	0.43	0.0157	0.354	6.67	-4.15
-	-	-	-	-	2018-04-30	02:31:36.03	70	31	0.43	0.0158	0.357	6.67	-4.14
HIP37971 ^e	(1)	5774	0.642	0.322	2016-11-07	11:28:03.37	69	38	0.38	0.0157	0.354	6.59	-4.20
-	-	-	-	-	2018-01-05	09:15:25.35	92	43	0.36	0.0148	0.334	6.56	-4.24
-	-	-	-	-	2018-04-30	02:44:36.92	77	36	0.39	0.0161	0.364	6.61	-4.19
HIP38228 ^e	(1)	5631	0.657	0.406	2016-11-07	11:37:22.49	117	65	0.45	0.0181	0.407	6.65	-4.10
-	-	-	-	-	2018-01-04	08:32:28.21	130	59	0.42	0.0164	0.370	6.60	-4.16
-	-	-	-	-	2018-01-05	09:05:22.10	137	63	0.44	0.0173	0.389	6.63	-4.13
-	-	-	-	-	2018-02-01	07:59:52.56	160	73	0.48	0.0186	0.418	6.67	-4.09
-	-	-	-	-	2018-04-30	02:55:31.81	109	49	0.42	0.0167	0.377	6.61	-4.14
HIP51652 ^e	(1)	5870	0.620	0.214	2016-11-07	12:12:29.36	72	33	0.25	0.0101	0.230	6.35	-4.48
-	-	-	-	-	2016-12-11	09:39:04.98	63	23	0.24	0.0099	0.226	6.33	-4.49
-	-	-	-	-	2018-01-05	11:09:21.87	102	50	0.24	0.0099	0.228	6.34	-4.49
HIP79068 ^e	(1)	5809	0.615	0.235	2016-12-11	12:53:01.25	52	25	0.28	0.0120	0.272	6.48	-4.33
-	-	-	-	-	2018-01-05	13:02:29.03	71	32	0.27	0.0109	0.248	6.42	-4.39
HIP117184 ^e	(1)	5890	0.609	0.354	2016-11-07	07:31:06.71	72	33	0.39	0.0153	0.346	6.64	-4.20
18Sco ^f	(2)	5794	0.618	0.170	2016-08-21	02:18:54.94	222	98	0.2	0.0074	0.172	6.13	-4.68
-	-	-	-	-	2016-08-23	02:00:15.72	198	102	0.23	0.0082	0.188	6.21	-4.60
-	-	-	-	-	2017-05-03	07:19:54.42	238	97	0.21	0.0082	0.190	6.21	-4.59

Table 3 continued on next page

Table 3 (*continued*)

Star name	Remarks ^a	$T_{\text{eff}}^{\text{b}}$ [K]	$B - V^{\text{b}}$	$S_{\text{MWO}}^{\text{c}}$	date(UT) ^d	time(UT) ^d	$S/\text{N}(\text{HK})^{\text{e}}$	$r_0(8542)$	S_{APO}	S_{HK}	$\log \mathcal{F}_{\text{HK}}^{+}$ (erg/(cm ² s))	$\log R_{\text{HK}}^{+}$	
59Vir ^f	(2)	6017	0.573	0.324	2017-04-10	07:23:42.69	90	52	0.4	0.0154	0.347	6.70	-4.17
-	-	-	-	-	2017-12-31	12:53:01.38	212	106	0.38	0.0144	0.326	6.66	-4.21
-	-	-	-	-	2018-01-02	12:55:35.66	134	64	0.39	0.0144	0.327	6.66	-4.21
61Vir ^f	(2)	5565	0.678	0.169	2017-04-10	07:31:23.31	107	41	0.21	0.0074	0.171	6.03	-4.70
HIP 100963 ^f	(2)	5751	0.620	0.227	2016-10-12	01:01:03.01	160	98	0.23	0.0085	0.195	6.24	-4.55
-	-	-	-	-	2016-10-14	00:52:57.66	170	106	0.26	0.0088	0.203	6.27	-4.52
-	-	-	-	-	2017-06-05	07:19:50.33	160	69	0.23	0.0087	0.200	6.26	-4.54
-	-	-	-	-	2017-10-03	01:17:15.01	154	71	0.22	0.0085	0.196	6.24	-4.55
-	-	-	-	-	2017-10-07	01:11:38.75	133	56	0.24	0.0089	0.206	6.28	-4.51
-	-	-	-	-	2017-10-29	01:40:46.82	103	51	0.24	0.0088	0.202	6.27	-4.53
-	-	-	-	-	2017-10-31	00:37:45.39	116	55	0.27	0.0089	0.204	6.28	-4.52
-	-	-	-	-	2017-12-10	02:08:12.60	137	41	0.23	0.0086	0.199	6.26	-4.54
HD11131 ^g	(3)	5735	0.654	0.299	2017-12-10	05:10:03.30	171	58	0.37	0.0143	0.324	6.52	-4.27
HD114710 ^g	(3)	6006	0.572	0.222	2017-12-31	12:45:12.67	235	120	0.28	0.0104	0.238	6.46	-4.40
-	-	-	-	-	2018-01-02	12:40:47.75	154	76	0.27	0.0103	0.236	6.46	-4.41
-	-	-	-	-	2018-02-01	10:31:27.18	169	89	0.26	0.0099	0.227	6.43	-4.44
-	-	-	-	-	2018-04-23	05:59:54.81	135	67	0.26	0.0098	0.224	6.42	-4.45
-	-	-	-	-	2018-04-30	04:19:41.44	116	62	0.27	0.0103	0.237	6.46	-4.41
-	-	-	-	-	2018-05-05	09:21:05.68	180	67	0.26	0.0095	0.219	6.40	-4.47
HD129333 ^g	(3)	5824	0.626	0.695	2017-10-03	01:29:23.45	130	36	0.75	0.0286	0.639	6.94	-3.87
-	-	-	-	-	2017-12-31	13:00:47.58	93	37	0.76	0.0309	0.688	6.98	-3.84
-	-	-	-	-	2018-01-02	12:47:38.75	92	35	0.74	0.0292	0.652	6.95	-3.86
-	-	-	-	-	2018-02-01	10:54:29.71	108	45	0.78	0.0321	0.715	7.00	-3.82
-	-	-	-	-	2018-02-24	06:54:57.88	89	29	0.76	0.0310	0.692	6.98	-3.83
-	-	-	-	-	2018-04-23	06:31:24.21	92	39	0.77	0.0318	0.709	6.99	-3.82
-	-	-	-	-	2018-04-30	04:30:19.90	120	51	0.79	0.0319	0.711	7.00	-3.82
-	-	-	-	-	2018-05-05	09:51:25.55	137	57	0.74	0.0293	0.653	6.95	-3.86
HD17925 ^g	(3)	5183	0.862	0.659	2017-12-10	05:32:13.48	238	59	0.54	0.0281	0.626	6.55	-4.06
-	-	-	-	-	2018-02-24	01:53:43.39	170	33	0.57	0.0299	0.667	6.58	-4.03
HD1835 ^g	(3)	5720	0.659	0.319	2017-10-29	04:18:11.31	212	66	0.4	0.0157	0.354	6.57	-4.22
-	-	-	-	-	2017-10-31	03:25:37.19	175	53	0.41	0.0156	0.352	6.56	-4.22
-	-	-	-	-	2017-12-10	04:58:32.18	148	32	0.39	0.0155	0.351	6.56	-4.22
HD190406 ^g	(3)	5910	0.600	0.183	2017-09-23	01:28:27.37	224	98	0.24	0.0091	0.210	6.32	-4.52
-	-	-	-	-	2017-10-31	02:20:07.29	59	26	0.25	0.0092	0.211	6.32	-4.52

Table 3 continued on next page

Table 3 (*continued*)

Star name	Remarks ^a	$T_{\text{eff}}^{\text{b}}$ [K]	$B - V^{\text{b}}$ [mag]	$S_{\text{MWO}}^{\text{c}}$	date(UT) ^d	time(UT) ^d	$\text{S/N}(\text{HK})^{\text{e}}$	$r_0(8542)$	S_{APO}	S_{HK}	$\log \mathcal{F}_{\text{HK}}^{+}$ (erg/(cm ² s))	$\log R_{\text{HK}}^{+}$	
-	-	-	-	-	2017-10-31	03:09:10.26	281	107	0.24	0.0092	0.211	6.32	-4.52
-	-	-	-	-	2018-05-05	10:19:25.86	156	76	0.23	0.0085	0.195	6.26	-4.58
HD20630 ^g	(3)	5654	0.681	0.379	2017-10-31	03:48:26.44	104	21	0.45	0.0182	0.410	6.61	-4.15
-	-	-	-	-	2017-10-31	05:51:54.28	201	31	0.46	0.0178	0.401	6.60	-4.16
-	-	-	-	-	2017-12-10	05:42:11.24	296	121	0.42	0.0170	0.382	6.57	-4.19
-	-	-	-	-	2018-01-05	07:18:21.90	245	34	0.41	0.0158	0.357	6.53	-4.23
-	-	-	-	-	2018-02-24	02:02:44.05	117	43	0.43	0.0171	0.384	6.58	-4.19
HD206860 ^g	(3)	5954	0.587	0.332	2017-10-07	06:51:16.37	157	53	0.43	0.0153	0.345	6.67	-4.18
-	-	-	-	-	2017-10-31	02:35:20.55	136	63	0.44	0.0151	0.341	6.67	-4.19
-	-	-	-	-	2018-05-05	10:42:35.83	125	50	0.45	0.0160	0.362	6.70	-4.15
HD22049 ^g	(3)	5140	0.881	0.501	2017-10-31	04:56:33.84	315	48	0.39	0.0204	0.457	6.36	-4.24
-	-	-	-	-	2018-02-24	01:59:09.42	191	49	0.4	0.0214	0.480	6.38	-4.22
HD30495 ^g	(3)	5804	0.632	0.287	2018-01-02	07:34:44.74	180	33	0.34	0.0131	0.298	6.51	-4.30
-	-	-	-	-	2018-02-24	02:08:32.46	199	64	0.33	0.0126	0.286	6.48	-4.33
HD39587 ^g	(3)	5930	0.594	0.379	2017-10-31	06:09:28.99	134	39	0.41	0.0147	0.333	6.64	-4.21
-	-	-	-	-	2017-12-31	08:19:44.48	243	114	0.4	0.0141	0.319	6.61	-4.23
-	-	-	-	-	2018-01-02	07:24:13.10	281	134	0.41	0.0144	0.325	6.63	-4.22
-	-	-	-	-	2018-01-10	07:32:03.90	64	34	0.41	0.0141	0.320	6.61	-4.23
-	-	-	-	-	2018-04-30	02:02:28.04	231	83	0.41	0.0133	0.302	6.58	-4.26
HD41593 ^g	(3)	5296	0.814	0.467	2017-12-10	05:51:26.50	176	58	0.49	0.0230	0.515	6.52	-4.12
-	-	-	-	-	2017-12-31	08:37:11.85	157	55	0.49	0.0233	0.522	6.53	-4.12
-	-	-	-	-	2018-01-02	09:56:19.71	195	41	0.47	0.0228	0.510	6.52	-4.13
-	-	-	-	-	2018-01-05	08:46:02.36	193	65	0.49	0.0233	0.523	6.53	-4.12
-	-	-	-	-	2018-02-01	07:35:33.81	188	54	0.5	0.0240	0.538	6.55	-4.10
-	-	-	-	-	2018-04-30	02:20:09.28	138	37	0.47	0.0217	0.487	6.50	-4.15
HD72905 ^g	(3)	5850	0.618	0.407	2017-12-31	11:51:52.03	233	94	0.44	0.0158	0.358	6.64	-4.18
-	-	-	-	-	2018-01-02	12:34:48.19	127	46	0.46	0.0166	0.373	6.67	-4.16
-	-	-	-	-	2018-01-04	07:18:42.04	78	36	0.46	0.0165	0.372	6.66	-4.16
-	-	-	-	-	2018-01-05	10:37:53.08	163	75	0.46	0.0162	0.365	6.65	-4.17
-	-	-	-	-	2018-01-10	07:56:29.39	67	31	0.47	0.0159	0.358	6.64	-4.18
-	-	-	-	-	2018-02-01	09:53:35.71	161	67	0.48	0.0171	0.385	6.68	-4.14
-	-	-	-	-	2018-02-24	06:46:08.98	129	60	0.48	0.0171	0.386	6.68	-4.14
-	-	-	-	-	2018-04-23	06:22:34.92	115	41	0.48	0.0172	0.387	6.69	-4.14
-	-	-	-	-	2018-04-30	04:41:56.76	168	68	0.49	0.0177	0.399	6.70	-4.12

Table 3 continued on next page

Table 3 (*continued*)

Star name	Remarks ^a	$T_{\text{eff}}^{\text{b}}$ [K]	$B - V^{\text{b}}$ [mag]	$S_{\text{MWO}}^{\text{c}}$	date(UT) ^d [mag]	time(UT) ^d	$S/\text{N}(8542)^{\text{e}}$	$\text{S/N}(\text{HK})^{\text{e}}$	$r_0(8542)$	S_{APO}	S_{HK}	$\log \mathcal{F}_{\text{HK}}^{+}$ (erg/(cm ² s))	$\log R_{\text{HK}}^{+}$
-----------	----------------------	------------------------------------	-----------------------------	-----------------------------	--------------------------------	-----------------------	-------------------------------	------------------------------------	-------------	------------------	-----------------	---	--------------------------

a (1) Active solar-type stars having strong X-ray luminosity, which we have also spectroscopically investigated in Notsu et al. (2017).

(2) Bright solar-type (inactive or mildly active) comparison stars also observed in Notsu et al. (2017).

(3) Other active solar-type stars that we have newly started monitoring spectroscopic observations in this study. These stars are also photometrically observed with TESS (Ricker et al. 2015), and are included in the target list of TESS Guest Investigator programs G011264 (PI: James Davenport) and G011299 (PI: Vladimir Airapetian) (cf. <https://heasarc.gsfc.nasa.gov/docs/tess/approved-programs.html>).

b Stellar effective temperature (T_{eff}) and stellar color ($B - V$). As for the first 15 stars with footnote *e* or *f*, T_{eff} values reported in Notsu et al. (2017) are used here, and we newly derive $B - V$ values from the T_{eff} and metallicity values in Notsu et al. (2017), by using Equation (2) of Alonso et al. (1996). As for the latter 13 stars with footnote *g*, $B - V$ values reported in Table 1 of Isaacson & Fischer (2010) are used here, and T_{eff} values are derived from these $B - V$ values by using Equation (2) of Valenti & Fischer (2005).

c Mount Wilson S-index value (Median value of each target) reported in Table 1 of Isaacson & Fischer (2010).

d Observation date (Universal Time) (format: YYYY-MM-DD) and middle time (Universal Time) (format: hh:mm:ss) of each exposure.

e Signal-to-noise ratio of the spectral data around Ca II 8542 Å ($\text{S}/\text{N}(8542)$) and Ca II H&K 3934/3938Å ($\text{S}/\text{N}(\text{HK})$).

3. ANALYSES AND RESULTS OF THE APO3.5M SPECTROSCOPIC OBSERVATIONS

For the first step of our analyses we checked the binarity, as we have done in our previous studies (e.g., Notsu et al. 2015a; Notsu et al. 2017). The details of the analyses of binarity are described in Appendix A.1. As a result, we regard 5 target stars as binary stars among the 18 superflare stars that we newly observed using the APO3.5m telescope in this study. These five stars are shown in the second column of Table 1. We treat the remaining 13 stars (among these 18 stars observed using APO3.5m) as single stars in this paper, since they do not show any evidence of binarity within the limits of our analyses. In the following, we conduct a detailed analyses for these 13 single stars.

We then estimated various stellar parameters of the target stars, using our spectroscopic data. The details of the analyses and results are described in Appendices A.2 – A.8 of this paper. We estimated stellar atmospheric parameters (T_{eff} , $\log g$, and [Fe/H]) in Appendix A.2, stellar radius (R_{Gaia} and R_{spec}) in Appendix A.3, and the projected rotational velocity ($v \sin i$) in Appendix A.4. We show measurement results of the intensity of Ca II 8542Å and H α lines in Appendix A.5, Ca II H&K S -index in Appendix A.6, and Ca II H&K flux values in Appendix A.7. We also describe the analysis of Lithium (Li) abundance of the target stars in Appendix A.8. The resultant parameters are listed in Tables 4 & 5.

Table 4. Parameters of the target stars estimated from our spectroscopic data.

Star name	Remarks ^a	Binarity ^b	T_{eff} (K)	$\log g$ (cm s ⁻²)	v_t (km s ⁻¹)	[Fe/H] (km s ⁻¹)	$v \sin i$ (km s ⁻¹)	R_{spec} ^c (R_{\odot})	R_{Gaia} (R_{\odot})	P_{rot} (d)	v_{lc} (km s ⁻¹)	$A(\text{Li})$
KIC10532461	–	no	5455±20	4.71±0.05	1.14±0.17	-0.14±0.03	4.3±0.3	0.77 ^{c1}	0.78 ^{+0.06} _{-0.05}	7.14	5.5 ^{+0.9} _{-0.7}	1.98
KIC11652870	–	no	5489±15	4.67±0.04	1.02±0.12	-0.27±0.03	<4	0.76 ^{c1}	0.78 ^{+0.06} _{-0.05}	8.54	4.6 ^{+0.8} _{-0.6}	2.29
KIC9139151	–	no	6063±18	4.31±0.04	1.13±0.11	0.09±0.03	4.5±0.2	1.24	1.14 ^{+0.05} _{-0.05}	6.15	9.4 ^{+1.3} _{-1.0}	2.76
KIC4554830	–	no	5642±30	4.22±0.07	1.05±0.17	0.35±0.05	<4	1.34	1.44 ^{+0.06} _{-0.06}	7.73	9.4 ^{+1.3} _{-1.0}	<1.0
KIC474236	(1)	no	5905±38	3.90±0.09	1.05±0.16	-0.23±0.05	<4	1.83 ^{c1}	—	2.34	39.5 ^{+9.1} _{-8.7}	2.44
KIC4831454	–	no	5637±25	4.65±0.06	1.21±0.17	0.04±0.04	<4	0.88	0.91 ^{+0.07} _{-0.06}	5.19	8.9 ^{+1.4} _{-1.1}	2.79
KIC8656342	–	no	6028±33	4.11±0.07	1.22±0.14	0.02±0.05	4.6±0.2	1.57	1.70 ^{+0.07} _{-0.07}	17.50	4.9 ^{+0.7} _{-0.5}	2.57
KIC9652680	(2)	no	—	—	—	—	38.2±0.1	0.88	1.09 ^{+0.08} _{-0.07}	1.47	37.5 ^{+5.9} _{-4.3}	3.43
KIC6777146	–	no	6158±38	4.39±0.08	1.37±0.19	-0.02±0.06	7.6±0.1	1.11	1.60 ^{+0.12} _{-0.11}	7.21	11.2 ^{+1.8} _{-1.3}	2.57
KIC8508009	–	no	6301±35	4.51±0.07	1.13±0.17	0.18±0.05	4.5±0.2	1.19 ^{c1}	1.15 ^{+0.09} _{-0.08}	2.95	19.7 ^{+3.1} _{-3.1}	3.35
KIC11610797	–	no	6209±43	4.41±0.10	1.70±0.20	0.26±0.05	23.0±0.1	1.24	1.17 ^{+0.05} _{-0.05}	1.62	36.5 ^{+4.9} _{-3.7}	3.62
KIC11233827	–	no	5686±23	4.76±0.06	1.07±0.22	0.19±0.05	<4	0.95 ^{c4}	0.90 ^{+0.04} _{-0.04}	13.40	3.4 ^{+0.5} _{-0.4}	1.34
KIC6291837	–	no	6270±48	4.29±0.09	1.48±0.23	0.00±0.07	7.9±0.1	1.30	1.42 ^{+0.07} _{-0.07}	14.30	5.0 ^{+0.8} _{-0.6}	2.71
KIC11551430A	(1),(3)	RV(+VB)	5589±40	3.95±0.10	1.88±0.25	-0.20±0.07	18.8±0.1	1.81	—	4.26	21.4 ^{+5.0} _{-4.8}	2.33
KIC11551430B	(3)	(VB)	5943±98	5.44±0.27	0.81±0.50	0.22±0.10	<4	1.08 ^{c3}	—	—	—	<2.3
KIC4543412	(4)	RV	5655±73	4.92±0.18	1.95±0.38	0.07±0.10	18.3±0.1	0.97 ^{c2}	0.96 ^{+0.07} _{-0.06}	2.16	22.5 ^{+3.5} _{-2.6}	<2.0
KIC11128041	(5)	SB2+RV	—	—	—	—	—	—	1.21 ^{+0.09} _{-0.08}	7.36	8.3 ^{+1.3} _{-1.0}	—
KIC10338279	(1),(5)	SB2	—	—	—	—	—	—	—	6.53	—	—
KIC7093428	(1),(6)	VB	6364±60	4.02±0.01	1.45±0.25	-0.02±0.07	5.1±0.2	1.90	—	0.51	187.8 ^{+43.0} _{-41.3}	<2.3

Table 4 continued on next page

Table 4 (*continued*)

Star name	Remarks ^a	Binarity ^b	T_{eff} (K)	$\log g$ (cm s ⁻²)	v_t (km s ⁻¹)	[Fe/H] (km s ⁻¹)	$v \sin i$ (km s ⁻¹)	R_{spec}^c (R_{\odot})	R_{Gaia} (R_{\odot})	P_{rot} (d)	v_{lc} (km s ⁻¹)	$A(\text{Li})$
-----------	----------------------	-----------------------	-------------------------	-----------------------------------	--------------------------------	---------------------------------	-------------------------------------	--	--------------------------------------	-------------------------	-----------------------------------	----------------

a (1) As for these four stars (KIC4742436, KIC11551430A, KIC10338279, and KIC7093428), there are no stellar radius values R_{Gaia} reported in (Berger et al. 2018) (*Gaia*-DR2). For these four stars, R_{spec} (stellar radius estimated from T_{eff} , $\log g$, and [Fe/H] in Appendix A.3) values are used to calculate v_{lc} values, while R_{Gaia} values are used for the other stars.

(2) We cannot estimate atmospheric parameters (T_{eff} , $\log g$, v_t , and [Fe/H]) of KIC952680 since the rotational velocity of this star is large ($\gtrsim 30$ km s⁻¹) and the spectral lines of these stars are too wide to estimate the atmospheric parameters in our way using equivalent widths of Fe I/II lines (see Appendix A.2 for the details). When we estimate $v \sin i$, R_{spec} , and $A(\text{Li})$ values listed in this table, $T_{\text{eff,DR25}}$, $(\log g)_{\text{DR25}}$, and $[\text{Fe}/\text{H}]_{\text{DR25}}$ (DR25 KSPC values) in Table 1 are used, and microturbulence velocity (v_t) is assumed to be 1 km s⁻¹, as also done in Notsu et al. (2015a).

(3) KIC11551430 is found to be visual binary (KIC11551430A and KIC1551430B), as described in Appendix A.1. We took spectra of each component of visual binary separately, and measured stellar parameters of each of them.

(4) KIC4543412 shows radial velocity changes but has single-lined profiles. After shifting the wavelength value of each spectrum to the laboratory frame on the basis of the RV value of each observation, we added up these shifted spectra to one co-added spectrum, as described in Appendix A.1. We measured stellar parameters by using this combined spectrum.

(5) We do not measure any parameters from the spectra of KIC1128041 and KIC10338279 since these stars show double-lined profiles.

(6) As described in Appendix A.1, KIC7093428 has two fainter companion stars, and pixel data analyses suggest that flares occur on these companion stars. Since companion stars are faint, here we only measured stellar parameters of the main (brightest) star for reference, though we do not use these values in the main discussion of this paper.

b Same as in footnote *a* of Table 1. See also Appendix A.1.

c As for the six stars with the marks *c1*, *c2*, *c3*, or *c4*, there are no suitable PARSEC isochrones within their original error range of T_{eff} and $\log g$ values (ΔT_{eff} and $\Delta \log g$), as mentioned in Appendix A.3. We then enlarge error ranges to find the appropriate isochrone values. As for the three stars with *c1*, we take into account $2\Delta T_{\text{eff}} \& 2\Delta \log g$. As for the stars with *c2*, *c3*, and *c4*, we take into account the error ranges “ $2\Delta T_{\text{eff}} \& 3\Delta \log g$ ”, “ $2\Delta T_{\text{eff}} \& 4\Delta \log g$ ”, and “ $2\Delta T_{\text{eff}} \& 5\Delta \log g$ ”, respectively.

Table 5. Activity indicators of the target stars.

Star name	Remarks ^a	Binarity ^b	$\langle \text{BV Amp} \rangle^c$	$r_0(8542)$	$r_0(\text{H}\alpha)$	S_{HK}	$\log \mathcal{F}'_{\text{HK}}$ (erg/(cm ² s))	$\log R'_{\text{HK}}$ (erg/(cm ² s))	$\log \mathcal{F}_{\text{HK}}^+$ (erg/(cm ² s))	$\log R_{\text{HK}}^+$ (erg/(cm ² s))
KIC10532461	-	no	$1.55^{+0.73}_{-0.74}$	0.51	0.33	0.465	6.70	-4.00	6.66	-4.04
KIC11652870	-	no	$0.93^{+0.23}_{-0.25}$	0.46	0.32	0.413	6.68	-4.03	6.64	-4.07
KIC9139151	-	no	$0.06^{+0.07}_{-0.02}$	0.22	0.19	0.177	6.40	-4.49	6.27	-4.61
KIC4554830	-	no	$0.03^{+0.01}_{-0.01}$	0.19	0.18	0.164	6.11	-4.65	5.93	-4.83
KIC4742436	-	no	$0.46^{+0.43}_{-0.24}$	0.28	0.30	0.216	6.52	-4.32	6.43	-4.41
KIC4831454	-	no	$0.91^{+1.27}_{-0.50}$	0.53	0.32	0.480	6.77	-3.99	6.73	-4.02
KIC8656342	-	no	$0.03^{+0.01}_{-0.01}$	0.22	0.20	0.175	6.39	-4.48	6.26	-4.61
KIC9652680	-	no	$4.72^{+1.32}_{-2.06}$	0.65	0.51	0.509	6.95	-3.87	6.92	-3.90
KIC6777146	-	no	$0.09^{+0.05}_{-0.03}$	0.26	0.23	0.179	6.47	-4.44	6.35	-4.56
KIC8508009	-	no	$0.28^{+0.16}_{-0.09}$	0.38	0.28	0.278	6.74	-4.21	6.69	-4.27
KIC11610797	-	no	$2.44^{+0.66}_{-0.95}$	0.63	0.47	0.498	6.99	-3.93	6.96	-3.96
KIC11253827	-	no	$1.59^{+0.84}_{-0.83}$	0.39	0.26	0.351	6.61	-4.17	6.55	-4.22
KIC6291837	-	no	$0.08^{+0.02}_{-0.02}$	0.26	0.22	0.195	6.56	-4.38	6.47	-4.47
KIC11551430A	(1)	RV(+VB)	$2.65^{+1.42}_{-1.13}$	0.83	0.69	0.813	7.04	-3.70	7.02	-3.72
KIC11551430B	(1)	VB	-	0.24	0.20	0.462	6.85	-3.99	6.82	-4.03
KIC4543412	(2)	RV	$4.77^{+2.02}_{-2.25}$	0.80	0.62	0.844	7.04	-3.72	7.02	-3.74
KIC11128041	(3)	SB2+RV	$0.48^{+0.28}_{-0.21}$	-	-	-	-	-	-	-
KIC10338279	(3)	SB2	$1.29^{+0.35}_{-0.40}$	-	-	-	-	-	-	-
KIC7093428	(4)	VB	$0.13^{+0.04}_{-0.06}$	0.22	0.19	0.150	6.44	-4.53	6.30	-4.67

Table 5 continued on next page

Table 5 (*continued*)

Star name	Remarks ^a	Binarity ^b	$\langle \text{BVamp} \rangle^c$	$r_0(8542)$	$r_0(\text{H}\alpha)$	S_{HK}	$\log F'_{\text{HK}}$ (erg/(cm ² s))	$\log R'_{\text{HK}}$	$\log F_{\text{HK}}^+$ (erg/(cm ² s))	$\log R_{\text{HK}}^+$
-----------	----------------------	-----------------------	----------------------------------	-------------	-----------------------	-----------------	--	-----------------------	---	------------------------

a (1) KIC11551430 is found to be visual binary (KIC11551430A and KIC11551430B), as described in Appendix A.1.

We took spectra of each component of visual binary separately, and measure stellar parameters of each of them.

(2) KIC4543412 shows radial velocity changes but has single-lined profiles. After shifting the wavelength value of each spectrum to the laboratory frame on the basis of the RV value of each observation, we added up these shifted spectra to one co-added spectrum, as described in Appendix A.1. We measured stellar parameters by using this combined spectrum.

(3) We do not measure any parameters from the spectra of KIC11128041 and KIC10338279 since these stars show double-lined profile.

(4) As described in Appendix A.1, KIC7093428 has two fainter companion stars, and pixel data analyses suggest that flares occur on these companion stars. Since companion stars are faint, here we only measured stellar parameters of the main (brightest) star for reference, though we do not use these values in the main discussion of this paper.

b Same as in footnote *a* of Table 1. See also Appendix A.1.

c The amplitude of the brightness variation. This value is calculated by taking the average of the amplitude value of each Quarter (Q2 – Q16) data, as also done in Notsu et al. (2015b). We did not use Q0, Q1, and Q17 data since the duration of these three quarters is short (30 d) compared to those of the other 15 quarters (~ 90 d) (Thompson et al. 2015). The errors of $\langle \text{BVamp} \rangle$ correspond to the maximum and minimum of the amplitude values of all Quarter (Q2 – Q16) data.

4. DISCUSSIONS ON THE RESULTS FROM OUR APO3.5M SPECTROSCOPIC OBSERVATIONS

4.1. Binarity

Table 6. Number of the “single” and “binary” stars

	Total	Single	Binary ^a
APO3.5m (This study)	18	13	5(2)
Subaru/HDS (Notsu et al. 2015a)	50	34	16(4)
Total	64 ^b	43 ^b	21(6)

^a Numbers in parentheses correspond to visual binary stars.

^b Four single stars (KIC4742436, KIC4831454, KIC9652680, and KIC11610797) were observed in the both studies (APO3.5m and Subaru/HDS).

In Section 3 and Appendix A.1, we described more than half (13 stars) of the 18 superflare stars that we newly conducted APO3.5m spectroscopic observations have no obvious evidence of being in a binary system. Combined with the results of the 50 stars that we observed with Subaru telescope in [Notsu et al. \(2015a\)](#), we have conducted spectroscopic observations of 64 superflare stars in total (Table 6). Four stars (KIC4742436, KIC4831454, KIC9652680, and KIC11610797) among these 64 stars were observed in the both studies. As a result, 43 stars among the total 64 solar-type superflare stars are classified as “single” stars. However, we need to remember here that we cannot completely exclude the possibility that some of these 43 “single” superflare stars have companions since observations and analyses in this study are limited, as we have also described in detail in Section 4.1 of [Notsu et al. \(2015a\)](#).

For example, as for the target stars with “multiple” observations in this study, only those showing large radial velocity changes would likely be detected in the randomly spaced observations. Targets with longer period orbits would require more observations spaced accordingly. Thus, only the short-period systems likely would be captured, and even then some would be missed by accident of poorly spaced observations (e.g., the case that the time differences between the observations correspond to the orbital period of the binary system). We must note these points, but we consider that more detailed analyses of binarity are not really necessary for the overall discussion of stellar properties of superflare stars in this paper.

Two target stars KIC11551430 and KIC7093428 are classified as visual binary stars on the basis of the slit viewer images, Figures 19 & 20 in Appendix A.1. Pixel count data of these two stars suggested that superflares occur on the primary star KIC11551430A as for the visual binary system KIC11551430, while flares occur on the fainter companion stars KIC7093428B or KIC7093428C as for the system KIC7093428. Measurement results of rotation velocity $v \sin i$ and chromospheric line intensities in this study (listed in Tables 4 & 5) support this suggestion. As for KIC11551430, the primary star KIC11551430A rotates much more rapidly ($v \sin i \sim 18.8 \text{ km s}^{-1}$) than the companion star KIC11551430B ($v \sin i < 4 \text{ km s}^{-1}$). Moreover, the primary KIC11551430A show strong chromospheric emissions while the companion KIC11551430B does not show any strong emissions (Figures 26, 27, & 28). The primary KIC11551430A can have much higher probability to generate superflares since superflare stars are generally well characterized with rapid rotation velocity and high

chromospheric activity levels. In contrast, the primary KIC7093428A has no strong chromospheric emissions (Figures 26, 27, & 28), and this primary star does not show any properties as superflare stars. It is therefore highly possible that flares occur on the fainter companion stars KIC7093428B or KIC7093428C mentioned above.

As seen in Table 1, stars identified as binary stars tend to show larger number of flares. For example, KIC11551430 and KIC4543412, which show radial velocity shifts, have $N_{\text{flare}}=89$ and 13, respectively. All the stars identified as “single” stars have $N_{\text{flare}} < 10$ in Table 1. As a result, among the 187 superflares (on 23 stars) from *Kepler* 1-min cadence data in Maehara et al. (2015), at least 127 events are found to occur on binary stars. This means the large part of the superflare data of the Kepler 1-min cadence sample (Maehara et al. 2015) are contaminated by binary stars (e.g., close binary stars). The data from Maehara et al. (2015) are therefore not enough for investigating the possibility of superflares on Sun-like stars, and we need to more investigations by increasing the number of single superflare stars (cf. See also the first paragraph of Section 6.3).

4.2. Estimated atmospheric parameters

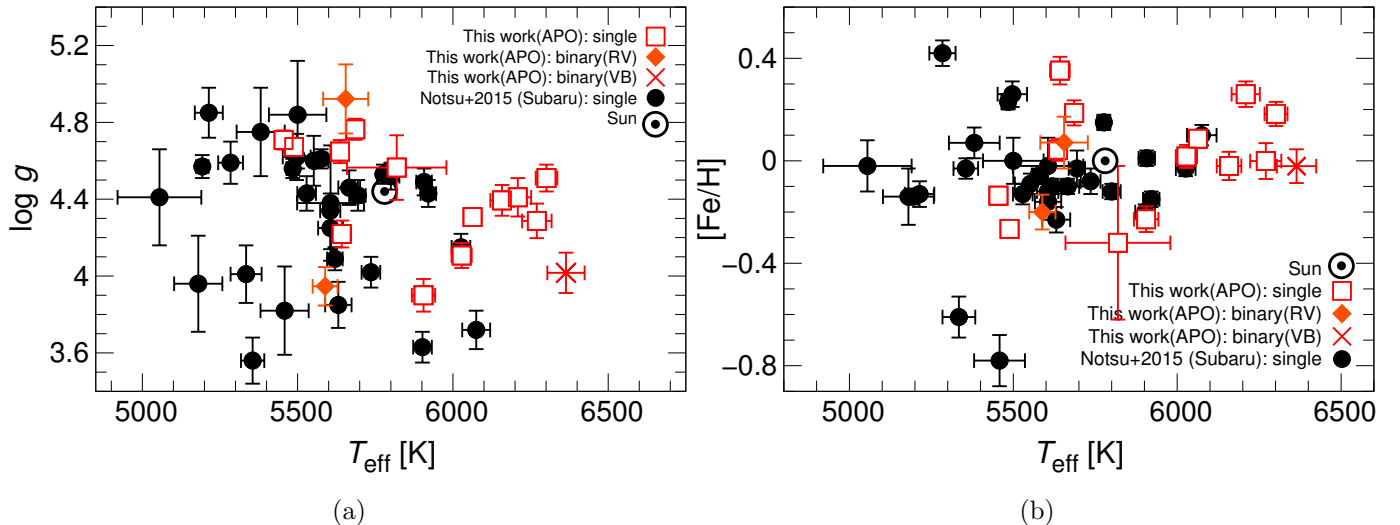


Figure 1. Temperature (T_{eff}), surface gravity ($\log g$), and metallicity ($[\text{Fe}/\text{H}]$), estimated from spectroscopic observations. The red open square points are the target superflare stars classified as single stars in Appendix A.1, and the orange diamonds correspond to the spectra of binary superflare stars that do not show any double-lined profiles (KIC11551430A and KIC4543412). A visual binary superflare star KIC7093428 (see Section 4.1 for the details) is plotted for reference with the red cross mark. The single superflare stars that we investigated using Subaru telescope (Notsu et al. 2015a), excluding the four stars also investigated in this study (See footnote f of Table 1), are plotted with the black circles. The open circle dot corresponds to the Sun.

We estimated the atmospheric parameters (T_{eff} , $\log g$, and $[\text{Fe}/\text{H}]$) of the target superflare stars in Appendix A.2. The measured values of the 13 single target stars of this observation are $T_{\text{eff}}=5400-6300\text{K}$, $\log g=3.9-4.8$, and $[\text{Fe}/\text{H}]=(-0.3)-(+0.3)$, respectively (Figure 1). This indicates that the stellar parameters of these 13 single target superflare stars are roughly in the range of solar-type (G-type main-sequence) stars, though the stars with $\log g \lesssim 4.0$ are possibly sub-giant G-type stars

(For the discussions on evolutionary state of the target stars, see also Section 5.1). Compared with the 34 single target superflare stars that we observed in Notsu et al. (2015a), the target stars tend to have a bit hotter T_{eff} values, and most of them are “solar-analog” stars (early-type G-type main-sequence stars). No clear “metal-rich” or “metal-poor” stars are included in the target stars of this observation.

4.3. Rotational velocity

As described above, we report the values of projected rotational velocity $v \sin i$, stellar radius R (R_{Gaia} and R_{spec}), and the rotation period P_{rot} from the brightness variation of the single target superflare stars (listed in Table 4). Using the R and P_{rot} values, we can estimate the rotational velocity (v_{lc}):

$$v_{\text{lc}} = \frac{2\pi R}{P_{\text{rot}}} , \quad (1)$$

as also described in Section 4 of Notsu et al. (2015b). As for the R values, we used $R = R_{\text{Gaia}}$ as a first priority, and $R = R_{\text{spec}}$ only for the stars without R_{Gaia} values. As for the errors of v_{lc} , we took the root sum squares of the two types of errors from R (see the descriptions in Appendix A.3) and P_{rot} . We here assume the possible errors of P_{rot} are about 10%, as done in Notsu et al. (2015b). In this assumption, we very roughly consider typical possible differences between equatorial rotation period and the measured period caused by the solar-like differential rotations. For example, the solar latitudinal differential rotation has a magnitude of 11% of the average rate from equator to midlatitudes ($\approx 45^\circ$ latitude) (cf. Benomar et al. 2018). We must note here that the differences can be much larger if we observe starspots near the pole region, and there can be solar-type stars with much larger differential rotation magnitudes (Benomar et al. 2018). Moreover, it is sometimes hard to distinguish the correct P_{rot} values with $1/n \times P_{\text{rot}}$ ($n=2, 3, \dots$) values in the periodogram, especially when there are several starspots on the surface of the stars (cf. Figure 2 of Notsu et al. 2013b). As a result, we must note here with caution that P_{rot} can have much larger error values, though the detailed investigations of each error value is beyond the scope of the overall discussions of $v \sin i$ vs. v_{lc} in Figure 2. The resultant values of v_{lc} are listed in Table 4.

We then plot $v \sin i$ as a function of v_{lc} in Figure 2. Not only the target superflare stars of this study (13 “single” stars and two binary stars categorized as “RV” and “VB” in Appendix A.1), but also the 34 single superflare stars that we have observed in Notsu et al. (2015b) are plotted for reference. The v_{lc} values of the latter 34 superflare stars are updated from the original ones in Notsu et al. (2015b). We newly recalculated v_{lc} (cf. Equation 1) of each target star by using R_{Gaia} value if the star has R_{Gaia} value reported in Berger et al. (2018).

In Figure 2, $v \sin i$ tends to be smaller than v_{lc} , and such differences should be explained by the inclination angle effect, as mentioned in the previous studies (e.g., Hirano et al. 2012; Notsu et al. 2015b). On the basis of $v \sin i$ and v_{lc} , the stellar inclination angle (i) can be estimated by using the following relation:

$$i = \arcsin \left(\frac{v \sin i}{v_{\text{lc}}} \right) . \quad (2)$$

In Figure 2, we also show four lines indicating $i = 90^\circ$ ($v \sin i = v_{\text{lc}}$), $i = 60^\circ$, $i = 30^\circ$, and $i = 10^\circ$. First of all, almost all the stars (except for KIC6291837 with $v \sin i \sim 7.9 \text{ km s}^{-1}$ and $v_{\text{lc}} \sim 5.0 \text{ km s}^{-1}$)

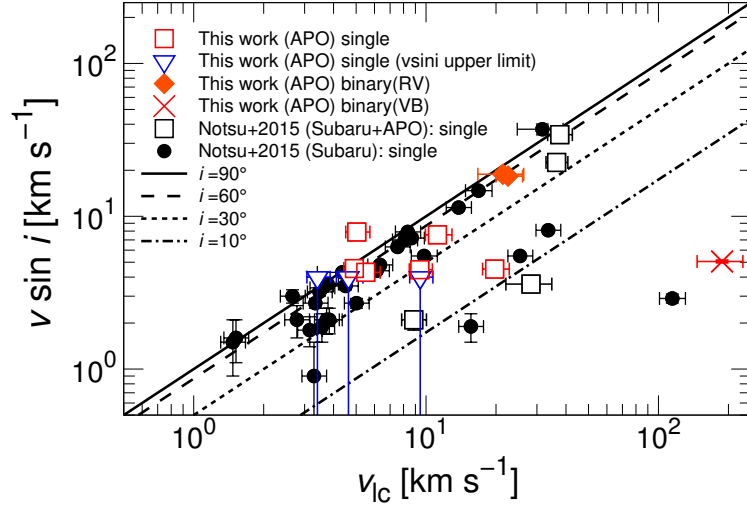


Figure 2. Projected rotational velocity ($v \sin i$) vs. the stellar rotational velocity (v_{lc}) estimated from the period of the brightness variation (P_{rot}) and stellar radius (R). The solid line represents the case that our line of sight is perpendicular to the stellar rotation axis ($i = 90^\circ$; $v \sin i = v_{lc}$). We also plot three different lines, which correspond to smaller inclination angles ($i = 60^\circ, 30^\circ, 10^\circ$). The open red square and blue downward triangle points are the target superflare stars classified as single stars in Appendix A.1, and the latter points (blue triangles) correspond to the slowly-rotating stars only with the upper limit of values $v \sin i$ ($v \sin i < 4 \text{ km s}^{-1}$) (cf. Appendix A.4 for the details). The orange diamonds correspond to the spectra of binary superflare stars that do not show any double-lined profiles (KIC11551430A and KIC4543412). A visual binary superflare star KIC7093428 (see Section 4.1 for the details) is plotted for reference with the red cross mark. The single superflare stars that we investigated using Subaru telescope (Notsu et al. 2015b) are plotted with the black circles and black open squares. As for the four stars (KIC4742436, KIC4831454, KIC9652680, and KIC11610797) investigated both in Notsu et al. (2015b) and in this study (See footnote f of Table 1), the values in Notsu et al. (2015b) (Subaru) are only plotted in this table (black open squares), and the values from APO data are not used. This is because the wavelength resolution (i.e. accuracy of $v \sin i$ estimation) of Subaru/HDS data is higher than that of APO data (cf. Appendix A.4).

in Figure 2, the relation “ $v \sin i \lesssim v_{lc}$ ” is satisfied. This is consistent with the assumption that the brightness variation is caused by the rotation since the inclination angle effect can cause this relation “ $v \sin i \lesssim v_{lc}$ ” if v_{lc} really corresponds to the rotation valosity (i.e. $v = v_{lc}$). This is also supported by the fact that the distribution of the data points in Figure 2 is not random, but is concentrated between the lines of $i = 90^\circ$ and $i = 60^\circ$. The distribution is expected to be much more random if the brightness variations have no relations with the stellar rotation. In addition, stars that are distributed in the lower right side of Figure 2 are expected to have small inclination angles and to be nearly pole-on stars. Later in Section 5.2, we see these inclination angle effects from another point of view with the scatter plot of flare energy and starspot size.

Summarizing the results in this section, we can remark that rotation velocity values from spectroscopic results ($v \sin i$) and those from *Kepler* brightness variation (v_{lc}) are consistent, and this supports that the brightness variation of superflare stars is caused by the rotation. This remark was

already suggested in Notsu et al. (2015b), but the conclusions are more strongly confirmed by the new spectroscopic observations and *Gaia*-DR2 stellar radius (R_{Gaia}) values.

4.4. Stellar chromospheric activity and starspots of superflare stars

We measured the core intensity and flux values of chromospheric lines (Ca II 8542Å, H α 6563Å, and Ca II H&K lines) in Appendices A.5 – A.7. These lines have been widely used for investigating stellar chromospheric activities (e.g., Wilson 1978; Linsky et al. 1979b; Noyes et al. 1984; Duncan et al. 1991; Baliunas et al. 1995; Hall 2008), and are good indicators of stellar average magnetic fields (e.g., Schrijver et al. 1989; Notsu et al. 2015b). Only the Ca II 8542Å line is mainly used in our previous studies using the Subaru telescope (Notsu et al. 2013a & 2015b; Nogami et al. 2014). In this study, Ca II H&K lines are used with high dispersion spectra for the first time in our series of studies of the *Kepler* solar-type superflare stars⁶.

In Figure 3, we compare the Ca II 8542Å and Ca II H&K index values ($r_0(8542)$ and $\log R_{\text{HK}}^+$) with the amplitude of the brightness variation of *Kepelr* data ($\langle \text{BV}Amp \rangle$). The $r_0(8542)$ index is the normalized intensity at the center of the Ca II 8542Å line (See Section A.5 for the details). The $\log R_{\text{HK}}^+$ index is a universal and “pure” Ca II H&K activity indicator introduced by Mittag et al. (2013), and is defined as $\mathcal{R}_{\text{HK}}^+ = \mathcal{F}_{\text{HK}}^+ / \sigma T_{\text{eff}}^4$ (Equation A13), where $\mathcal{F}_{\text{HK}}^+$ is the Ca II H&K surface flux (unit : [erg cm $^{-2}$ s $^{-1}$]) with photospheric and “basal” flux contributions removed (See Appendix A.7 for the details). As described in Figure 30 in Appendix A.7, this $\log R_{\text{HK}}^+$ index has a good correlation with the $r_0(8542)$ index, and $\log R_{\text{HK}}^+$ can be more sensitive to the difference in the lower activity level region compared with $r_0(8542)$. $\langle \text{BV}Amp \rangle$ values are calculated by taking the average of the amplitude value of each Quarter (Q2 – Q16) data, as we have done in Notsu et al. (2015b). The resultant values of $\langle \text{BV}Amp \rangle$ of the target stars of our APO3.5m observations are listed in Table 5. In Figure 3, we also plot solar values as a reference, as done in Notsu et al. (2015b), and we can see that as for most of the target superflare stars, Ca II 8542Å and Ca II H&K index values are higher than the solar values. This suggests that these superflare stars have higher chromospheric activities compared with the Sun.

More importantly, there is a rough positive correlation between Ca II index values and $\langle \text{BV}Amp \rangle$ in Figure 3. Assuming that the brightness variation of superflare stars is caused by the rotation of a star with starspots, the brightness variation amplitude ($\langle \text{BV}Amp \rangle$) corresponds to the starspot coverage of these stars. As mentioned above, Ca II index values are good indicators of stellar average magnetic field (or total magnetic flux). Then, we can remark that there is a rough positive correlation between the starspot coverage from *Kepler* photometric data and the stellar average magnetic field from spectroscopic data. All the target stars expected to have large starspots on the basis of their large amplitude of the brightness variation show strong average magnetic field compared with the Sun. In other words, our assumption that the amplitude of the brightness variation corresponds to the spot coverage is supported, since the average magnetic field is considered to be caused by the existence of large starspots. These results have been already confirmed in Notsu et al. (2015b) with Ca II 8542Å line, but in this study we confirmed the same conclusion with the following two updates: (i) Larger number of stars with Ca II 8542Å line data (Figure 3a), (ii) Analyses using Ca II H&K lines (Figure 3b).

⁶ We note here that Karoff et al. (2016) already investigated Ca II H&K line intensity and flux values of superflare stars with LAMOST “low-resolution” spectra.

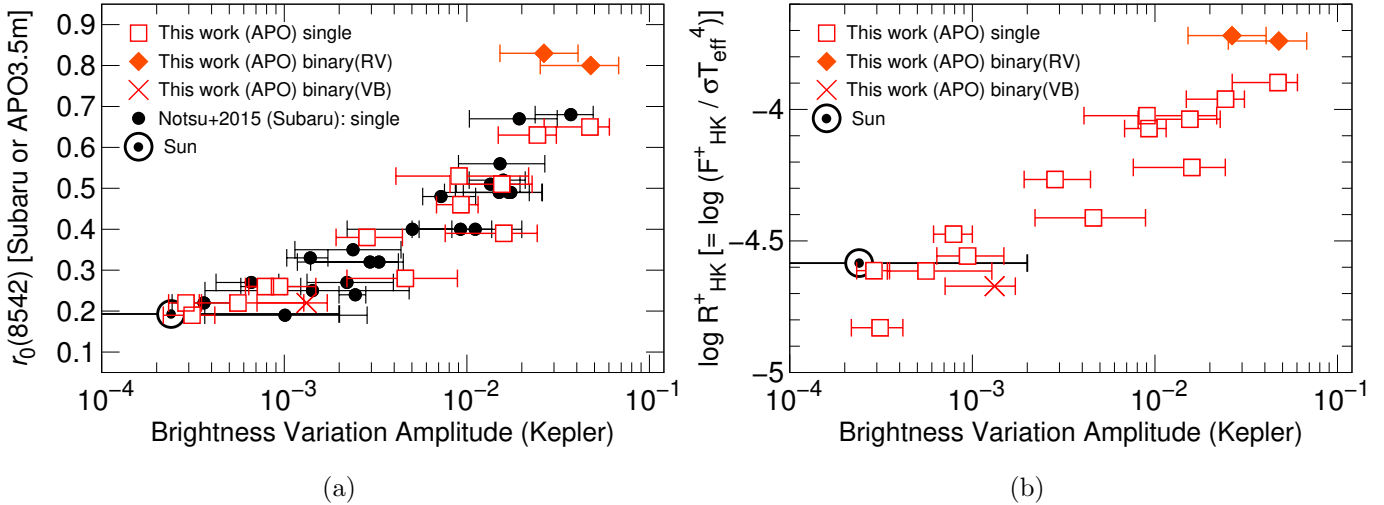


Figure 3. (a) $r_0(8542)$ (the normalized intensity at the center of Ca II 8542Å line) vs. $\langle \text{BV} \text{Amp} \rangle$ (the amplitude of stellar brightness variation of *Kepelr* data).

(b) Ca II H&K activity index $\log \mathcal{R}_{\text{HK}}^+ (= \mathcal{F}_{\text{HK}}^+ / \sigma T_{\text{eff}}^4)$ vs. $\langle \text{BV} \text{Amp} \rangle$.

The red open square points are the target superflare stars classified as single stars in Appendix A.1, and the orange diamonds correspond to the spectra of binary superflare stars that do not show any double-lined profiles (KIC11551430A and KIC4543412). A visual binary superflare star KIC7093428 (see Section 4.1 for the details) is plotted for reference with the red cross mark. Only in (a), the single superflare stars that we investigated using Subaru telescope (Notsu et al. 2015b), excluding the four stars also investigated in this study (See footnote *f* of Table 1), are also plotted with black circles. The solar value is plotted by using a circled dot point. The difference of Ca II index values between solar maximum and solar minimum is no larger than the size of this point (Lockwood et al. 2007).

4.5. *Li abundances*

We also estimated Li abundances $A(\text{Li})$ of the target superflare stars in Appendix A.8. Li abundance is known to be a clue for investigating the stellar age of solar-type stars. (e.g., Skumanich 1972; Takeda et al. 2010 & 2013; Honda et al. 2015; Notsu et al. 2017). The Li depletion is seen in the stars with $T_{\text{eff}} \lesssim 5500\text{K}$, while the stars with $T_{\text{eff}} \gtrsim 6000\text{K}$ show no Li depletion. This is because as the star becomes cooler, the convection zone in the stellar atmosphere evolves and the Li is transported to a deeper hotter zone, where Li is easily destroyed (p, α reactions: ${}^7\text{Li}$, $T \geq 2.5 \times 10^6\text{K}$; ${}^6\text{Li}$, $T \geq 2.0 \times 10^6\text{K}$). The depletion of Li in the stellar surface caused by convective mixing increases as time passes, and we can remark that young stars tend to have high $A(\text{Li})$ values.

In Figure 4, we plot $A(\text{Li})$ as a function of T_{eff} of the superflare stars with the ordinary stars in the Hyades cluster (taken from Takeda et al. 2013). Some of the superflare stars show high Li compared with the stars in the Hyades cluster (Figure 4), and such stars are suggested to be younger than the Hyades cluster. The age of the Hyades cluster is estimated to be 6.25×10^8 yr (e.g., Perryman et al. 1998). It is reasonable that such young stars tend to have high activity levels and produce superflares. However, more than 10 target stars do not show higher $A(\text{Li})$ values compared with the Hyades, and a few of them are as low as the solar value. These results suggest that superflare stars include many young stars but also include old stars like our Sun, as also suggested in Honda et al. (2015).

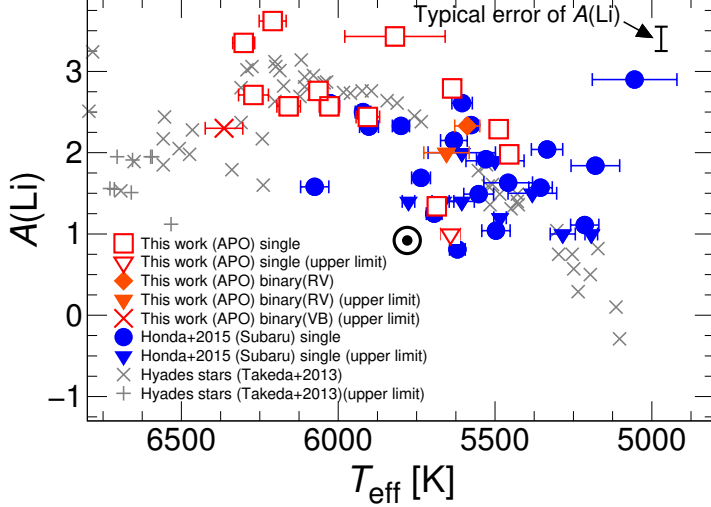


Figure 4. $A(\text{Li})$ vs. T_{eff} of the target superflare stars with the stars in the Hyades cluster. The age of Hyades is 6.25×10^8 yr (e.g., Perryman et al. 1998). The red open square/triangle points are the target superflare stars classified as single stars in Appendix A.1, and the orange diamond/triangle points correspond to the spectra of binary superflare stars that do not show any double-lined profiles (KIC11551430A and KIC4543412). A visual binary superflare star KIC7093428 (see Section 4.1 for the details) is plotted for reference with the red cross mark. The single superflare stars that we investigated using Subaru telescope (Notsu et al. 2015b), excluding the four stars also investigated in this study (See footnote f of Table 1), are also plotted with blue circles/triangles. Among the above symbols, the triangles and the cross mark correspond to the upper limit values of $A(\text{Li})$ for the unmeasurable cases. We plot the data of the stars in Hyades cluster reported by Takeda et al. (2013) with gray cross marks (x marks and plus marks), and the plus marks correspond to the upper limit values of $A(\text{Li})$ for the unmeasurable cases. The solar value is also plotted with a circled dot point for reference. Typical error value of $A(\text{Li})$ (~ 0.15 dex) mentioned in Appendix A.8 is shown with the error bar in the upper right of this figure.

5. STATISTICAL PROPERTIES OF *KEPLER* SOLAR-TYPE SUPERFLARE STARS INCORPORATING *GAIA*-DR2 DATA

5.1. Evolutionary state classifications of superflare stars

In this section, we investigate again the statistical discussions of *Kepler* solar-type superflare stars in our previous studies (Maehara et al. 2012, 2015, & 2017; Shibayama et al. 2013; Notsu et al. 2013b), by incorporating *Gaia*-DR2 stellar radius estimates (reported in Berger et al. 2018) and the results of our spectroscopic observations (Subaru and APO3.5m observations). In these previous studies, we reported 1547 superflare events on 279 solar-type (G-type main-sequence) stars from *Kepler* 30-min (long) time cadence data (Shibayama et al. 2013), and 189 superflares on 23 solar-type stars from *Kepler* 1-min (short) time cadence data (Maehara et al. 2015) (Line 1 of Tables 7 & 8). As also used in Appendix A.3, Berger et al. (2018) reported the catalog of the 177,911 *Kepler* stars with the stellar radius estimates (R_{Gaia}) estimated from *Gaia*-DR2 parallax values. 245 stars among the 279 solar-type superflare stars in Shibayama et al. (2013) and 18 stars among the 23 stars in Maehara et al. (2015) have R_{Gaia} values in this *Gaia*-DR2 catalog, respectively (Line 2 of Tables 7 & 8).

We plot these superflare stars on the stellar radius (R) vs. T_{eff} diagram in Figures 5 (a)&(b). In these figures, all the *Kepler* stars reported in Berger et al. (2018) are also plotted for reference with the evolutionary state classifications (Main sequence (MS) / subgiants / red giants / cool main-sequence binaries). In Figure 5 (a), among the 245 stars found as solar-type superflare stars from *Kepler* 30-min time cadence data in Shibayama et al. (2013), 136 stars (55.5%) are classified as main-sequence stars, while 108 stars (44.1%) as subgiants and only one star (KIC4633721) as a red giant (Lines (3) – (5) of Table 7). Originally in Shibayama et al. (2013), we used the T_{eff} and $\log g$ values in the initial *Kepler* Input Catalog (KIC; Brown et al. 2011) and selected solar-type (G-type main-sequence) stars with the definition of $5100 \text{ K} \leq T_{\text{eff}} \leq 6000 \text{ K}$ and $\log g \geq 4.0$. T_{eff} and $\log g$ values in the initial KIC have large error values of $\pm 200 \text{ K}$ and 0.4 dex, respectively (Brown et al. 2011), and the reliability of each value can be low. In Figure 5 (a), not only using the updated stellar radius R_{Gaia} from *Gaia*-DR2 data, but T_{eff} values are also updated with the latest DR25 *Kepler* Stellar Properties Catalog (DR25-KSPC; Mathur et al. 2017), which incorporates the revised method of T_{eff} estimation (cf. Pinsonneault et al. 2012). As a result, large fraction (more than 40%) of the stars that were originally identified as solar-type superflare stars in Shibayama et al. (2013) are now classified as subgiant or red giant stars.

In Figure 5 (b), among the 18 stars found as solar-type superflare stars from *Kepler* 1-min time cadence data in Maehara et al. (2015), 13 stars are classified as main-sequence stars, while 5 stars are as subgiant stars (Lines (3) – (5) of Table 8). In the case of these 18 stars, the revised KIC catalog (Huber et al. 2014) were used when we selected solar-type stars in Maehara et al. (2015), and it is possible that the errors of T_{eff} was somewhat smaller, compared with the case of the stars from Shibayama et al. (2013) in Figure 5 (a).

In Figure 5(c), we plot 50 superflare stars found from *Kepler* 30-min cadence data that we have spectroscopically observed using Subaru telescope (Notsu et al. 2015a&2015b). As for the radius value in the vertical axis of these two figures, R_{Gaia} value is used if it exists. If the star has no R_{Gaia} value in Berger et al. (2018), R_{spec} values (in Table 4 of Notsu et al. 2015a) are used for single stars and R_{DR25} values (from DR25-KSPC in the above) are used for binary stars. As for the temperature value in the horizontal axis, T_{eff} values estimated from spectroscopic data (in Table 4 of Notsu et al. 2015a) are used for single stars, while $T_{\text{eff,DR25}}$ values are used for binary stars. As a result, 24

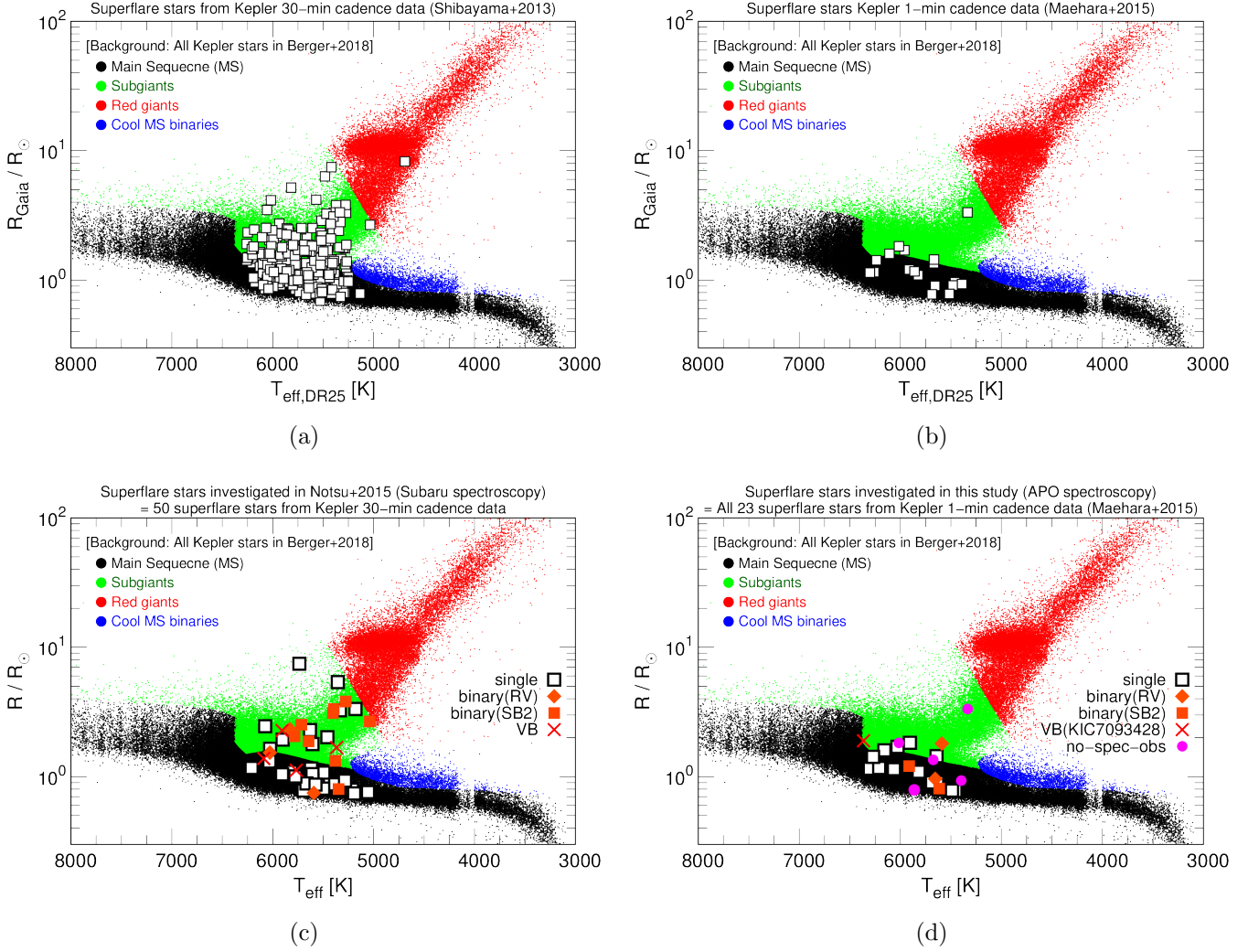


Figure 5. Stellar radius (R) vs. effective temperature T_{eff} of superflare stars. The background black, green, red, and blue circles are all the 177,911 *Kepler* stars listed in Berger et al. (2018) with R_{Gaia} (stellar radius based on *Gaia*-DR2 parallaxes) and $T_{\text{eff}, \text{DR25}}$ (temperature from DR25 *Kepler* Stellar Properties Catalog: Mathur et al. 2017). Each color corresponds to evolutionary state classification presented in Berger et al. (2018): main-sequence stars (black), subgiants (green), red giants (red), and cool main-sequence stars affected by binarity (blue).

(a) Superflare stars found from *Kepler* 30-min cadence data (Shibayama et al. 2013) that have R_{Gaia} values in Berger et al. (2018) are plotted with the open square points. The horizontal and vertical axes are R_{Gaia} and $T_{\text{eff}, \text{DR25}}$, respectively.

(b) Same as (a), but superflare stars from *Kepler* 1-min cadence data (Maehara et al. 2015) are plotted.

(c) Superflare stars that we have investigated with spectroscopic observations using Subaru telescope (Notsu et al. 2015a&2015b) are plotted. The open squares are the target superflare stars classified as single stars (Classifications are basically the same as those used in Appendix A.1 of this study). The orange diamonds (RV) and squares (SB2) correspond to the stars classified as binary stars because of radial velocity shifts and double-lined profiles, respectively. Visual binary stars are shown with the red cross marks. As for the radius value in the vertical axis and the temperature value in the horizontal axis, we use different types of the values for each star. The details are described in the main text of Section 5.1.

(d) The target superflare stars of this study, which are equal to all the 23 superflare stars from *Kepler* 1-min cadence data reported in Maehara et al. (2015), are plotted. The symbols and axes are used with the same way as (c). Pink circles correspond to the five faint superflare stars that we did not get spectra with enough S/N in this study (cf. Section 2).

Table 7. Number of solar-type superflare stars (N_{star}) and superflares on these stars (N_{flare}) found from *Kepler* 30-min time cadence data (cf. Figures 5(a) and 6)

	N_{star}	N_{flare}
(1) Original data (Shibayama et al. 2013)	279	1547
(2) Stars having R_{Gaia} values (Berger et al. 2018) among (1)	245	1402
(3) Stars identified as main sequence among (2) (cf. Figure 5(a))	136 (55.5%)	496
(4) Stars identified as subgiants among (2) (cf. Figure 5(a))	108 (44.1%)	905
(5) Stars identified as red giants among (2) (cf. Figure 5(a))	1 (0.4%)	1
(6) Stars with $T_{\text{eff,DR25}} = 5100 - 6000$ K among (3)	106	419
(7) Stars that was originally early K-dwarfs in Candelaresi et al. (2014) but are newly identified as solar-type stars with $T_{\text{eff,DR25}}$ and R_{Gaia} .	36	178
(8) (6)+(7)	142	597
(9) Stars having $\Delta F/F$ values in McQuillan et al. (2014) among (8)	113	527

Table 8. Number of solar-type superflare stars (N_{star}) and superflares on these stars (N_{flare}) found from *Kepler* 1-min time cadence data (cf. Figures 5(b) and 6)

	N_{star}	N_{flare}
(1) Original data (Maehara et al. 2015)	23	187
(2) Stars having R_{Gaia} values (Berger et al. 2018) among (1)	18	68
(3) Stars identified as main sequence among (2) (cf. Figure 5(b))	13 (2, 2) ^a	55 (15, 9) ^a
(4) Stars identified as subgiants among (2) (cf. Figure 5(b))	5 (0, 2) ^a	13 (0, 9) ^a
(5) Stars identified as red giants among (2) (cf. Figure 5(b))	0	0
(6) Stars with $T_{\text{eff,DR25}} = 5100 - 6000$ K among (3)	10	51
(7) Stars having $\Delta F/F$ values in McQuillan et al. (2014) among (6)	8	48

^a Numbers in parentheses show the stars identified as binary and the stars that we have not conducted spectroscopic observations because they are too faint, respectively, on the basis of our APO3.5m spectroscopic observations in this study (see also Figure 5(d) and Table 1).

stars are classified as main-sequence, while the remaining 10 stars ⁷ are classified as subgiants, among all the 34 “single” target stars. Among the 16 “binary” target stars, only 5 stars are classified as main-sequence stars, while the remaining 11 stars ⁸ are as subgiants.

In Figure 5(d), we plot the target stars of the APO3.5m spectroscopic observation of this study, which are equal to all the 23 superflare stars found from *Kepler* 1-min cadence data (Maehara et al. 2015). The radius and temperature values in the vertical and horizontal axes are plotted with the basically same way as Figure 5(c), but R_{spec} values are used for “RV” binary stars if the stars have no R_{Gaia} values, and T_{eff} estimated from spectroscopic data are used for all “RV” binary stars. As a result, 9 stars are classified as main-sequence, while 4 stars ⁹ are as subgiants, among all the 13

⁷ KIC3626094, KIC6503434, KIC7420545, KIC8547383, KIC9412514, KIC9459362, KIC10252382, KIC10528093, KIC11455711, and KIC11764567.

⁸ KIC4045215, KIC4138557, KIC7264976, KIC7902097, KIC8479655, KIC9653110, KIC9764192, KIC9764489, KIC10120296, KIC10453475, and KIC11560431.

⁹ KIC4554830, KIC4742436, KIC6777146, and KIC8656342.

“single target stars. Among the 5 “binary” target stars, three stars are classified as main-sequence, while two stars¹⁰ are as subgiants. Moreover, among the remaining 5 stars that we did not get spectroscopic data with enough S/N in this study (cf. Section 2)¹¹, three stars are classified as main-sequence, while two stars¹² are as subgiants. In the following sections, we update statistical studies by using the data of the stars that we can newly classify as solar-type (G-type main-sequence) stars.

5.2. Starspot size and energy of superflares

Most of superflare stars show large amplitude brightness variations, and they suggest that the surface of superflare stars are covered by large starspots (cf. Section 4.4). Figure 6 shows the scatter plot of flare energy (E_{flare}) as a function of the spot group area (A_{spot}). The values of solar flares in Figure 6 are the same as those in our previous studies (Shibata et al. 2013; Notsu et al. 2013b; Maehara et al. 2015). We estimate bolometric energies (white light flare (WLF) energies) of solar flares from *GOES* soft X-ray (SXR) flux values. We use the relation that WLF energy (E_{WL}) is proportional to SXR flux (F_{SXR}): $E_{\text{WL}} \propto F_{\text{SXR}}$, on the basis of the results and detailed descriptions in Section 4.1 of Namekata et al. (2017). This relation is supported from the observational comparisons between WL and SXR data during flares (e.g., Figure 4 of Namekata et al. 2017), and are related with the well-known relation between Hard X-ray (HXR) flux and SXR flux during a flare (“Neupert effect”: Neupert 1968). As a result, we here assume that bolometric energies of B, C, M, X, and X10 class solar flares are 10^{28} , 10^{29} , 10^{30} , 10^{31} , and 10^{32} erg.

In Figure 6, A_{spot} of superflare stars were estimated from the normalized amplitude of light variations ($\Delta F/F$) by using the following equation (Shibata et al. 2013; Notsu et al. 2013b):

$$A_{\text{spot}} = \frac{\Delta F}{F} A_{\text{star}} \left[1 - \left(\frac{T_{\text{spot}}}{T_{\text{star}}} \right)^4 \right]^{-1}, \quad (3)$$

where A_{star} is the apparent area of the star, and T_{spot} and T_{star} are the temperature values of the starspot and photosphere of the star. In Figure 6(a), original values of superflares on solar-type stars reported in Shibayama et al. (2013) (from *Kepler* 30-min cadence data) and Maehara et al. (2015) (from *Kepler* 1-min cadence data) are plotted¹³ for comparisons with the results of this study. In these previous papers, we defined the amplitude ($\Delta F/F$) as the brightness range normalized by the average stellar brightness, in which the lower 99% of the distribution of the brightness difference from average, except for the flares, are included. A_{star} and T_{star} values were based on the stellar radius and temperature values used in these previous papers¹⁴, and we assumed $T_{\text{spot}} = 4,000$ K.

In this study, we newly updated both of the E_{flare} and A_{spot} values by using the latest $T_{\text{eff,DR25}}$ and R_{Gaia} values described in Section 5.1. First, from the superflare stars that we previously reported from *Kepler* 30-min & 1-min time cadence data (Shibayama et al. 2013; Candelaresi et al. 2014; Maehara et al. 2015) we selected the stars classified again as solar-type stars (main-sequence stars

¹⁰ KIC11551430A and KIC7093428.

¹¹ As also done for “SB2” and “VB” binary stars, R_{gaia} and $T_{\text{eff,DR25}}$ values are used if R_{gaia} exists. If not, $T_{\text{eff,DR25}}$ and $T_{\text{eff,DR25}}$ values are used.

¹² KIC10528093 and KIC10745663.

¹³ Figure 6(a) is basically the same as Figure 5 of Maehara et al. (2015), but we plot it again because of the following two reasons. It is helpful for readers to compare the original figure with the new one updated in this study. Second, the solid lines corresponding to Equation (5) were mistakenly plotted (the vertical axis values are factor 7 smaller than the correct values) in Figure 5 of Maehara et al. (2015), and then it is better to show the revised figure here.

¹⁴ In Shibayama et al. (2013), we used the values taken from the first *Kepler* Input Catalog (KIC: Brown et al. 2011). In Maehara et al. (2015), we used those from the latest one (the revised KIC) at that time (Huber et al. 2014).

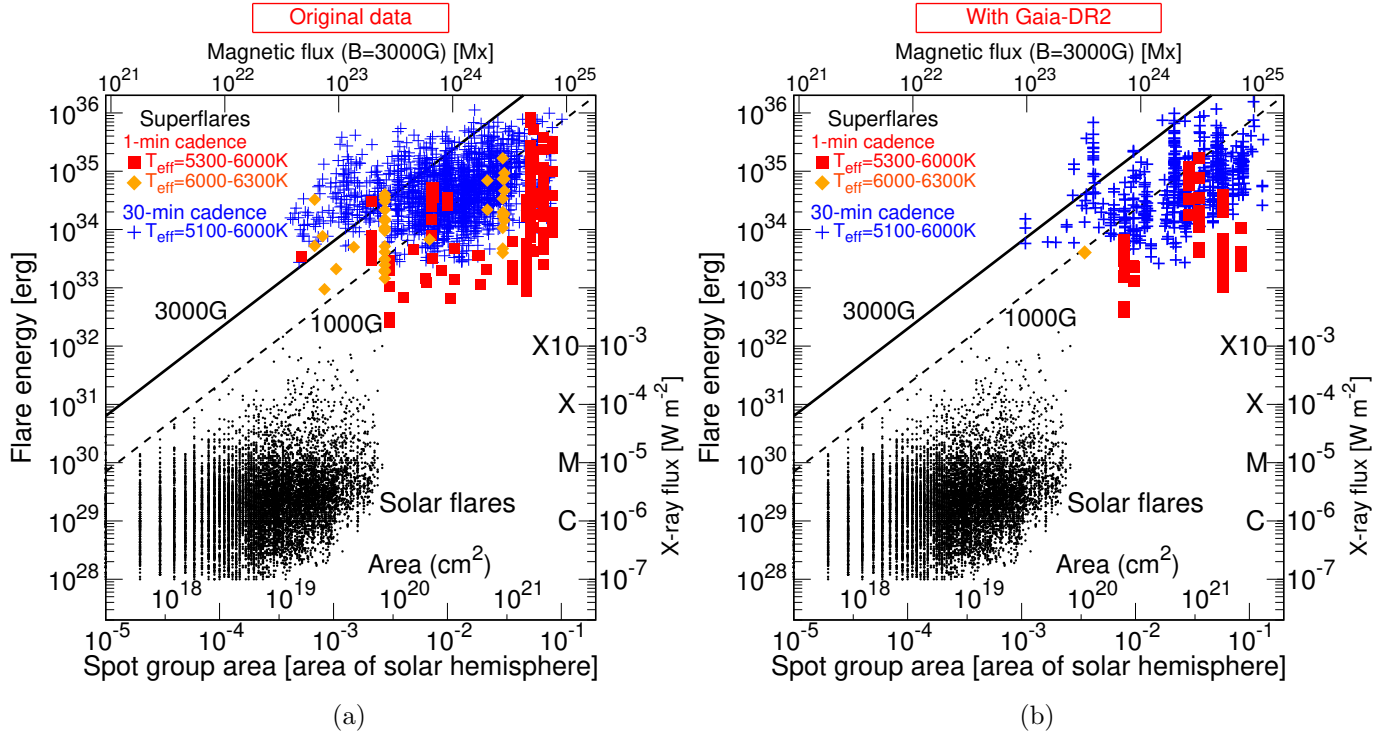


Figure 6. Scatter plot of flare energy (E_{flare}) as a function of spot area (A_{spot}) for solar flares and superflares. The lower and upper horizontal axes indicate the area of the spot group in the unit of the area of the solar hemisphere ($A_{1/2\odot} \sim 3 \times 10^{22} \text{ cm}^2$) and the magnetic flux for $B=3000 \text{ G}$. The vertical axis represents the bolometric energy released by each flare. The data of solar flares are completely the same as those in our previous studies (e.g., Figure 5 of Maehara et al. 2015). We assumed that bolometric energies of B, C, M, X, and X10 class solar flares are 10^{28} , 10^{29} , 10^{30} , 10^{31} , and 10^{32} erg from observational estimates of typical solar flare energies (See the main text for the details). The black solid and dashed lines correspond to the analytic relationship between the E_{flare} and A_{spot} from Equation (5) for $B=3000 \text{ G}$ and 1000 G , respectively.

(a) The original data of superflares on solar-type (G-type main-sequence) stars presented in our previous studies (Shibayama et al. 2013 & Maehara et al. 2015) are plotted. Blue crosses indicate 1549 superflares (on 279 stars) detected from *Kepler* 30-min cadence data (Shibayama et al. 2013), while red squares and orange diamonds are those (187 flares on 23 stars) detected from 1-min cadence data (Maehara et al. 2015). Among the 187 flares from 1-min cadence data, stars with $T_{\text{eff}} = 6000 - 6300$ K, which are not included in the range of solar-type stars in this study ($T_{\text{eff}} = 5100 - 6000$ K), are distinguished with orange diamonds.

(b) The data of superflares on solar-type stars updated in this study using $T_{\text{eff,DR25}}$ and R_{Gaia} values. Symbols are used with the same way as (a). In addition to the data of solar-type stars (blue crosses and red squares), the data of one main-sequence star with $T_{\text{eff}} = 6000 - 6300$ K (KIC8508009) from *Kepler* 1-min cadence data is also calculated and plotted for reference.

with $T_{\text{eff}} = 5100 - 6000$ K) on the basis of $T_{\text{eff,DR25}}$ and R_{Gaia} values (cf. Figure 5) (Line (6) of Tables 7 and 8). Not only “subgiants” and “red giants”, but also stars identified as “cool main-sequence binary” stars in Figure 5 are not included in the “solar-type” stars classified in this study.

As for the selection from *Kepler* 30-min cadence data, we used the data not only from [Shibayama et al. \(2013\)](#) (described in Figure 5 (a)) but also from [Candelaresi et al. \(2014\)](#). We investigated superflares on solar-type stars in [Shibayama et al. \(2013\)](#) and those on G,K,M-type stars in [Can-](#)

delaresi et al. (2014). Exactly the same *Kepler* dataset (the first 500 days : Quarters 0 – 6) are used for the flare surveys in these both studies, and the superflare data of Shibayama et al. (2013) (solar-type stars) exactly correspond to the subset of those of Candelaresi et al. (2014) (G,K,M-type stars). Then in this paper, we newly selected solar-type superflare stars not only from the original solar-type superflare stars in Shibayama et al. (2013) (cf. Figure 5(a)), but also from the stars originally identified as K,M-type stars in Candelaresi et al. (2014). 36 superflare stars originally identified as early K-type stars (with $T_{\text{eff}} = 4900 - 5100\text{K}$) in Candelaresi et al. (2014) are newly categorized as solar-type stars with the revised $T_{\text{eff,DR25}}$ and R_{Gaia} values (Line (7) of Tables 7). We note that these superflare stars were not included in Figure 5(a), but are included in the following discussions of solar-type superflare stars in this paper. As a result, 142 solar-type stars (with 597 superflares in total) from *Kepler* 30-min cadence data (Shibayama et al. 2013; Candelaresi et al. 2014) (Line (8) of Table 7) and 10 solar-type stars (with 51 superflares in total) from 1-min cadence data (Maehara et al. 2015) are selected (Line (6) of Table 8).

We then recalculated E_{flare} and A_{spot} for these selected data. The recalculation of E_{flare} was done by applying these updated $T_{\text{eff,DR25}}$ and R_{Gaia} values to the equations presented in Section 2.3 of Shibayama et al. (2013). As for A_{spot} , we used the new methods presented in Maehara et al. (2017). $\Delta F/F$ values taken from McQuillan et al. (2014) were used, and we applied the following relation on the temperature difference between photosphere and spot ($T_{\text{star}} - T_{\text{spot}}$) deduced from Berdyugina (2005):

$$\begin{aligned}\Delta T(T_{\text{star}}) &= T_{\text{star}} - T_{\text{spot}} \\ &= 3.58 \times 10^{-5} T_{\text{star}}^2 + 0.249 T_{\text{star}} - 808.\end{aligned}\quad (4)$$

As a result, we got the resultant values of the updated E_{flare} and A_{spot} values for 113 stars (with 527 flares in total) from *Kepler* 30-min cadence data (Shibayama et al. 2013; Candelaresi et al. 2014) (Line (9) of Table 7) and 8 stars (with 48 flares in total) from 1-min cadence data (Maehara et al. 2015) (Line (7) of Table 8). We note that only the stars having $\Delta F/F$ values in McQuillan et al. (2014) are selected here. These resultant superflare values are plotted in Figure 6(b).

In Figure 6, the majority of superflares occur on the stars with large starspots, though there is a large scatter. Flares are sudden releases of magnetic energy stored around starspots (cf. Shibata & Magara 2011). The total energy released by the flare (E_{flare}) must be smaller than (or equal to) the magnetic energy stored around starspots (E_{mag}). Our previous paper (e.g., Shibata et al. 2013) suggested that the upper limit of E_{flare} can be determined by the simple scaling law:

$$\begin{aligned}E_{\text{flare}} &\approx f E_{\text{mag}} \approx \frac{B^2 L^3}{8\pi} \approx \frac{B^2}{8\pi} A_{\text{spot}}^{3/2} \\ &\approx 7 \times 10^{32}(\text{erg}) \left(\frac{f}{0.1} \right) \left(\frac{B}{10^3 \text{G}} \right)^2 \left(\frac{A_{\text{spot}}}{3 \times 10^{19} \text{cm}^2} \right)^{3/2} \\ &\approx 7 \times 10^{32}(\text{erg}) \left(\frac{f}{0.1} \right) \left(\frac{B}{10^3 \text{G}} \right)^2 \left(\frac{A_{\text{spot}} / (2\pi R_{\odot}^2)}{0.001} \right)^{3/2},\end{aligned}\quad (5)$$

where f is the fraction of magnetic energy that can be released as flare energy, B and L are the magnetic field strength and size of the spot, and R_{\odot} is the solar radius. The black solid and dashed lines in Figure 6 represent Equation (5), and almost all the solar flare data located below these lines.

As for the original superflare data from our previous papers (Figure 6(a)), many of the superflares locate below the solid line, but some of them locate above this line. Our previous papers (e.g., Notsu et al. 2013b & 2015b) considered that these stars above this line are expected to have low inclination angle or have starposts around the pole region. In contrast, as for the new data of superflares updated in this study (Figure 6(b)), the number of flares above this line (Equation (5) with $B=3000$ G) looks to be decreased and much higher fraction of superflares locate below this line. In order to see this point more clearly, we plot only the maximum energy flare of each superflare star in Figures 7 (a) & (b), and compare them using histograms in Figure 8. The number of stars above the black solid line (the upper limit line from Equation (5) with $B=3000$ G and the inclination angle $i=90^\circ$) is significantly decreased. With these updates, it is more strongly supported that the upper limit of the energy released by the flare is not inconsistent with the magnetic energy stored around the starspots.

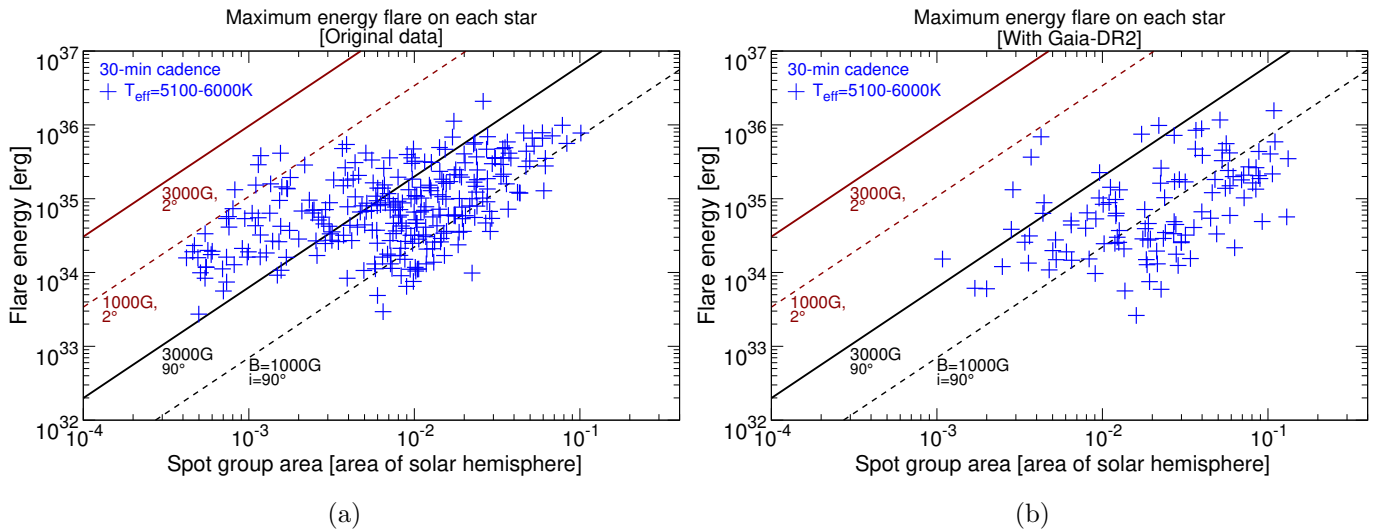


Figure 7. (a) Scatter plot of flare energy (E_{flare}) as a function of spot area (A_{spot}) for superflares (as Figure 6), but the maximum energy flare of each superflare star from *Kepler* 30-min cadence data using the original data in Shibayama et al. (2013) are only plotted. The black solid and dashed lines correspond to the analytic relationship between the E_{flare} and A_{spot} from Equation (5) with the inclination angle $i = 90^\circ$ for $B=3000$ G and 1000 G, respectively. The dark-red solid and dashed lines correspond to the same relationship with $i = 2^\circ$ for $B=3000$ G and 1000 G, respectively.

(b) Same as (a), but the maximum energy flare of each superflare star from *Kepler* 30-min cadence data using the data updated with $T_{\text{eff},\text{DR25}}$ and R_{Gaia} in this study are only plotted.

Next, we see this point (the difference of the number of superflare stars above Equation (5) between the previous studies and this study) a bit more in detail by incorporating the results of our spectroscopic studies in Section 4. In Figure 2 in Section 4.3, we compared the projected rotational velocity ($v \sin i$) with the stellar rotational velocity (v_{lc}) on the basis of our spectroscopic observations (Notsu et al. 2015b and this study), and stellar inclination angle (i) can be calculated using Equation (2). We plot again the data of single superflare stars in Figure 9. In this figure, we newly classified solar-type stars by using spectroscopically-measured temperature ($T_{\text{eff,spec}}$) and stellar radius values (R_{gaia} or R_{spec}) in Figures 5(c)&(d). White open symbols and black filled ones are solar-type stars (main-sequence stars with $T_{\text{eff}} = 5100 - 6000$ K). The former points are the stars having A_{spot} values

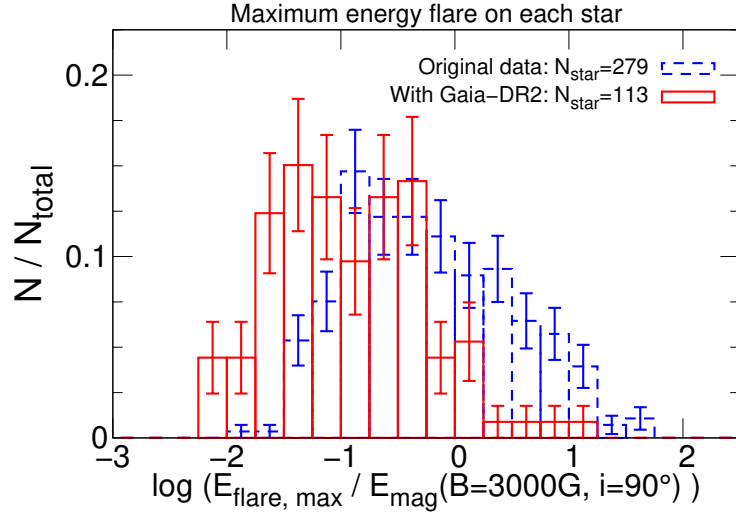


Figure 8. Histograms showing the distribution of the maximum energy flare of each superflare star ($E_{\text{flare,max}}$) found from *Kepler* 30-min time cadence data. The horizontal axis value is the fraction of $E_{\text{flare,max}}$ to the upper limit magnetic energy (E_{mag}). E_{mag} values correspond to the black solid lines in (a)&(b) ($B=3000$ G and $i=90^\circ$) at A_{spot} value of each star. The blue dashed line corresponds to the original superflare data shown in Figure 7(a), while the red solid line corresponds to the updated data in Figure 7(b). The error bars represent the 1- σ uncertainty estimated from the square root of the number of stars in each bin.

deduced from $\Delta F/F$ in McQuillan et al. (2014) so that we can plot the data points in Figure 10(b), but the latter ones are the stars without $\Delta F/F$ values in McQuillan et al. (2014) so that we cannot plot the data in Figure 10(b). Orange and green symbols correspond to the main-sequence stars with a bit hotter ($T_{\text{eff}} = 6000 - 6300$ K) and a bit cooler ($T_{\text{eff}} = 5000 - 5100$ K) temperature values, respectively. Red symbols are the stars classified as subgiants (cf. Section 5.1). As a result, many of the low-inclination angle stars are not classified as solar-type stars in this study.

Then, in Figures 10(a) & (b), we overplotted the maximum energy flare data of these spectroscopically observed superflare stars on the data of Figures 7 (a) & (b), respectively. In Figure 10 (a), the starspot size and flare energy data of the overplotted stars are taken from those used in Figure 7 (a)¹⁵. As for Figure 10(b), we update starspot size and flare energy values of the overplotted stars by recalculating them with $T_{\text{eff,spec}}$ and stellar radius values (R_{gaia} or R_{spec}) used in Figures 5(c) & (d). The equations used for these recalculations are the same as those used for Figures 6(b) & 7 in the above. Notsu et al. (2015b) suggested that many of the data points located in upper-left side of A_{spot} vs. E_{flare} diagram tend to have low inclination angle values. This tendency can also be seen in Figure 10(a), but most of these low-inclination angle stars are now classified as subgiant stars (i.e. red points in this figure). In the updated Figure 10(b), the data points locate in more right-bottom side of this diagram. There is only one star above the black solid line (Equation (5)). However, the

¹⁵ We note that three spectroscopically investigated stars (KIC7420545, KIC6934317, and KIC8429280) that are not in Figure 7(a) are also included in this figure. These stars were not included in the data of Shibayama et al. (2013), but have been spectroscopically investigated in our previous papers (see a footnote of Table 1 of Notsu et al. 2015b).

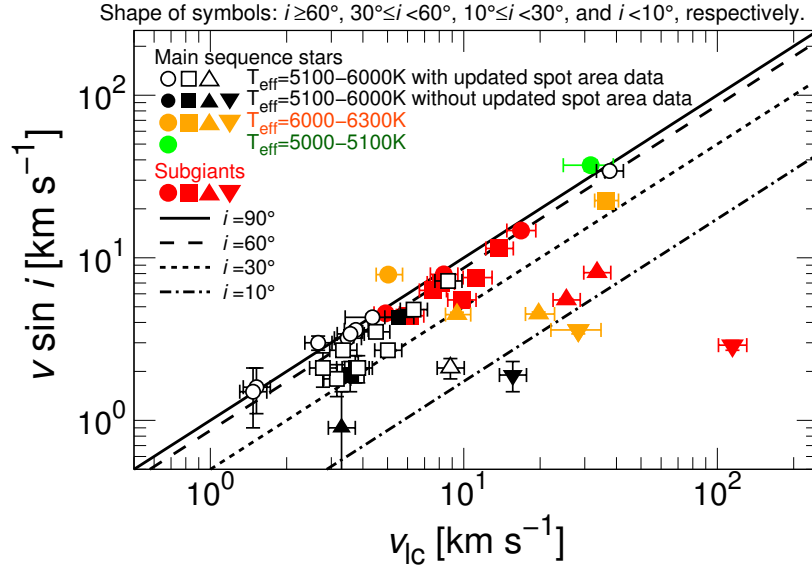


Figure 9. Projected rotational velocity ($v \sin i$) vs. the stellar rotational velocity (v_{lc}) estimated from the period of the brightness variation (P_{rot}) and stellar radius (R). The datapoints are the basically the same as those of Figure 2 in Section 4.3, but are limited to single superflare stars. The three single stars (KIC11652870, KIC4554830, and KIC11253827, which are shown with blue triangles in Figure 2) that have only $v \sin i$ upper limit values in APO data (and no values from Subaru data) are removed from this figure since we cannot estimate their inclination angle values correctly. They are classified with colors and shapes of the symbols on the basis of the stellar type classifications (see the main text for the details) and inclination angles (circles: $i \geq 60^\circ$, squares: $30^\circ < i \leq 60^\circ$, upward triangles: $10^\circ < i \leq 30^\circ$, and downward triangles: $i < 10^\circ$), respectively. The solid line represents the case that our line of sight is vertical to the stellar rotation axis ($i = 90^\circ$; $v \sin i = v_{lc}$). We also plot three different lines, which correspond to smaller inclination angles ($i = 60^\circ$, 30° , 10°).

number of stars is decreased in Figure 10(b) compared with Figure 10(a), and we need to increase the number of target stars with more spectroscopic observations in the future.

Finally in Figures 11(a) & (b), we plot again A_{spot} and E_{flare} values (taken from Figure 6(b)), separating the superflare data on the basis of the stellar temperature values. The data of the stars with a temperature range ($T_{\text{eff}} = 5600 - 6000$ K) close to the solar temperature are plotted in Figure 11(b), while those of late G-type main-sequence stars ($T_{\text{eff}} = 5100 - 5600$ K) are in Figure 11(a). There are no big differences between Figures 11(a) & (b). As a result, almost all the data points of superflares locate below the line of Equation (5), and we confirmed again that the upper limit of the energy released by flares is not inconsistent with the magnetic energy stored around the starspots.

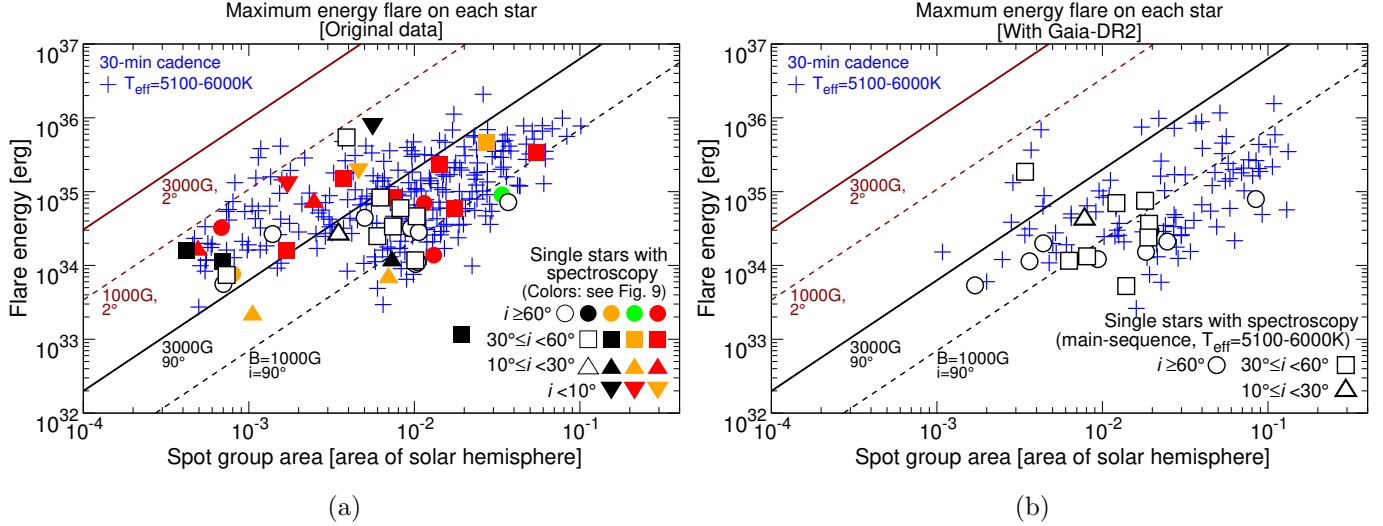


Figure 10. (a) Same as Figure 7(a), but the data of maximum energy flares on single superflare stars that we have spectroscopically investigated (Figure 9) are overplotted with bigger points. The colors and shapes of the overplotted symbols are used with the basically the same way as Figure 9.
(b) Same as Figure 7(b), but the maximum energy flares on single superflare stars that we have spectroscopically investigated (Figure 9) are overplotted using the updated values (see the main text for the details). Different from Figure 10(a), only the stars categorized as solar-type stars in this study are plotted. The shapes of the overplotted symbols (open points) are used with the basically the same way as Figure 9.

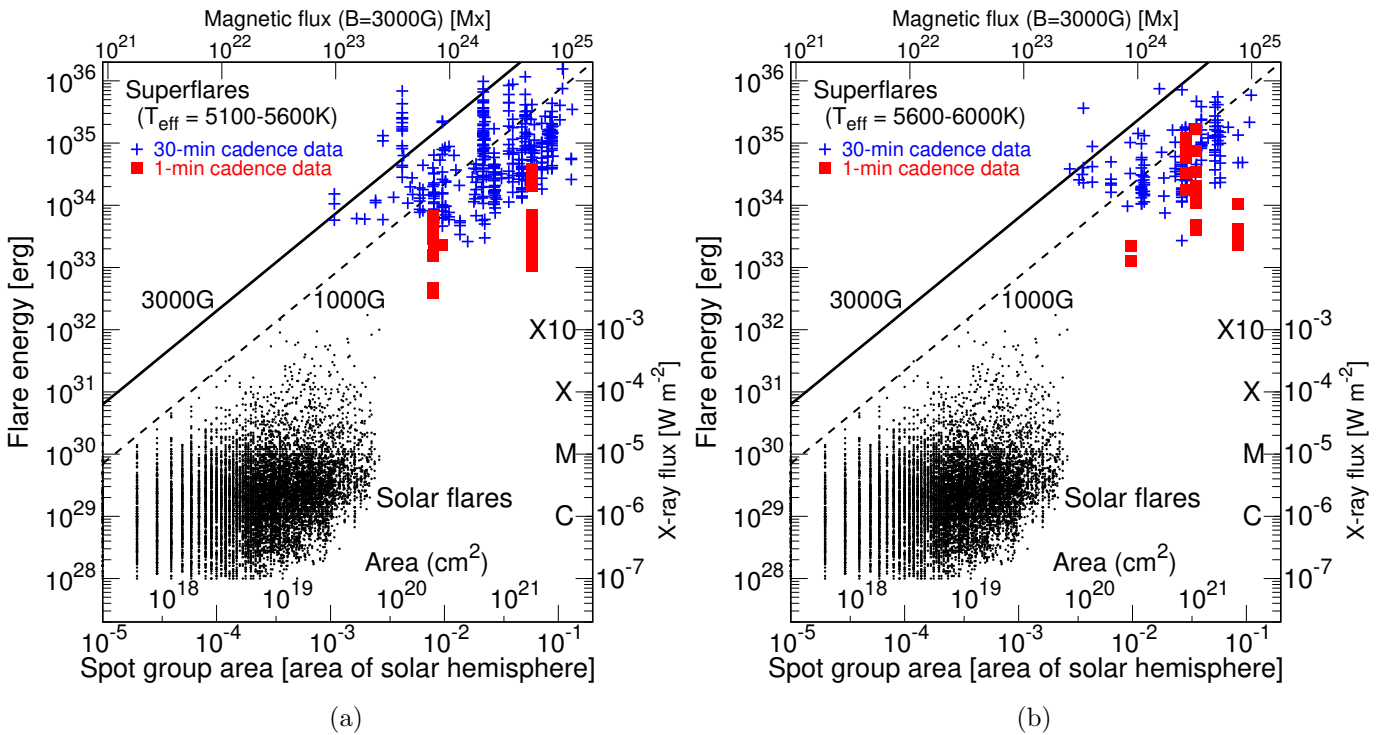


Figure 11. The scatter plot of flare energy (E_{flare}) as a function of spot area (A_{spot}) of solar flares and superflares (as Figure 6(b)). Blue plus marks and red filled squares are the data of superflares found from *Kepler* 30-min and 1-min time cadence data, which are originally in Figure 6(b). They are separated into (a) and (b) on the basis of the stellar temperature values: (a) $T_{\text{eff}} = 5100 - 5600$ K and (b) $T_{\text{eff}} = 5600 - 6000$ K.

5.3. Dependence of superflare energy and frequency on rotation period

Previous observations of solar-type stars (e.g., X-ray, UV, Ca II H&K) have shown that the stellar magnetic activity level decreases as rotation period increases (e.g., Noyes et al. 1984; Güdel 2007; Wright et al. 2011). Since stellar age has a good correlation with rotation, young rapidly-rotating stars show the higher activity levels, and it was expected that they show more energetic flares more frequently compared with slowly-rotating stars like the Sun. In our previous paper (Notsu et al. 2013b), we investigated the relationship between the superflare energy (E_{flare}), and the rotation period (P_{rot}), and suggested that the maximum superflare energy in a given rotation period bin does not have a clear correlation with the rotation period (Figure 12(a) of this paper), while the average flare frequency in a given period bin has a correlation with the rotation (Figure 7(b) of Notsu et al. 2013b and Figure 2 of Maehara et al. 2015). This suggestion is important since, against the above mentioned previous expectations, energetic superflares with $\sim 10^{35}$ erg can occur on solar-type stars rotating as slow as the Sun ($P_{\text{rot}} \sim 25$ days), even though the frequency is low (once in a few thousand years), compared with rapidly-rotating stars.

Next, we investigate again this relation by using superflare values updated with *Gaia*-DR2 stellar radius (R_{Gaia}) data. In Section 5.2, we newly classified solar-type stars on the basis of $T_{\text{eff,DR25}}$ and R_{Gaia} , and recalculated flare energy E_{flare} . Figure 12(b) shows the relationship between this updated E_{flare} value with the rotation period P_{rot} of each solar-type superflare star. P_{rot} values plotted here

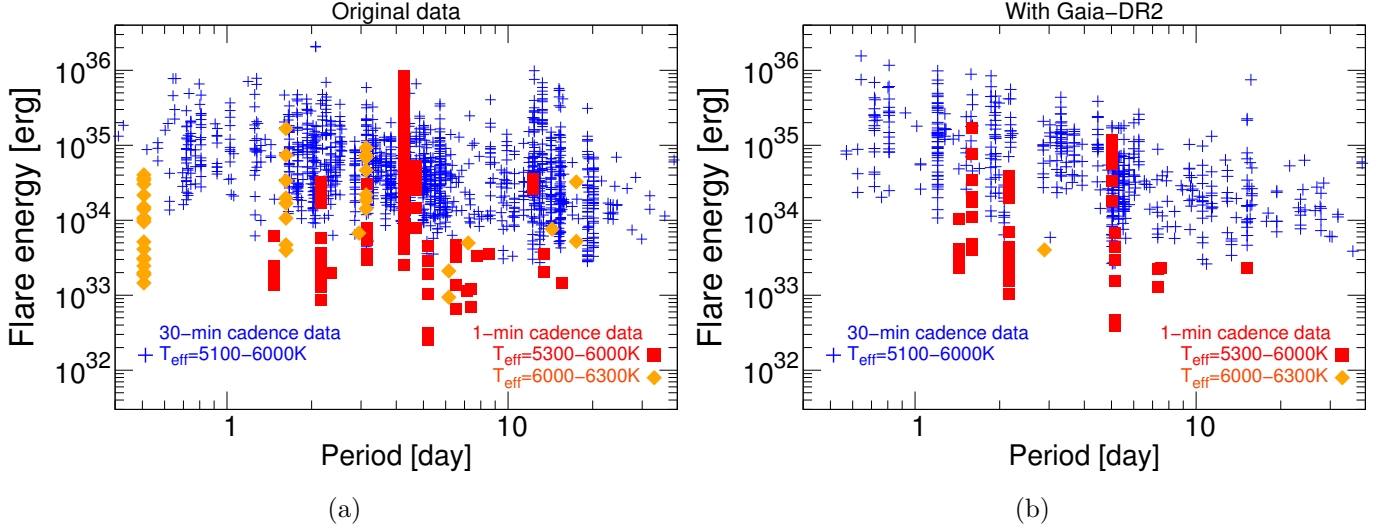


Figure 12. Scatter plot of the superflare energy (E_{flare}) vs. the rotation period (P_{rot}) of each star (estimated from the brightness variation period). Apparent negative correlations between P_{rot} and the lower limit of E_{flare} , which are mainly seen for blue cross points, result from the detection limit of our flare search method (cf. Shibayama et al. 2013).

(a) The original data of superflares on solar-type (G-type main-sequence) stars presented in our previous studies (Shibayama et al. 2013 & Maehara et al. 2015) are plotted. Blue crosses indicate superflares detected from *Kepler* 30-min cadence data (Shibayama et al. 2013), while red squares and orange diamonds are those detected from 1-min cadence data (Maehara et al. 2015). Among the flares from 1-min cadence data, stars with $T_{\text{eff}} = 6000 - 6300$ K, which are not included in the range of solar-type stars in this study ($T_{\text{eff}} = 5100 - 6000$ K), are distinguished with orange diamonds.

(b) The data of superflares updated in this study using $T_{\text{eff,DR25}}$ and R_{Gaia} values. Symbols are used with the same way as (a). In addition to the data of solar-type stars (Blue crosses and red squares), the data of one main-sequence star with $T_{\text{eff}} = 6000 - 6300$ K (KIC8508009) from *Kepler* 1-min cadence data is also calculated and plotted for reference.

are taken from McQuillan et al. (2014). Unlike the results of our previous studies (Figure 12 (a)), Figure 12(b) suggests that the upper limit of E_{flare} in each period bin has a continuous decreasing trend with rotation period. For example, stars rotating as slow as the Sun ($P_{\text{rot}} \sim 25$ days) show superflares up to 10^{35} erg, while rapidly-rotating stars with $P_{\text{rot}}=1 - 3$ days have more energetic superflares up to 10^{36} erg.

Flare activity also depends on stellar temperature (Candelaresi et al. 2014; Davenport 2016; Van Doorsselaere et al. 2017), and even among solar-type stars, cooler stars can have higher flare activities (cf. Figure 5 of Shibayama et al. 2013). Then the data of superflares plotted in Figure 13 are separated into (a) and (b) on the basis of the stellar temperature values. The data of the stars with a temperature range ($T_{\text{eff}} = 5600 - 6000$ K) close to the solar temperature are plotted in Figure 13(b), while those of late G-type main-sequence stars ($T_{\text{eff}} = 5100 - 5600$ K) are in Figure 13(a). In Figure 13(b), we also added the scale of stellar age (t) on the basis of the gyrochronology relation of solar-type star ($t \propto P_{\text{rot}}^{0.6}$: Ayres 1997) in order to compare the age of superflare stars with that of the Sun ($t=4.6$ Gyr). The scale of t are only plotted in the limited age range $t = 0.5 - 5$ Gyr because of the following two reasons. (1) As for young solar-type stars with $t \lesssim 0.5 - 0.6$ Gyr, a large scatter

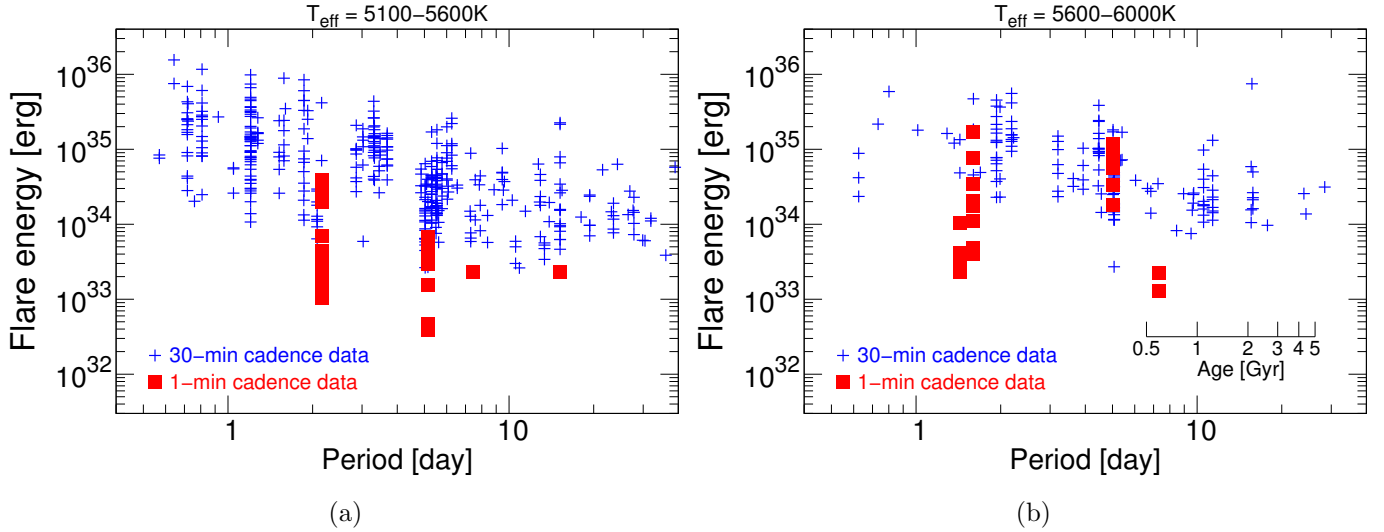


Figure 13. Scatter plot of the superflare energy (E_{flare}) vs. the rotation period (P_{rot}) of each star (as Figure 12(b)). Blue plus marks and red filled squares are the data of superflares found from *Kepler* 30-min and 1-min time cadence data, which are originally in Figure 12(b). They are separated into (a) and (b) on the basis of the stellar temperature values: (a) $T_{\text{eff}} = 5100 - 5600 \text{ K}$ and (b) $T_{\text{eff}} = 5600 - 6000 \text{ K}$. Only in (b), we added the scale of stellar age (t) on the basis of the gyrochronology relation of solar-type star ($t \propto P_{\text{rot}}^{0.6}$: Ayres 1997) (See main text for the details).

in the age-rotation relation has been reported from young cluster observations (e.g., Soderblom et al. 1993; Ayres 1997; Tu et al. 2015). (2) As for old solar-type stars beyond solar-age ($t=4.6$ Gyr), a breakdown of gyrochronology relations has been recently reported (van Saders et al. 2016; Metcalfe & Egeland 2018). With this scale, for example, we can see that Sun-like stars with $P_{\text{rot}} \sim 25$ days are more than four times older ($t \sim 4.6$ Gyr) than the stars with $P_{\text{rot}} \sim 10$ days ($t \sim 1$ Gyr).

As a result of Figures 13 (a) & (b), we confirmed again the suggestions from Figures 12 (b). The upper limit of superflare energy in each period bin depends on the rotation period in both Figures 13 (a) & (b), and there is one order of magnitude difference between the maximum flare energy on young stars ($t < 0.5$ Gyr) and Sun-like old stars ($t \sim 4.6$ Gyr). We cannot judge whether there are any clear differences between these two figures because of the low-number statistics. It is necessary to increase the number of superflare data with the future observations (See also Section 6.3).

Then we see the relation between flare frequency and rotation period by using the updated superflare data. Figure 14 shows that the average flare frequency in a given period bin tends to decrease as the period increases in the range of P_{rot} longer than a few days. The frequency is averaged from all of the superflare stars in the same period bin. This result is basically the same as that presented in Notsu et al. (2013b) with the original superflare data. The frequency of superflares on young rapidly-rotating stars ($P_{\text{rot}}=1 - 3$ days) is ~ 100 times higher compared with old slowly-rotating stars ($P_{\text{rot}} \sim 25$ days), and this indicates that as a star evolves (and its rotational period increases), the frequency of superflares decreases. We can now interpret that this correlation between the rotation period (roughly corresponding to age) and flare frequency is consistent with the correlation between the rotation period (age) and previous measurement of the stellar activity level such as the average X-ray luminosity (e.g., Noyes et al. 1984; Güdel 2007; Wright et al. 2011). Summarizing the results in this section, superflares with their energy $\lesssim 5 \times 10^{34}$ erg can occur on slowly-rotating old Sun-

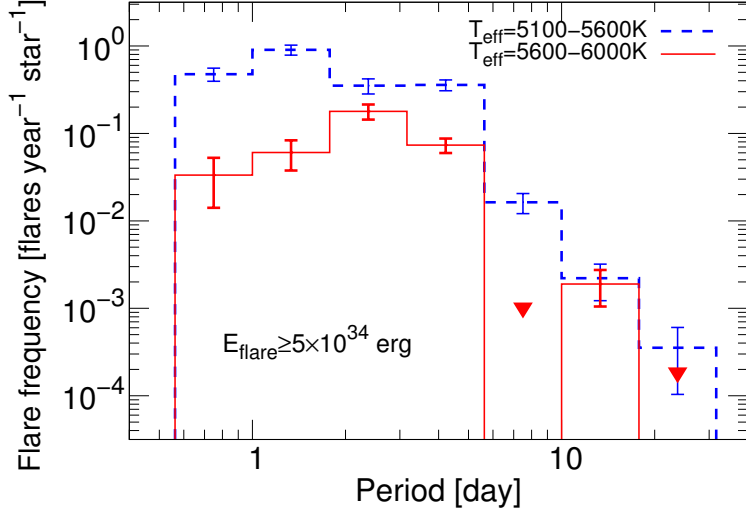


Figure 14. Occurrence frequency distribution of superflares as a function of the rotation period (P_{rot}), using the data of superflares on solar-type stars that were originally found from *Kepler* 30-min cadence data (Shibayama et al. 2013; Candelaresi et al. 2014) but are updated with $T_{\text{eff,DR25}}$ and R_{Gaia} in this study (E_{flare} and P_{rot} data in Figure 12). The vertical axis indicates the number of superflares with energy $\geq 5 \times 10^{34}$ erg per star and per year. The error bars represent the $1-\sigma$ uncertainty estimated from the square root of the number of flares in each bin. Unlike Figure 7 of Notsu et al. (2013b), we do not take into account the error values of E_{flare} since this is now more reliable with *Gaia*-DR2 stellar radius values. This vertical axis value is calculated by using the number of the solar-type stars in each P_{rot} bin ($N_P(P_{\text{rot}})$ in Table 9) detected in McQuillan et al. (2014). The potential errors from this $N_P(P_{\text{rot}})$ value are discussed in Appendix B. Red solid lines correspond to the frequency values calculated from the solar-type stars with their temperature values limited to a range ($T_{\text{eff}} = 5600 - 6000$ K) close to the solar temperature, while blue dashed lines are those from the late G-type main-sequence stars with $T_{\text{eff}} = 5100 - 5600$ K. $T_{\text{eff,DR25}}$ values are used for the temperature classifications here. As for the red solid lines, in the case of no events in a period bin, the upper limit values are shown with the red downward triangle points assuming less than one event occur in each bin.

like stars similar to the Sun ($T_{\text{eff}} = 5600 - 6000$ K, $P_{\text{rot}} \sim 25$ days and $t \sim 4.6$ Gyr), even though the frequency and maximum flare energy are lower compared with young rapidly-rotating stars and cooler stars.

5.4. Starspot size vs. rotation period of solar-type stars, and implications for superflare energy.

Our previous paper Maehara et al. (2017) investigated the statistical properties of starspots on solar-type stars by using the starspot size A_{spot} and rotation period P_{rot} estimated from the brightness variations of *Kepler* data. Here we update these values by using *Gaia*-DR2 stellar radius, as also done for superflare stars in the above. As done in Maehara et al. (2017), we used P_{rot} and brightness variation amplitude $\Delta F/F$ values reported in McQuillan et al. (2014). We newly classified 49212 solar-type stars (N_{data} in Table 9 in Appendix B) among the stars in McQuillan et al. (2014) by using $T_{\text{eff,DR25}}$ and R_{Gaia} values, as done for superflare stars in Section 5.2. P_{rot} and $\Delta F/F$ values of 11594 stars (cf. $N_P(\text{all})$ values in Table 9) are detected among these 49212 stars. Then, we recalculated A_{spot} values from $\Delta F/F$ values, using these $T_{\text{eff,DR25}}$ and R_{Gaia} values. The method of

A_{spot} calculation is exactly the same as those used for superflare stars in Section 5.2. The resultant values of are plotted in Figure 15. The data in Figure 15 are separated into (a) and (b) on the basis of the temperature values. The data of the stars with a temperature range ($T_{\text{eff}} = 5600 - 6000$ K) close to the solar temperature are plotted in Figure 15(b), while those of late G-type main-sequence stars ($T_{\text{eff}} = 5100 - 5600$ K) are in Figure 15(a). The stars showing superflares tend to have shorter rotation periods (younger ages) and larger starspot areas.

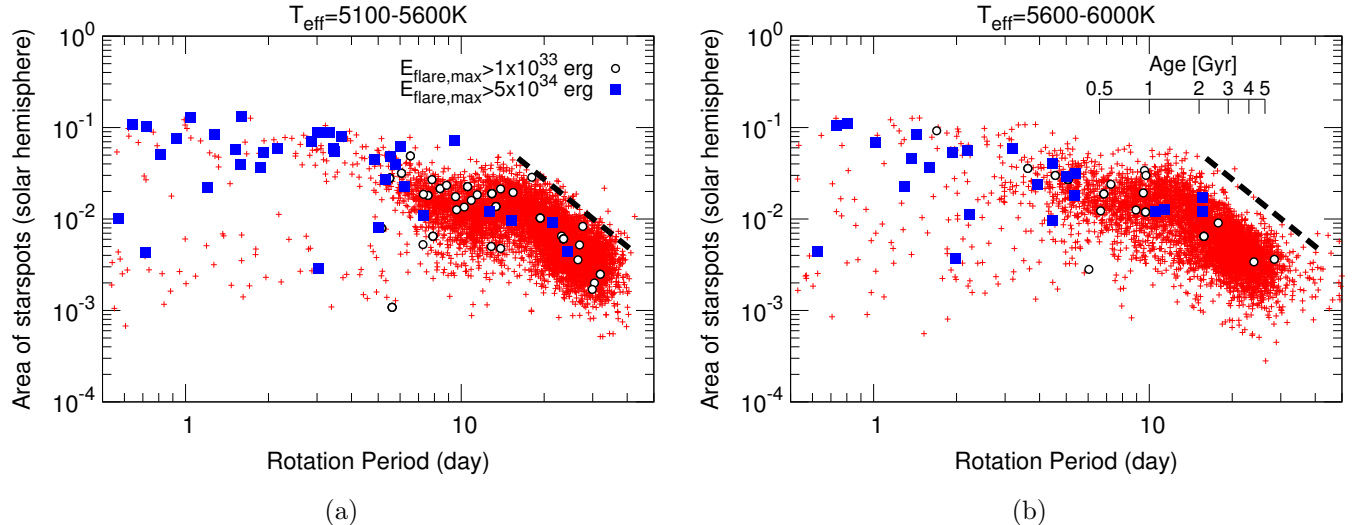


Figure 15. Scatter plot of the spot group area of solar-type stars (A_{spot}) as a function of the rotation period (P_{rot}), using the data updated with $T_{\text{eff,DR25}}$ and R_{Gaia} values in this study. The vertical axis represents A_{spot} in units of the area of solar hemisphere ($A_{1/2\odot} \sim 3 \times 10^{22} \text{ cm}^2$). Open circles and blue filled squares indicate solar-type stars that have superflares with the energy values of their most energetic flares $E_{\text{flare,max}} > 1 \times 10^{33} \text{ erg}$ and $E_{\text{flare,max}} > 5 \times 10^{34} \text{ erg}$, respectively. Red small cross marks indicate solar-type stars without superflares. The plotted data are separated into (a) and (b) on the basis of the temperature values: (a) $T_{\text{eff}} = 5100 - 5600$ K and (b) $T_{\text{eff}} = 5600 - 6000$ K. The black dashed line in (a) is plotted by eye to roughly show the upper limit of the datapoints in the range of $P_{\text{rot}} \gtrsim 14$ days. The black dashed line in (b) is plotted at the same place as (a) in order for comparison with the results of (a). Only in (b), we also added the scale of stellar age (t) on the basis of the gyrochronology relation of solar-type star ($t \propto P_{\text{rot}}^{0.6}$: Ayres 1997) (See the main text of Section 5.3 for the details).

Figure 15(b) shows that the largest area of starspots on Sun-like stars with $T_{\text{eff}} = 5600 - 6000$ K in a given period bin has roughly a constant or very gentle decreasing trend around $A_{\text{spot}} = 5 \times 10^{-2} - 1 \times 10^{-1} A_{1/2\odot}$ in the period range of $P_{\text{rot}} \lesssim 12$ days (age: $t \lesssim 1.4$ Gyr). However, in the period range of $P_{\text{rot}} \gtrsim 12$ days ($t \gtrsim 1.4$ Gyr), the largest starspot area on them clearly decreases as the rotation period increases. As for the late G-type main-sequence stars with $T_{\text{eff}} = 5100 - 5600$ K in Figure 15(a), the similar steep trends can be seen for maximum size of starspots, but the exact values are a bit different. This steep decreasing trend starts around $P_{\text{rot}} \sim 14$ days (Figure 15(a)). In the longer period range, the maximum area of spots on the stars with $T_{\text{eff}} = 5600 - 6000$ K at a given period bin is roughly half compared with those of the stars with $T_{\text{eff}} = 5100 - 5600$ K (see the black dashed line in Figure 15(b)). These differences support that cooler stars can generate larger magnetic flux more effectively thanks to the development of the convection zone. We discuss such temperature

differences of the P_{rot} vs. A_{spot} relations including more cooler (K and M-type) dwarf stars in more detail in our next study (Maehara et al. 2019 in preparation).

The trends similar to those presented here was already reported in Figure 1(a) of Maehara et al. (2017), but we did not discuss the temperature differences. Moreover, the steep decreasing trend in the longer period range is now much more clear compared with this previous paper. It might be because the error of A_{spot} values decrease thanks to the updates using *Gaia*-DR2 stellar radius (R_{Gaia}) values. and the potential contamination of subgiants in the previous data can also be eliminated. Then the steep decreasing trend of maximum spot area in the longer period range is more strongly supported.

In Section 5.3, we reported that maximum energy of superflares in a given period bin decreases as P_{rot} increases (Figures 13(a) & (b)). This decreasing trend of maximum flare energy can be related with the decreasing trend of maximum area of starspots in longer period regime in Figures 15 (a) & (b) described in this section. This is because the maximum area of starspots determines well the upper limit of flare energy (cf. Section 5.2). For example, Figure 15(b) shows that maximum size of starspots on old ($t \sim 4.6$ Gyr) Sun-like stars with $T_{\text{eff}} = 5600 - 6000$ K and $P_{\text{rot}} \sim 25$ days is $\sim 1\%$ of the solar hemisphere. This corresponds to flare energy of $10^{34} - 10^{35}$ erg on the basis of Equation (5), and the upper limit of superflare energy of such Sun-like stars in Figure 13 (b) are roughly in the same range.

However, there is a difference in a bit strict sense between the decreasing trend of the maximum superflare energy in Figures 13 (a) & (b) and that of the maximum area of starspots in Figures 15 (a) & (b). The maximum superflare energy roughly continuously decrease as the rotation period increases (the star becomes older) in Figures 13 (a) & (b), but the maximum area of starspots does not show such continuous decreasing trend in Figures 15 (a) & (b). The maximum area of starspots is constant in the short period range ($P_{\text{rot}} \lesssim 12 - 14$ days), but it steeply decreases as the period increases in the longer range ($P_{\text{rot}} \gtrsim 12 - 14$ days). This difference can suggest a possibility that the flare energy is determined not only by the starspot area but also by the other important factors, though the starspot area is still a necessary condition determining flare energy (cf. Section 5.2). By analogy with the correlation between the flare activity and the magnetic structure of sunspot groups (cf. Sammis et al. 2000; Maehara et al. 2017), one of the possible factors might be the effect of the magnetic structure of starspots. More complex spots can generate more frequent and more energetic flares according to solar observations. If the magnetic structure (complexity) of spots also has a correlation with the rotation period, the upper limit of flare energy can depend on rotation period even if the starspot size is roughly constant. We need to conduct more detailed studies on starspot properties to clarify such possibilities (See also the final paragraph of Maehara et al. 2017). We must note here that we also need more superflare observations to more quantitatively discuss the above difference between Figures 13 and 15, since the number of superflare events especially in Figure 13(b) is small.

In addition, the existence of constant and decreasing trends of maximum starspot coverage can be compared with the relation between soft X-ray flux and rotation period (e.g., Wright et al. 2011). The soft X-ray fluxes of solar-type stars are also known to show the constant regime (or so-called “saturation” regime) in the period range of $P_{\text{rot}} \lesssim 2-3$ days, but they decrease constantly as the P_{rot} values increase in the range of $P_{\text{rot}} > 2-3$ days. The changing point of this soft X-ray trend ($P_{\text{rot}} \sim 2-3$ days) is different from that of maximum spotsize values ($P_{\text{rot}} \sim 12 - 14$ days). Although

a detailed study on this point is beyond the scope of this paper, these similarities and differences can be interesting and helpful when considering the relation between stellar activity (including starspots, flares, X-ray steady emissions) and rotation in more detail.

5.5. *Superflare frequency on Sun-like stars and implications for the Sun*

Figure 16 represents the occurrence frequency distributions of superflares on solar-type stars with $T_{\text{eff}} = 5600 - 6000$ K (“the temperature range close to the solar value” in the above sections) and various rotation period (P_{rot}) values, derived from the superflare data updated in the above of this study. As also presented in our previous studies (e.g., [Shibayama et al. 2013](#)) with the original data of superflares, we can see that there are the power-law distributions ($dN/dE \propto E^{-\alpha}$ with the index $\alpha \lesssim 2$), and rapidly-rotating stars tend to have larger frequency values. The upper limit values of flare energy roughly depend on rotation period, as already seen in Figure 13. However, error values are relatively large especially for slowly-rotating stars, because of the small number of analyzed data. For example, one blue circle point in the energy range $E_{\text{flare}} = 10^{35.75-36.0}$ erg in Figure 16, which are a bit far from the other blue circle points, correspond to only one superflare event. We must note here that these values are treated with cautions, and we need to increase the number of slowly-rotating superflare stars by including more new data in the future.

We also note here that as the same as in Figure 14, the flare frequency value in vertical axis of Figure 16 is calculated by using the number of the solar-type stars in each P_{rot} bin ($N_P(P_{\text{rot}})$ in Table 9 in Appendix B) detected in [McQuillan et al. \(2014\)](#). The potential errors from this $N_P(P_{\text{rot}})$ value, which are discussed in Appendix B, should be kept in mind when we discuss the dependence of flare frequency on the rotation period on the basis of this Figure 16. For example, flare frequency of Sun-like stars with $P_{\text{rot}} = 20 - 40$ days could become factor two smaller in the largest error case, and more investigations with new data in the future are strongly needed.

Our previous papers ([Shibayama et al. 2013](#); [Maehara et al. 2015](#)) pointed out that the frequency distribution of superflares on Sun-like stars and those of solar flares are roughly on the same power-law line. However, the definition of Sun-like stars in these previous studies ($T_{\text{eff}} = 5600 - 6000$ K and $P_{\text{rot}} > 10$ days) include many stars much younger than the Sun. For example, stars with $P_{\text{rot}} \sim 10$ days have the age of $t \sim 1$ Gyr (cf. Figures 13(b) & 15(b)). It might be better to use only the data of stars rotating as slowly as Sun ($P_{\text{rot}} \sim 25$ days and $t \sim 4.6$ Gyr). Then in Figure 17, we newly plot the frequency value of superflares on Sun-like stars with $P_{\text{rot}} = 20 - 40$ days ($t > 3.2$ Gyr) taken from Figure 16, in addition to the data of solar flares and superflares shown in Figure 4 of [Maehara et al. \(2015\)](#). As a result, the newly added data point of superflares on Sun-like stars are roughly on the same power law-line, though the exact value of superflare frequency of stars with $P_{\text{rot}} = 20 - 40$ days ($t > 3.2$ Gyr) is a bit smaller than those of stars with $P_{\text{rot}} > 10$ days ($t > 1$ Gyr). From this figure, we can roughly remark that superflares with energy $> 10^{34}$ erg would be approximately once every 2000 – 3000 years on old Sun-like stars with $P_{\text{rot}} \sim 25$ days and $t \sim 4.6$ Gyr, though the error value is relatively large because of the small number of data of slowly-rotating stars.

We note here that several potential candidates of extreme solar flare events, which can be bigger than the largest solar flare in the past 200 years ($E_{\text{flare}} \sim 10^{32}$ erg), have been reported from the data over the recent 1000 – 2000 years (e.g., [Usoskin 2017](#) for review). For example, significant radioisotope ^{14}C enhancements have been reported in tree rings for the year 775AD and 994AD, and they suggest extremely strong and rapid cosmic-ray increase events possibly caused by extreme solar flares (e.g., [Miyake et al. 2012&2013](#)). Various potential low-latitude auroral drawings have been

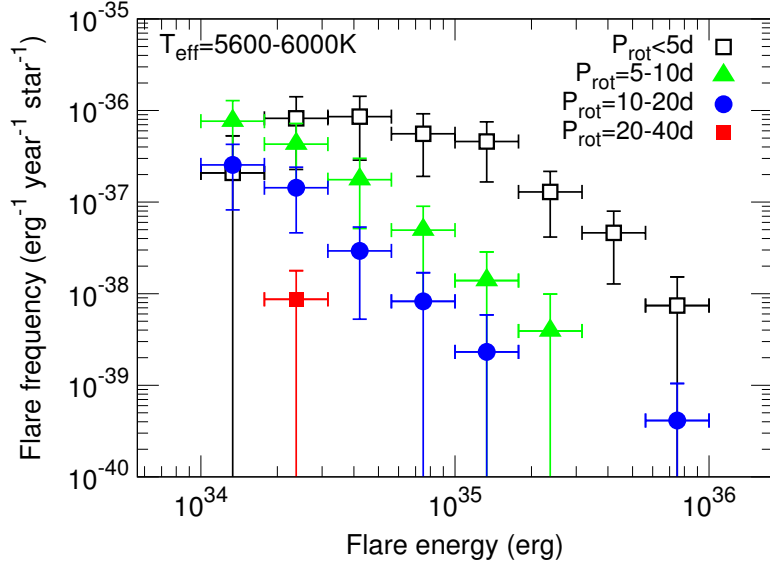


Figure 16. Occurrence frequency distribution of superflares on solar-type stars with $T_{\text{eff}} = 5600 - 6000$ K, using the superflare data that were originally found from *Kepler* 30-min cadence data (Shibayama et al. 2013; Candelaresi et al. 2014) but are updated using $T_{\text{eff,DR25}}$ and R_{Gaia} in this study. The flare energy values in the horizontal axis are limited to $10^{34} - 10^{36}$ erg since flare frequency in the range of $\lesssim 10^{34}$ erg can be heavily affected from the detection limit. The error bar in the horizontal axis direction corresponds to each energy bin. The vertical axis indicates the number of superflares per star, per year, and per unit energy in each energy bin. Error bars in the vertical axis represent $1-\sigma$ uncertainty of the frequency estimated from the $\sqrt{N+1}$ (N : the number of detected flares in each energy bin) considering Poisson statistics. Unlike the figures in our previous papers (e.g., Shibayama et al. 2013; Maehara et al. 2015), we do not take into account the error values of E_{flare} since this is now more reliable because of the *Gaia*-DR2 stellar radius values. The symbols are classified with rotation period (P_{rot}) values: open squares: $P_{\text{rot}} < 5$ days (age: $t < 0.5$ Gyr), green triangles: $P_{\text{rot}} = 5 - 10$ days ($t = 0.5 - 1$ Gyr), blue circles: $P_{\text{rot}} = 10 - 20$ days ($t = 1 - 3.2$ Gyr), and the red filled square: $P_{\text{rot}} = 20 - 40$ days ($t > 3.2$ Gyr). Age values here are taken from Figures 13(b) & 15(b).

also reported from the historical documents around the world, and they suggest the possibility that extreme solar flare events have occurred several times in the recent ~ 1000 years (e.g., Hayakawa et al. 2017a&2017b). In the future studies, the superflare frequency information as in Figure 17 should be compared with these radioisotope and historical data in detail.

5.6. Size frequency distribution of starspots and comparison with sunspots

In addition to the relation between the rotation period and starspot area in Section 5.4, in the following we also investigate the size frequency distribution of large starspot groups on Sun-like stars and that of sunspots. Our previous paper Maehara et al. (2017) already conducted this analysis, but here we aim to investigate again whether the both sunspots and larger starspots can be related to the same physical processes, by including the updates using *Gaia*-DR2 stellar radius values.

Figure 18 shows the comparison between the cumulative appearance frequency of starspots on Sun-like stars ($T_{\text{eff}} = 5600 - 6000$ K and $P_{\text{rot}}=20-40$ days) and that of sunspot groups. The estimation

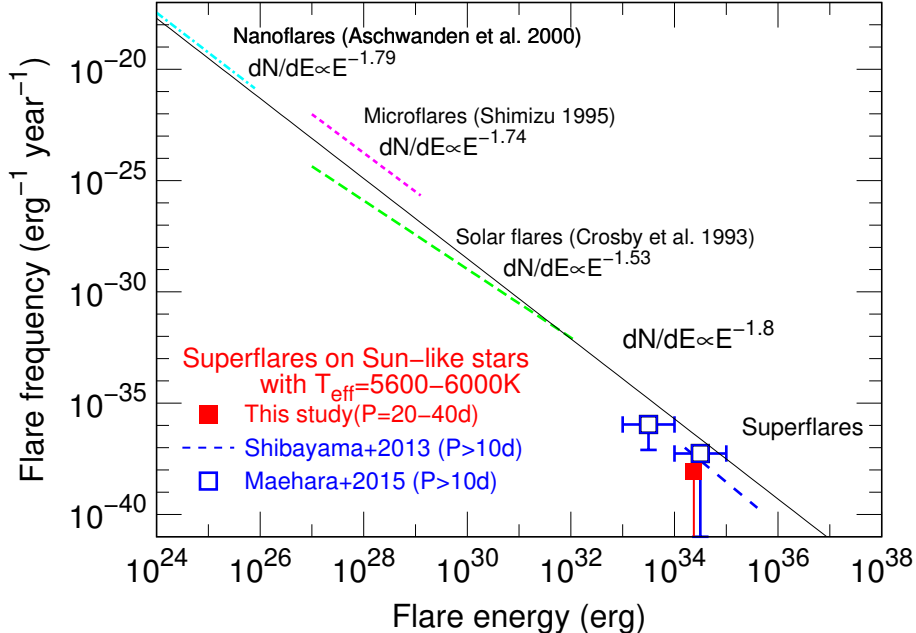


Figure 17. The comparison between the frequency distribution of superflares and solar flares. The red square, blue dashed line, and blue open squares indicate the occurrence frequency distributions of superflares on Sun-like stars (slowly-rotating solar-type stars with $T_{\text{eff}} = 5600 - 6000$ K). The red square corresponds to the updated frequency value of superflares on the stars with $P_{\text{rot}} = 20 - 40$ days, which are calculated in this study and presented in Figure 16. Horizontal and vertical error bars are the same as those in Figure 16. For reference, the blue dashed line and blue open squares are the values of superflares on the stars with $P_{\text{rot}} > 10$ days, which we presented in Figure 4 of Maehara et al. (2015) on the basis of original superflare data using *Kepler* 30-min cadence data (Shibayama et al. 2013) and 1-min cadence data (Maehara et al. 2015), respectively. Definitions of error bars of the blue open squares are the same as those in Figure 4 of Maehara et al. (2015). Three dashed lines in upper-left side of this figure indicate the power-law frequency distribution of solar flares observed in hard X-ray (Crosby et al. 1993), soft X-ray (Shimizu 1995), and EUV (Aschwanden et al. 2000). Occurrence frequency distributions of superflares on Sun-like stars and solar flares are roughly on the same power-law line with an index of -1.8 (black solid line) for the wide energy range between 10^{24} and 10^{35} erg.

method of the cumulative appearance frequency values is basically the same as that used for Figure 5 of Maehara et al. (2017), and this was already described in detail in that paper. Only one difference is that we use the updated A_{spot} values described in the above Section 5.4. The occurrence frequency decreases as the area of sunspots or starspots increases. The appearance rate of both the sunspot groups and that of starspots with the area $> 10^{-2.5} A_{1/2\odot}$ is approximately once in a few years. The cumulative appearance frequency of starspots on Sun-like stars can be fitted by a power-law function with the power-law index of -2.9 ± 0.5 (red dashed line) for spot areas between $10^{-2.5} - 10^{-1.0} A_{1/2\odot}$. This power-law index is a bit steeper compared with those originally presented in Maehara et al. (2017).

According to Bogdan et al. (1988), the size distribution of individual sunspot umbral areas shows lognormal distribution. Although the overall size-frequency distribution of sunspot groups in Figure

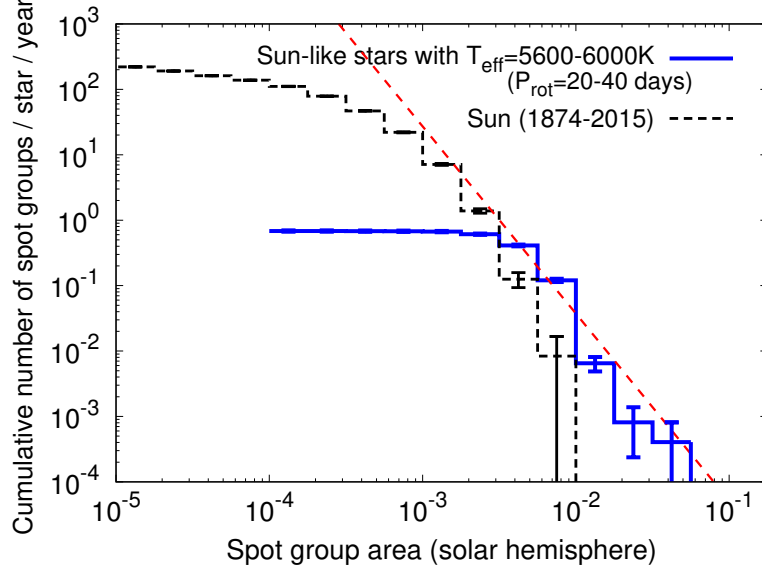


Figure 18. Comparison between the appearance frequency vs. spot area distribution of starspots on Sun-like stars and that of sunspot groups. Blue solid lines indicate the cumulative appearance frequency of starspots on Sun-like stars ($T_{\text{eff}} = 5600 - 6000 \text{ K}$ and $P_{\text{rot}} = 20 - 40 \text{ days}$). The value is almost constant in the spot area range below $2 \times 10^{-3} A_{1/2\odot}$ ($A_{1/2\odot} \sim 3 \times 10^{22} \text{ cm}^2$), and this is because the brightness variations of the stars with small starspots could not be detected, as mentioned in Maehara et al. (2017). Black dashed lines indicate the cumulative appearance frequency of sunspot groups as a function of the maximum area of each sunspot group, which are exactly the same data presented in Figure 5 of Maehara et al. (2017) (Then as for the details of the data description, see Maehara et al. 2017). The vertical error bars of these two lines indicate the square root of the number of stars in each bin. The red dashed line represents the power-law fit to the frequency distribution of starspots in the spot area range of $10^{-2.5} - 10^{-1.0} A_{1/2\odot}$. The power-law index of the line is -2.9 ± 0.5 .

18 also shows the similar log-normal distribution, the distribution of sunspot groups for large sunspots is roughly on this power-law line for sunspot areas between $10^{-3.25} - 10^{-2.5} A_{1/2\odot}$. The appearance frequency of sunspots with spot areas of $\sim 10^{-2} A_{1/2\odot}$ is about 10 times lower than that of starspots on Sun-like stars. This difference between the Sun and Sun-like stars might be caused by the lack of a “super-active” phase on our Sun during the last 140 years (Schrijver et al. 2012). These results shown here are basically the same as those originally presented in Maehara et al. (2017), and we confirmed the similarity between the size distribution of sunspots and that of starspots. This supports that the both sunspots and larger starspots could be related to the same physical processes. The upper limit of starspot size values of Sun-like stars in Figure 18 is \sim a few $\times 10^{-2} A_{1/2\odot}$ and the appearance frequency of these spots is approximately once every 2000 – 3000 years.

6. SUMMARY AND FUTURE PROSPECTS

This paper reports the latest view of superflares on solar-type stars found from our series of studies using *Kepler* data, by including the recent updates using Apache Point Observatory (APO) 3.5m telescope spectroscopic observations and *Gaia*-DR2 data.

6.1. *Summary of APO 3.5m telescope spectroscopic observations*

In Sections 2 – 4, we described the results of our spectroscopic observations of *Kepler* solar-type superflare stars. We newly conducted APO 3.5m telescope spectroscopic observations of the 18 solar-type superflare stars found from *Kepler* 1-min (short) time cadence data (Maehara et al. 2015).

- (i) More than half (43 stars) are confirmed to be “single” stars, among the 64 solar-type superflare stars in total that have been spectroscopically investigated so far in this APO3.5m observation and our previous Subaru/HDS (Notsu et al. 2015a) observations (Table 6).
- (ii) “ $v \sin i$ ” (projected rotational velocity) values are consistent with the rotational velocity values v_{lc} estimated from the brightness variation period of *Kepler* data (Figure 2).
- (iii) There is a positive correlation between the amplitude of the brightness variation and Ca II (Ca II 8542Å and Ca II H&K lines) index values (Figure 3), and this suggests that there is a rough positive correlation between the starspot coverage from *Kepler* photometric data and the stellar average magnetic field.
- (iv) The results of (ii)&(iii) support the idea that the quasi-periodic brightness variation of *Kepler* solar-type superflare stars is caused by the rotation with large starspots.
- (v) Lithium abundances of superflare stars suggest that *Kepler* solar-type superflare stars include many young stars but also include old stars like our Sun (Figure 4).

6.2. *Summary of the statistical properties of Kepler solar-type superflare stars incorporating Gaia-DR2 data*

Then in Section 5, we investigated the statistical properties of *Kepler* solar-type superflare stars originally described in our previous studies (Maehara et al. 2012, 2015, & 2017; Shibayama et al. 2013; Notsu et al. 2013b), by incorporating *Gaia*-DR2 stellar radius estimates (reported in Berger et al. 2018) and updating the parameters (e.g., flare energy, spot size).

- (i) More than 40% of the original solar-type superflare stars in our previous studies are now classified as subgiant stars (Figure 5).
- (ii) The bolometric energy released by flares (E_{flare}) is not inconsistent with the magnetic energy (E_{mag}) stored around the large starspots (Figures 6(b) & 11).
- (iii) Our previous studies suggested that the maximum superflare energy in a given rotation period bin does not have a clear correlation with the rotation period, and superflares up to 10^{35} erg could occur on slowly-rotating solar-type stars (Figure 12(a)). This study suggests that the maximum superflare energy continuously decreases as the rotation period increases (as the star becomes older) (Figures 12(b) & 13). Superflares with energies $\lesssim 5 \times 10^{34}$ erg occur on old, slowly-rotating Sun-like stars ($T_{\text{eff}} = 5600 - 6000$ K, $P_{\text{rot}} \sim 25$ days, and age $t \sim 4.6$ Gyr)

approximately once every 2000–3000 years (Figures 13(b) & 17). In contrast, superflares up to $\sim 10^{36}$ erg can occur on young rapidly-rotating stars ($P_{\text{rot}} \sim$ a few days and $t \sim$ a few hundreds Myr) (Figure 13), and the flare frequency of such young rapidly-rotating stars is ~ 100 times higher compared with the above old slowly-rotating Sun-like stars (Figures 14 & 16).

- (iv) The maximum area of starspots does not depend on the rotation period and are roughly constant or very gentle decreasing trend around $A_{\text{spot}} = 5 \times 10^{-2} - 1 \times 10^{-1} A_{1/2\odot}$ ($A_{1/2\odot} \sim 3 \times 10^{22}$ cm 2 : solar hemisphere) when the star is young and rapidly-rotating. However, as the star becomes older and its rotation slows down, it starts to have a steep decreasing trend at a certain point : $P_{\text{rot}} \sim 12$ days ($t \sim 1.4$ Gyr) for the stars with $T_{\text{eff}} = 5600 - 6000$ K (Figure 15(b)), and $P_{\text{rot}} \sim 14$ days for the stars with $T_{\text{eff}} = 5100 - 5600$ K (Figure 15(a)). Maximum size of starspots on slowly-rotating Sun-like stars is $\sim 1\%$ of the solar hemisphere, and this is enough for generating superflares with the energy $\lesssim 5 \times 10^{34}$ erg described in (iii).
- (v) These decreasing trends of the maximum flare energy (in (iii)) and the maximum starspot area (in (iv)) can be related with each other since the superflare energy can be explained by the starspot magnetic energy as in (ii). However, there is also a difference between the two: the maximum area of starspots starts to steeply decrease at a certain P_{rot} value (as in (iv)), while the maximum flare energy continuously decrease as the rotation slows down (as in (iii)). This can suggest a possibility that the flare energy is determined not only by the starspot area but also by other important factors (e.g., spot magnetic structure).
- (vi) The size distribution of starspots on Sun-like stars ($T_{\text{eff}} = 5600 - 6000$ K and $P_{\text{rot}} \sim 25$ days) between $A_{\text{spot}} = 10^{-2.5} - 10^{-1.0} A_{1/2\odot}$ roughly locate on the extension line of the distribution of sunspot groups between $A_{\text{spot}} = 10^{-3.25} - 10^{-2.5} A_{1/2\odot}$ (Figure 18). The upper limit of starspot size values on slowly-rotating Sun-like stars would be \sim a few $\times 10^{-2} A_{1/2\odot}$ and the appearance frequency of these spots is approximately once every 2000–3000 years.

6.3. Future prospects

In this paper, we have reported the current updates of our series of studies on superflares on solar-type stars. However, we need more studies to clarify the properties of superflare stars on Sun-like stars and answer the important question “Can our Sun have superflares ?”. For example, our spectroscopic observations so far have observed 64 solar-type superflare stars, but the number of Sun-like superflare stars ($T_{\text{eff}} = 5600 - 6000$ K, $P_{\text{rot}} \sim 25$ days, and $t \sim 4.6$ Gyr) that have been investigated spectroscopically and found to be “single” stars are now only a few (~ 1). In the figures in Section 5, the number of old slowly-rotating Sun-like superflare stars are now very small, and the current statistical discussions are not enough. In this study, as for superflares found from *Kepler* 30-min cadence data, we only used the data originally found as solar-type superflare stars from *Kepler* data of the first ~ 500 days (Quarter 0 – 6) in our previous study (Shibayama et al. 2013; Candelaresi et al. 2014). In our next study, we plan to increase the number of data by using the whole *Kepler* dataset of ~ 1500 days (Quarter 0 – 17)¹⁶. Moreover, the data from the next missions such as *TESS* (Ricker et al. 2015) and *PLATO* (Rauer et al. 2014) are expected to bring us more superflare data

¹⁶ We note that Davenport (2016) conducted the flare survey of F–M type stars using the whole *Kepler* 30-min cadence dataset, but their data are not necessarily enough for investigating flare stars with smaller frequency (e.g., slowly-rotating Sun-like stars).

on solar-type stars in near future. These two missions are helpful also for spectroscopic follow-up observations of superflare stars since these two missions observe more nearby stars (with their wider spatial coverage), compared with *Kepler*.

In addition to the statistical properties of superflares that we discussed in this paper, there are so many topics that should be investigated in near future to fully understand the physics of superflares and their effects in the related research fields. For example, mechanisms of white-light continuum emissions of superflares (e.g., Kowalski & Allred 2018; Heinzel & Shibata 2018; Namekata et al. 2017), chromospheric line profiles during superflares (e.g., Houdebine et al. 1993; Hawley et al. 2007; Honda et al. 2018), stellar mass ejections (e.g., CMEs) during superflares (e.g., Aarnio et al. 2012; Leitzinger et al. 2014; Hudson 2015; Osten & Wolk 2015; Takahashi et al. 2016; Harra et al. 2016; Vida et al. 2016; Moschou et al. 2017; Crosley & Osten 2018), the impacts of superflares on planets (e.g., Segura et al. 2010; Airapetian et al. 2016; Atri 2017; Lingam & Loeb 2017; Riley et al. 2018), detailed comparisons with a history of solar activity over \sim 1000 years (e.g., Miyake et al. 2012&2013; Hayakawa et al. 2017a&2017b; Usoskin 2017), quasi-periodic pulsations (QPPs) of the brightness during superflares (e.g., Pugh et al. 2016; McLaughlin et al. 2018), complexities of superflare-generating starspots (e.g., Maehara et al. 2017; Toriumi et al. 2017), how starspots are distributed on the surface of superflare stars (e.g., Doyle et al. 2018; Roettenbacher & Vida 2018), how starspots and plages are co-located in the case of active stars (e.g., Morris et al. 2018), and lifetimes and formation/decay processes of large starspots in solar-type stars (e.g., Shibata et al. 2013; Giles et al. 2017; Namekata et al. 2019). The superflare stars newly found from the above new missions (*TESS* and *PLATO*) would be helpful for the detailed observations to investigate these topics (e.g., spectroscopic or multi-wavelength observations of superflares themselves, and long-term changes of stellar activities).

This study is based on observations obtained with the Apache Point Observatory (APO) 3.5 m telescope, which is owned and operated by the Astrophysical Research Consortium. We used observation time allocated to University of Washington. We are grateful to APO 3.5m Observing Specialists (Candace Gray, Jack Dembicky, Russet McMillan, and Theodore Rudyk) and other staffs of Apache Point Observatory and University of Washington for their large contributions in carrying our observations. George Wallerstein and Charli Sakari kindly shared their observation time to take our data on 2017 October 15 (UT) as a time exchange. We acknowledge with great thanks that Brett Morris helped us when the corresponding author Y.N. learned how to make observations at APO and how to analyze APO data. Thanks are also to Adam Kowalski and Petr Heinzel for general discussions. We are indebted to Yoichi Takeda for providing us the TGVIT and SPTOOL programs developed by him.

This paper includes data collected by the *Kepler* mission. Funding for the *Kepler* mission is provided by the NASA Science Mission Directorate. The *Kepler* data presented in this paper were obtained from the Multimission Archive at STScI. This paper also has made use of data from the European Space Agency (ESA) mission *Gaia* (<https://www.cosmos.esa.int/gaia>), processed by the *Gaia* Data Processing and Analysis Consortium (DPAC, <https://www.cosmos.esa.int/web/gaia/dpac/consortium>). Funding for the DPAC has been provided by national institutions, in particular the institutions participating in the *Gaia* Multilateral Agreement.

This work originally started from the discussions during “Superflare Workshop 2016 at Kyoto University: Superflares on Solar-type Stars and Solar Flares, and Their Impacts on Exoplanets and the Earth” supported by the International Research Unit of Advanced Future Studies of Kyoto University. This work was also supported by JSPS KAKENHI Grant Numbers JP16J00320, JP16J06887, JP16H03955, JP17H02865, JP17K05400, and JP18J20048.

Facilities: APO/ARC3.5m(ARCES), Kepler, Gaia.

APPENDIX

A. DETAILS OF ANALYSES AND RESULTS OF THE APO3.5M SPECTROSCOPIC OBSERVATIONS

A.1. *Binarity*

For the first step of our analyses, we checked the binarity of each superflare star, as we did in [Notsu et al. \(2015a\)](#). First, we checked slit viewer images of APO3.5m telescope. Two stars (KIC11551430 and KIC7093428) have visual companion stars, as shown in Figures 19 (a) and 20 (a).

As for KIC11551430, we took spectra of both components (the brighter primary star: KIC11551430A and the fainter companion star KIC11551430B) of the visual binary system separately, as shown in Figures 19 (b) and (c). We checked again pixel count data of superflare events on KIC11551430 (Figures 19 (d) and (e)), which are originally in [Maehara et al. \(2015\)](#), and confirmed that the center positions of the brightness during superflare events are roughly the same as those during quiescent state. This is consistent with the possibility that superflares occur on the primary star KIC11551430A (cf. Figures S1 & S2 of [Maehara et al. 2012](#)).

As for KIC7093428, we can see one primary brighter star (KIC7093428A) and two fainter companion stars (KIC7093428B and KIC7093428C) in Figure 20 (a). We only took spectra of the main brighter star (KIC7093428A) as shown in Figure 20 (b), since companions stars (B & C) are too faint. We also checked again pixel count data of superflare events on KIC7093428 (Figures 20 (c) and (d)), which are originally in [Maehara et al. \(2015\)](#). We can see that the center positions of the brightness during superflare events are shifted compared with those during quiescent state. This suggests the high possibility that superflares occur on the fainter companion stars KIC7093428B or KIC7093428C (cf. Figures S1 & S2 of [Maehara et al. 2012](#)), not on the primary G-type star KIC7093428A. Then KIC7093428 has “VB” in the second column of Table 1.

As described in Section 2, we selected 23 target stars and took spectra of 22 stars except for the too faint target star KIC10745663 ($K_p=14.3$ mag). Among the 22 observed stars, the data quality of our spectroscopic data of the fainter four stars (KIC6032920, KIC10528093, KIC10646889, and KIC9655134) are not enough for the detailed following discussions. We plot examples of photospheric lines in Figure 21 for reference. We only remark here that they does not show any clear signs of binarity, on the basis of Figure 21 and the slit viewer images of APO3.5m telescope. In the following discussions of this paper, we only treat the 18 target stars that we got spectra of with enough S/N.

Next we investigated the line profiles, and found two stars (KIC11128041 and KIC10338279) show double-lined profiles. In this process, we checked by eye the profiles of the many spectral lines, and the double-lined spectra of these two stars are shown in Figure 22. Since these double-lined profiles are caused by the overlap of the radiation of multiple stars, we regard these two stars as double-lined spectroscopic binary stars. These two stars have “SB2” in the second column of Table 1.

Third, we investigated time variations of the line profiles between the multiple observations that are expected to be caused by the orbital motion in the binary system. This investigation was for the target stars that we observed multiple times (16 stars). In Section 2, we already measured the radial velocity (RV) of all the target stars that were not classified as visual binary stars or double-lined spectroscopic binary stars, and these values are listed in Table 2. We have also conducted spectroscopic observations of these four stars (KIC4742436, KIC4831454, KIC9652680, and KIC11610797) using Subaru telescope ([Notsu et al. 2015a&2015b; Honda et al. 2015](#)), and we also use these data in

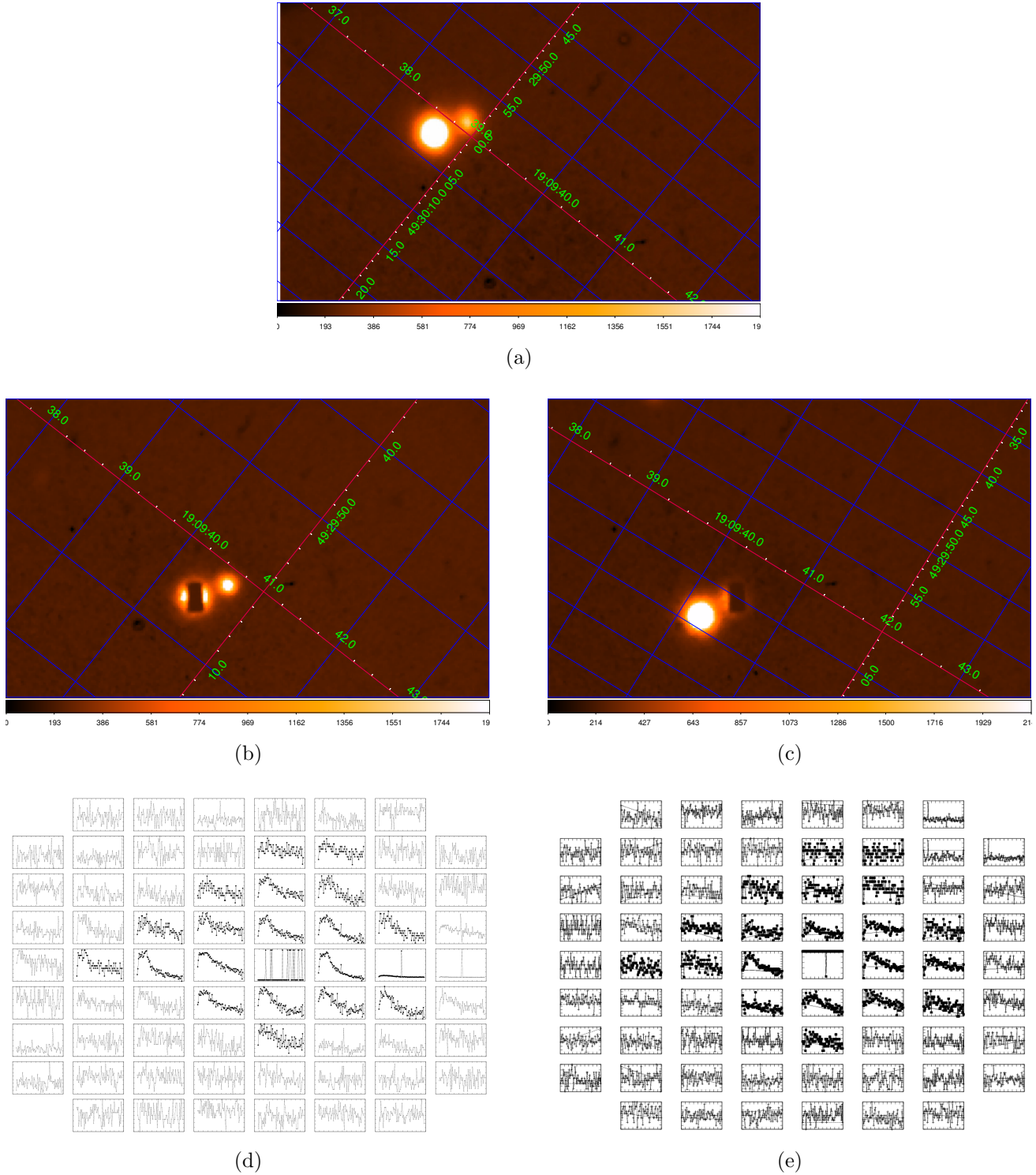


Figure 19. (a)(b)(c) Slit viewer images of the visual binary target KIC11551430. These images show that this star (the brighter primary star KIC11551430A, which we took spectroscopic data as in (b)) has a visual fainter companion star (KIC11551430B, which we took spectroscopic data as in (c)).
 (d)(e) Pixel count data around two typical superflares on KIC11551430 from the data of [Maebara et al. \(2015\)](#). The peak time (BJD (Barycentric Julian Date) - 2,400,000) of flares in (d) & (e) are 55019.673718 and 56196.445193, and the estimated bolometric energy of them are 2.2×10^{35} erg and 2.8×10^{34} erg, respectively. The pixels in the center of the flares are saturated.

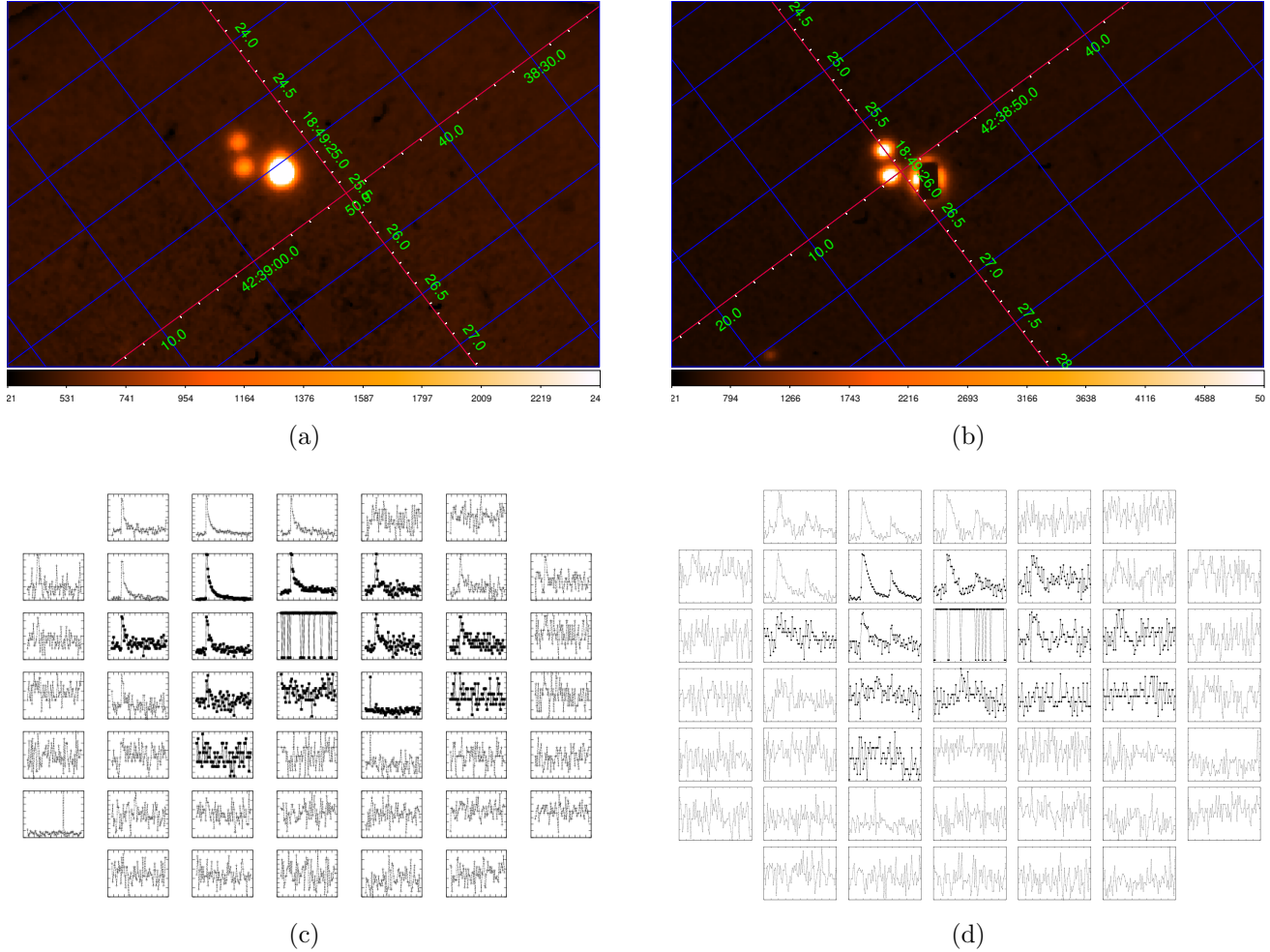


Figure 20. (a)(b) Slit viewer images of the visual binary target KIC7093428. These images show that this star (the brighter primary star KIC7093428A, which we took spectroscopic data as in (b)) has two fainter visual companion stars (KIC7093428B and KIC7093428C).

(c)(d) Pixel count data around two typical superflares on KIC7093428 from the data of Maehara et al. (2015). The peak time (BJD - 2,400,000) of flares in (c) & (d) are 55102.453431 and 55104.090097, and the estimated bolometric energy of them are 4.0×10^{34} erg and 1.1×10^{34} erg, respectively. The pixels in the center of the flares are saturated.

the RV investigation here (They are also listed in Table 2). As a result, KIC11551430A, KIC4543412, and KIC11128041 show RV changes as shown in Figure 22, and these RV changes are larger enough compared with RV errors of APO data ($\lesssim 1 \text{ km s}^{-1}$). We confirmed this typical RV error value ($\lesssim 1 \text{ km s}^{-1}$) by comparing our spectroscopic data of the single comparison stars that we observed multiple times in this study and are listed in Table 3. These three stars have “RV” in the second column of Table 1.

In total, we regard 5 superflare stars as binary stars among the 18 target stars of which we got spectra with enough S/N. The remaining 13 superflare stars does not show any evidence of binarity within the limits of our analyses, so we treat them as “single stars” in this paper. They have “no” in the second column of Tables 1. Spectra of photospheric lines, including Fe I 6212, 6215, 6216, and 6219Å lines, of the 13 “single” superflare stars are shown in Figure 23. We observed 9 stars among

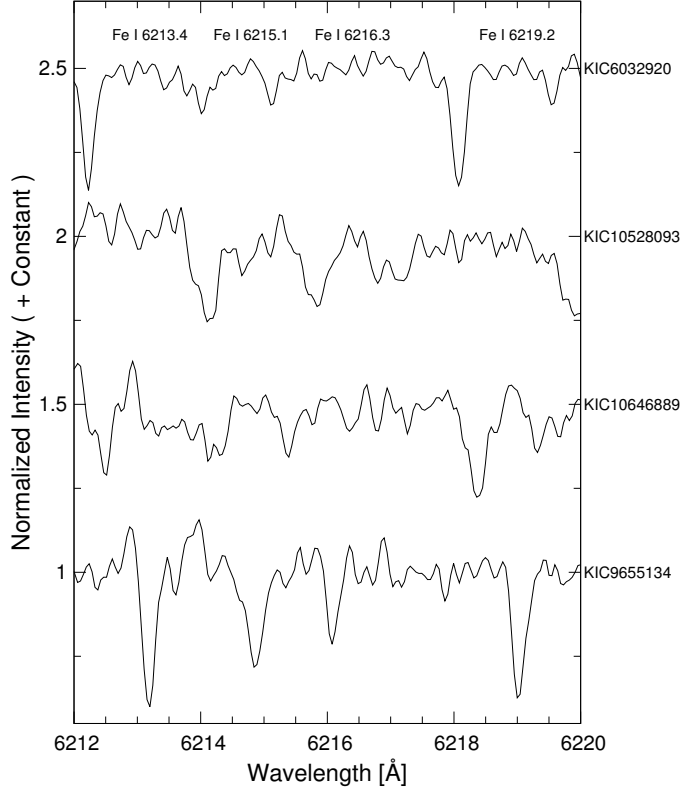


Figure 21. Example of photospheric absorption lines, including Fe I 6213, 6215, 6216, and 6219 \AA lines, of the fainter four superflare stars (KIC6032920, KIC10528093, KIC10646889, and KIC9655134). The wavelength scale is adjusted to the heliocentric frame.

the 13 “single” stars multiple times, and we made co-added spectra of these 9 stars by conducting the following two steps. First, we shifted the wavelength value of each spectrum to the laboratory frame on the basis of the radial velocity value of each observation listed in Table 2. Next, we added up these shifted spectra to one co-added spectrum. The co-added spectra are mentioned as “comb” in Table 2, and only co-added spectra of these 9 stars are used in Figure 23. Only the co-added spectra are used for the detailed analyses in the following sections of this paper, when we analyze the spectral data of the 9 stars that we observed multiple times.

In addition to these 9 “single” stars, we also made co-added spectra with the same methods for the two binary target stars (KIC11551430A and KIC4543412) that show radial velocity shifts but do not show double-lined profiles. They are also shown in Figure 23. For reference, we also use these data when we estimate stellar parameters in the following.

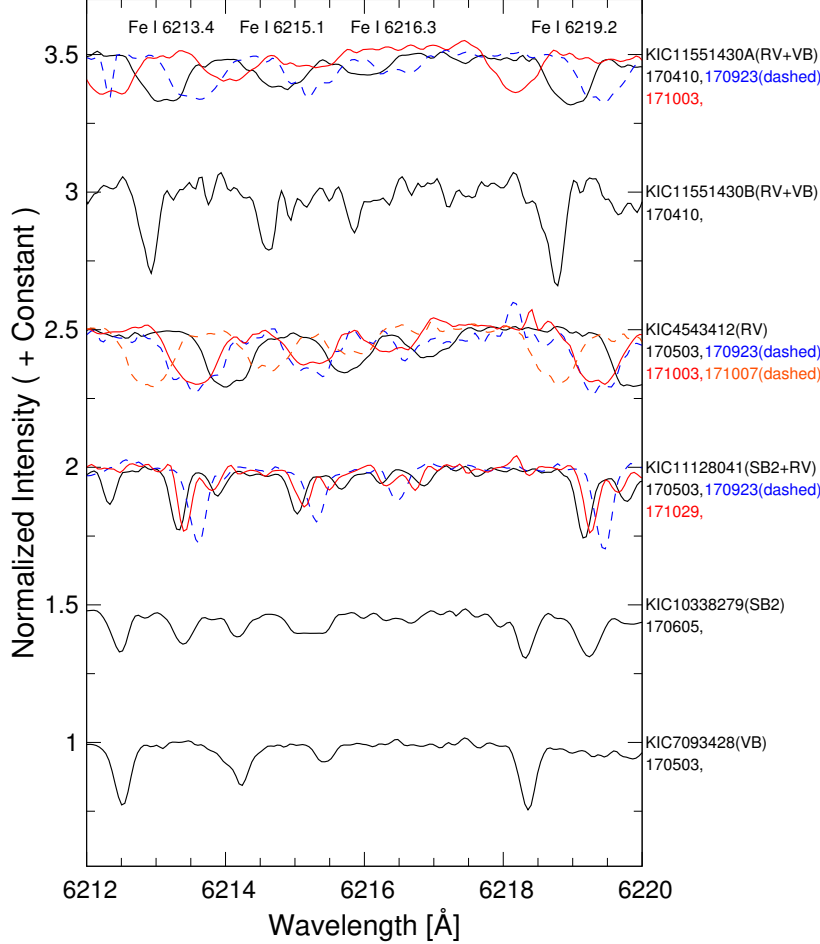


Figure 22. Example of photospheric absorption lines, including Fe I 6213, 6215, 6216, and 6219 \AA lines, of superflare stars that we consider as spectroscopic binary stars. The wavelength scale is adjusted to the heliocentric frame. Numbers below each stars name show observation dates (cf. Table 2).

A.2. Temperature, surface gravity, and metallicity

We estimated the effective temperature T_{eff} , surface gravity $\log g$, microturbulence v_t , and metallicity [Fe/H] of the target superflare stars, by using the method that is basically the same as the one we have used in Notsu et al. (2015a & 2017). We measured the equivalent widths of ~ 200 Fe I and Fe II lines, and used TGVIT program developed by Y. Takeda (Takeda et al. 2002 & 2005). For reference, Rich et al. (2017) also applied this method to their ARCES spectroscopic data, which were taken with the same wavelength resolution value ($R \sim 32,000$) as our data, and they confirmed the resultant values are consistent with the other previous studies. The resultant atmospheric parameters (T_{eff} , $\log g$, v_t , and [Fe/H]) are listed in Table 4.

We then compare these resultant atmospheric parameters with the values reported in the Data Release 25 *Kepler* Stellar Properties Catalog (DR25-KSPC: Mathur et al. 2017). We show the results in Figure 24, where the data points are classified with colors on the basis of the methods used to derive the parameters in DR25-KSPC. Our values seem to be in good agreement with the

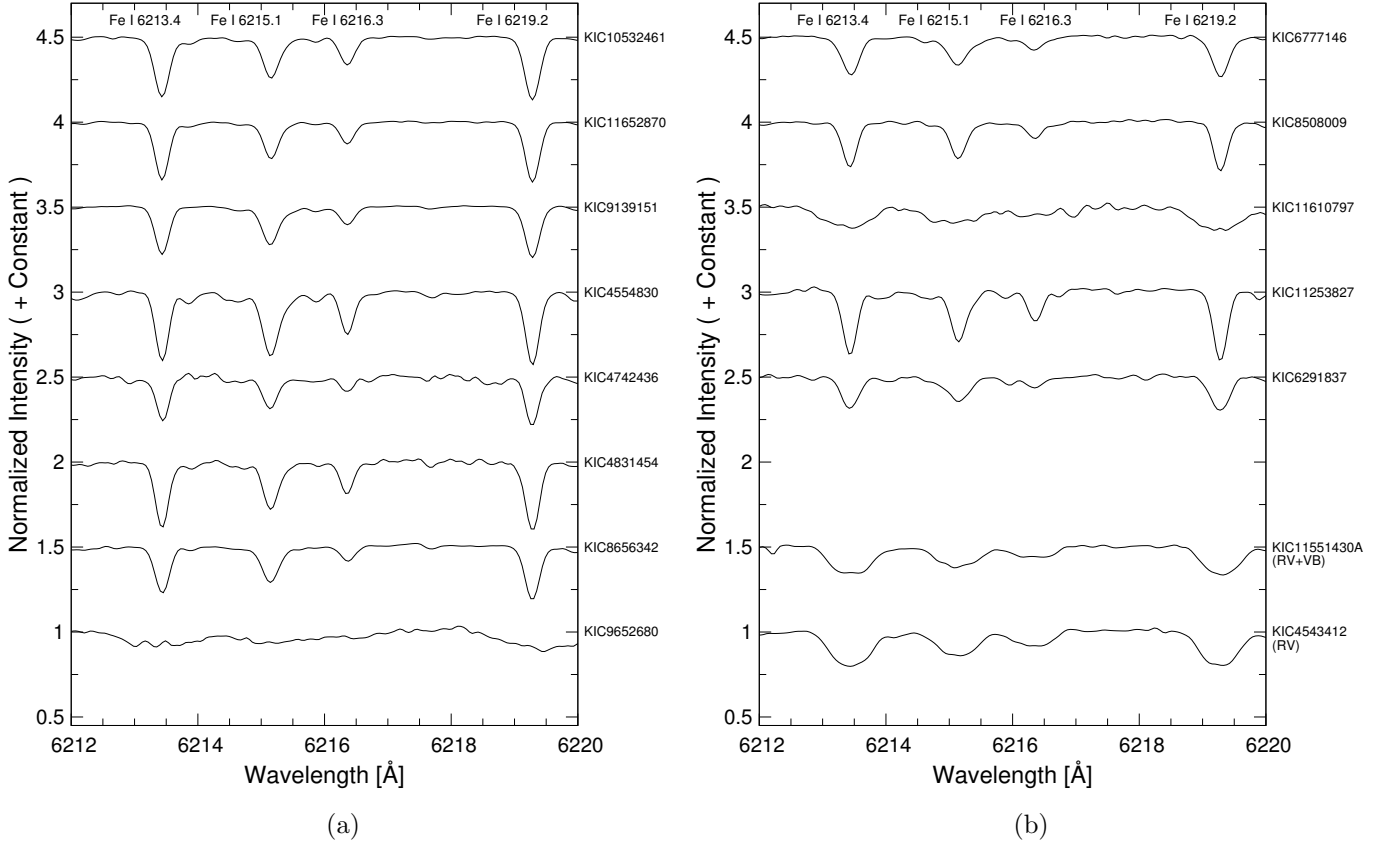


Figure 23. Example of photospheric absorption lines, including Fe I 6213, 6215, 6216, and 6219 Å lines. The wavelength scale of each spectrum is adjusted to the laboratory frame. In (a) and the upper part of (b), 13 “single” superflare stars that show no evidence of binarity are plotted. Co-added spectra are used here in case that the star was observed multiple times (See Table 2). In the bottom of (b), the co-added spectra of the two binary stars KIC11551430A and KIC4543412, which only show radial velocity shifts but do not show any double-lined profiles, are also plotted for reference.

DR25-KSPC values, especially for T_{eff} (Figure 24(a)). $\log g$ has some dispersion (Figure 24(b)), but this small dispersion does not cause essential problems when we consider whether the target stars are main-sequence stars or not. As for [Fe/H], if we only consider the spectroscopic values in DR25-KSPC (“DR25-SPE” in Figure 24(c)), the both values have better agreement and the difference does not affect on the overall discussions (e.g., whether the target stars are “metal-rich/poor” or not). Through this, we can remark that our spectroscopically derived values are good sources with which to discuss the actual properties of stars, as also mentioned for our previous Subaru spectroscopic data in Section 4.3 of Notsu et al. (2015a).

A.3. Stellar radius

As already listed in Table 1, we have stellar radius values R_{Gaia} of *Kepler* stars deduced from *Gaia*-DR2 parallax values (Berger et al. 2018). These values are listed again in Table 4, but five stars among our observed 18 target stars have no R_{Gaia} values reported in Berger et al. (2018).

In Figure 25 we compare these R_{Gaia} values with $\log g$ values estimated from our spectroscopic studies (Notsu et al. 2015a and this study). These two values are roughly correlated, and R_{Gaia}

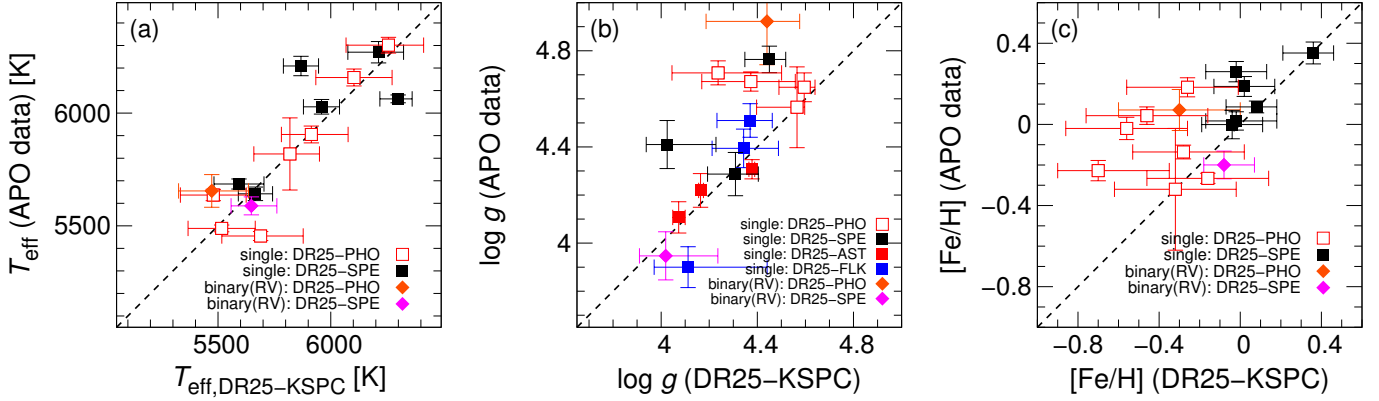


Figure 24. Comparison between the atmospheric parameters (T_{eff} , $\log g$, and $[\text{Fe}/\text{H}]$) that we estimated in this study, and those reported in the Data Release 25 *Kepler* Stellar Properties Catalog (DR25-KSPC: Mathur et al. 2017), respectively. The square points are the target superflare stars classified as single stars in Appendix A.1, while the diamond points correspond to the spectra of binary superflare stars that do not show any double-lined profiles (KIC11551430A and KIC4543412). Colors show the methods used to derive the atmospheric parameters in DR25-KSPC (PHO: photometry, SPE: Spectroscopy, FLK: flicker method (cf. Bastien et al. 2016), AST: Asteroseismology). See Mathur et al. (2017) for the details of this classification.

values look more sensitive to the boundary region between main-sequence stars and subgiants (around $\log g = 4.0 - 4.5$ and $R_{\text{Gaia}} = 1.5 - 2.0 R_{\odot}$). Then in Section 5, we mainly use these stellar radius R_{Gaia} values to strictly define main-sequence stars.

We also estimated stellar radius (R_{spec}) values from the stellar atmospheric parameters (T_{eff} , $\log g$, and $[\text{Fe}/\text{H}]$), by applying the latest PARSEC isochrones (Bressan et al. 2012; Marigo et al. 2017)¹⁷. In this process, we used basically the same method as the one used in our previous study (Notsu et al. 2015a). We selected all the data points that had possible sets of T_{eff} , $\log g$, and $[\text{Fe}/\text{H}]$ from the PARSEC isochrones, taking into account the error values of T_{eff} and $\log g$ (ΔT_{eff} and $\Delta \log g$). For the six stars that have no suitable isochrones within their original error range of T_{eff} and $\log g$ values, we then took into account larger error values as mentioned in footnote c of Table 4. We note that the resultant values of these six stars can have relatively low accuracy. We then selected the maximum and minimum R_{spec} value of each star, and determined the resultant R_{spec} value as a median of the maximum and minimum values. The error values of R_{spec} listed in Table 4 are $\lesssim 20\%$ for most of the stars, as also mentioned in Notsu et al. (2015a).

In the following, we use R_{Gaia} values as a first priority, and we use R_{spec} values only for the stars without R_{Gaia} values.

A.4. Projected rotation velocity ($v \sin i$)

We measured $v \sin i$ (stellar projected rotational velocity) of the target stars by using the method that is basically the same as that in our previous studies (Notsu et al. 2015a & 2017). This is originally based on the one described in Takeda et al. (2008). We took into account the effects of macroturbulence and instrumental broadening by considering a simple relationship among the

¹⁷ <http://stev.oapd.inaf.it/cgi-bin/cmd>

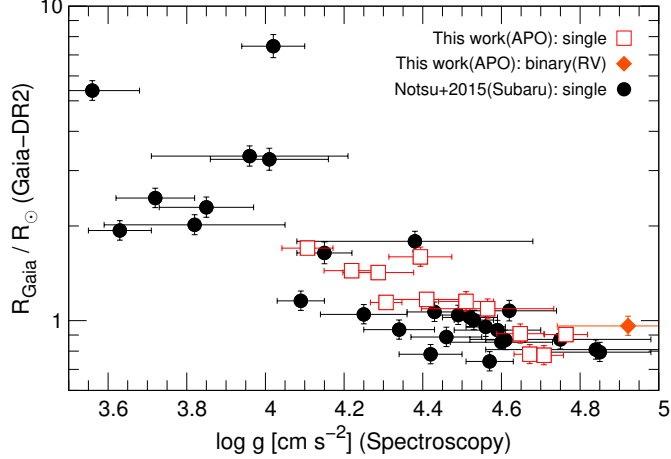


Figure 25. Stellar radius values R_{Gaia} from *Gaia*-DR2 parallaxes (Berger et al. 2018) as a function of $\log g$ estimated from our spectroscopic observations. Only the stars that have R_{Gaia} are included in this figure. The red open square points are the target superflare stars classified as single stars in Appendix A.1, and the orange diamonds correspond to the spectra of binary superflare stars that do not show any double-lined profiles (KIC4543412). The single superflare stars that we investigated using Subaru telescope (Notsu et al. 2015a & 2015b), excluding the four stars also investigated in this study (See footnote f of Table 1), are plotted with black circles.

line-broadening parameters (cf. Takeda et al. 2008), which can be expressed as

$$v_M^2 = v_{\text{ip}}^2 + v_{\text{rt}}^2 + v_{\text{mt}}^2 . \quad (\text{A1})$$

Here, v_M is the e-folding width of the Gaussian macrobroadening function $f(v) \propto \exp[-(v/v_M)^2]$, including instrumental broadening (v_{ip}), rotation (v_{rt}), and macroturbulence (v_{mt}). We derived v_M by applying an automatic spectrum-fitting technique (Takeda 1995), assuming the model atmosphere corresponding to the atmospheric parameters estimated in Appendix A.2. In this process, we used the MPFIT program contained in the SPTOOL software package developed by Y.Takeda. We applied this fitting technique to the 6212–6220Å region (shown in Figures 22 & 23) to derive $v \sin i$ values. This region has also been used in our previous studies (Notsu et al. 2015a & 2017).

The instrumental broadening velocity v_{ip} was calculated using the following equation (Takeda et al. 2008):

$$v_{\text{ip}} = \frac{3 \times 10^5}{2R\sqrt{\ln 2}} , \quad (\text{A2})$$

where $R (= \lambda/\Delta\lambda)$ is the wavelength resolution of the observation. For estimating the R value adopted here, we conducted Gaussian-fitting to emission lines in the 6180–6240Å region of the Th-Ar spectrum data. This region is around the 6212–6220Å region, where we conduct the above fitting process. We finally got $R=32,500$ and we applied this to Equation (A2) in the following. The macroturbulence velocity v_{rt} was estimated by using the relation $v_{\text{mt}} \sim 0.42\xi_{\text{RT}}$ (Takeda et al. 2008). The term ξ_{RT} is the radial-tangential macroturbulence, and ξ_{RT} was estimated using the relation reported in Valenti

& Fischer (2005):

$$\xi_{\text{RT}} = \left(3.98 - \frac{T_{\text{eff}} - 5770\text{K}}{650\text{K}} \right) . \quad (\text{A3})$$

As we described in Notsu et al. (2015a), the choice of macroturbulence equation is often important, but we only use this Equation (A3) to estimate the resultant values of this study, as we have also done in our previous studies (Notsu et al. 2015a & 2017). v_{rt} was then derived with the above equations, and we finally got $v \sin i$ with the relation $v_{\text{rt}} \sim 0.94 v \sin i$ (Gray 2005). The resultant $v \sin i$ values of the target superflare stars are listed in Table 4. As error values of $v \sin i$, we consider the systematic uncertainty with changing ξ_{RT} up to $\pm 25\%$, as described in Hirano et al. (2012).

The above estimation method of $v \sin i$ has been developed to be suitable for the Subaru/HDS spectroscopic data with the high spectral resolutions of $R \sim 55,000 - 100,000$ (Hirano et al. 2012; Notsu et al. 2013a; Notsu et al. 2015a). It is not so appropriate that we apply this method without any modifications into our APO3.5m/ARCES spectroscopic data (the spectral resolution of only $\sim 32,500$). It is difficult to estimate $v \sin i$ values as low as $2-3 \text{ km s}^{-1}$ only with APO spectra. On the other hand, in this study, we do not need to estimate $v \sin i$ values with the high precision of $2-3 \text{ km s}^{-1}$ for the overall discussions in this study with Figures 2 and 9 (e.g., whether $v \sin i \lesssim v_{\text{lc}}$ is roughly achieved, and whether the target stars can have low inclination angle values or not). There are twice (or more) differences of the spectral resolution values between this APO observation and the previous Subaru/HDS observations (Hirano et al. 2012; Notsu et al. 2013a; Notsu et al. 2015a), and the instrumental velocity v_{ip} has twice (or more) larger values between them. Then in this study (e.g., Table 4), we only report a rough upper limit value “ $v \sin i < 4 \text{ km s}^{-1}$ ” for the slowly-rotating stars with $v \sin i < 4 \text{ km s}^{-1}$. We also need to use the $v \sin i$ values of mildly slowly-rotating stars ($v \sin i \sim 5 \text{ km s}^{-1}$) with cautions.

A.5. Measurements of stellar activity indicators Ca II 8542Å and Hα 6563Å

The observed spectra of the target superflare stars around Ca II 8542Å and Hα 6563Å are shown in Figures 26 and 27, respectively. We measured the $r_0(8542)$ and $r_0(\text{H}\alpha)$ indexes, which are the residual core fluxes normalized by the continuum level at the line cores of Ca II 8542Å and Hα 6563Å, respectively. As we have already introduced in Notsu et al. (2013a), these indexes are known to be indicators of stellar chromospheric activity (e.g., Linsky et al. 1979b; Takeda et al. 2010). As the chromospheric activity is enhanced, the intensity of these indicators becomes large since a greater amount of emission from the chromosphere fills in the core of the lines. The values of the $r_0(8542)$ and $r_0(\text{H}\alpha)$ indexes of the target superflare stars are listed in Table 5. For reference, $r_0(8542)$ values of the 28 comparison stars are also listed in Table 3.

A.6. Measurements of Ca II H&K S-index

The observed spectra of the target superflare stars around Ca II H 3968Å and Ca II K 3934Å lines are shown in Figure 28. As described in Section 2, these spectra are normalized by using spectra of early-type standard stars, as also done in Morris et al. (2017). The emission in the cores of the Ca II H & K lines is a widely-known indicator of the stellar chromospheric activity (e.g., Hall 2008 for review), and this is more sensitive to activity level changes compared with Ca II 8542Å line (cf. Takeda et al. 2010 & 2012). Ca II H & K emission is often measured as “S-index”, which is the flux in the emission features normalized by two pseudocontinuum regions on either side of the absorption features (e.g., Vaughan et al. 1978; Duncan et al. 1991; Isaacson & Fischer 2010; Mittag et al. 2013;

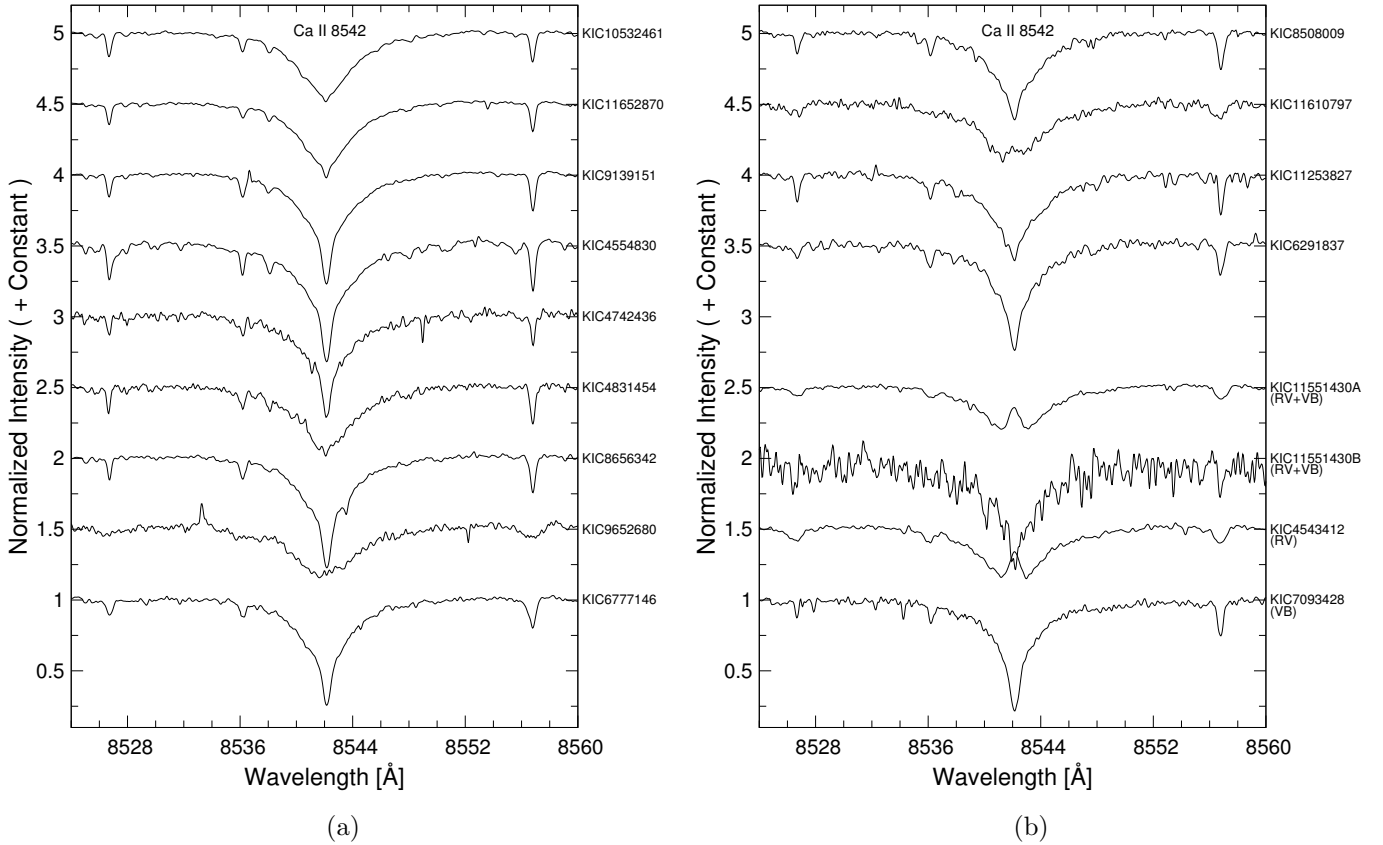


Figure 26. Spectra around Ca II 8542 Å line. The wavelength scale of each spectrum is adjusted to the laboratory frame. In (a) and the upper part of (b), 13 “single” superflare stars that show no evidence of binarity are plotted. Co-added spectra are used here in case that the star was observed multiple times (See Table 2). In the bottom of (b), the spectra of binary stars that do not show any double-lined profiles are plotted for reference. As for KIC11551430A and KIC4543412 among them, which only show radial velocity shifts, the co-added spectra are used.

Karoff et al. 2016; Morris et al. 2017). We measured the S -index values of the target stars in the following of this section.

The S -index value can vary among other instruments for the same intrinsic flux, as described in Section 2.1 of Isaacson & Fischer (2010). Following the method used in Isaacson & Fischer (2010) and Morris et al. (2017), we calibrated S -index values of our APO observation data (S_{APO}) against the S -index values already calibrated to the Mount Wilson Observatory (MWO) sample (S_{MWO})¹⁸. In this calibration process, we use our observation data of the 28 bright solar-type comparison stars described in Section 2 and listed in Table 3. All of these 28 stars have S -index values calibrated to the Mount Wilson Observatory (MWO) sample (S_{MWO} values in Table 3) that are reported in Isaacson & Fischer (2010) on the basis of California Planet Search (CPS) program spectroscopic observations.

¹⁸ Morris et al. (2017) already conducted the calibration of S -index measurements for APO data, but most of their observed stars are K-type stars. Since S -index is a value also depending on stellar colors (Noyes et al. 1984), we newly conduct the calibration using solar-type (G-type main-sequence) stars in this study.

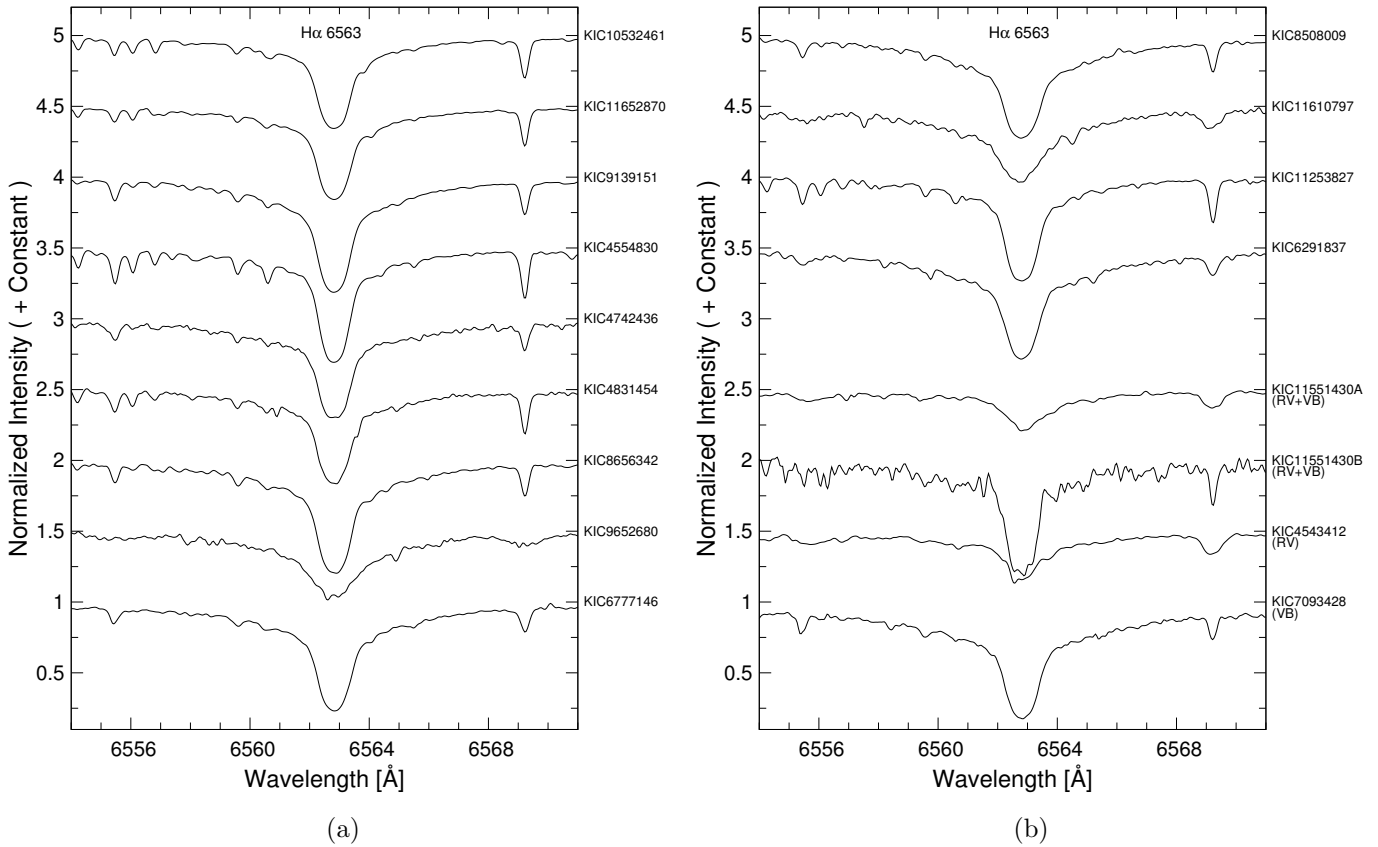


Figure 27. Spectra around H α 6563Å line. The wavelength scale of each spectrum is adjusted to the laboratory frame. In (a) and the upper part of (b), 13 “single” superflare stars that show no evidence of binarity are plotted. Co-added spectra are used here in case that the star was observed multiple times (See Table 2). In the bottom of (b), the spectra of binary stars that do not show any double-lined profiles are plotted for reference. As for KIC11551430A and KIC4543412 among them, which only show radial velocity shifts, the co-added spectra are used.

We first measured the S -index from our APO data (S_{APO}) of these comparison stars using the following equation (cf. Morris et al. 2017):

$$S_{\text{APO}} = \frac{aH + bK}{cR + dV} , \quad (\text{A4})$$

where H and K are the recorded counts in a 1.09\AA full-width at half-maximum triangular bandpasses centered on the Ca II H and K lines at 3968.469\AA and 3933.663\AA , respectively. V and R are two 20\AA wide reference bandpasses centered on 3901.07\AA and 4901.07\AA . The values of a , b , c , and d should be selected so that S_{APO} has roughly equal flux contribution from the H and K emission lines and roughly equal flux contribution from the R and V pseudocontinuum regions in the APO spectra. Here we finally had $a = b = c = d = 1$ after trial and error in this study.

Then in Figure 29, we compared these APO S-index values (S_{APO}) listed in Table 3 with the S_{MWO} values reported in Isaacson & Fischer (2010), and investigated the two constants of the following equation (cf. Morris et al. 2017):

$$S_{\text{MWO}} = C_1 S_{\text{APO}} + C_2 . \quad (\text{A5})$$

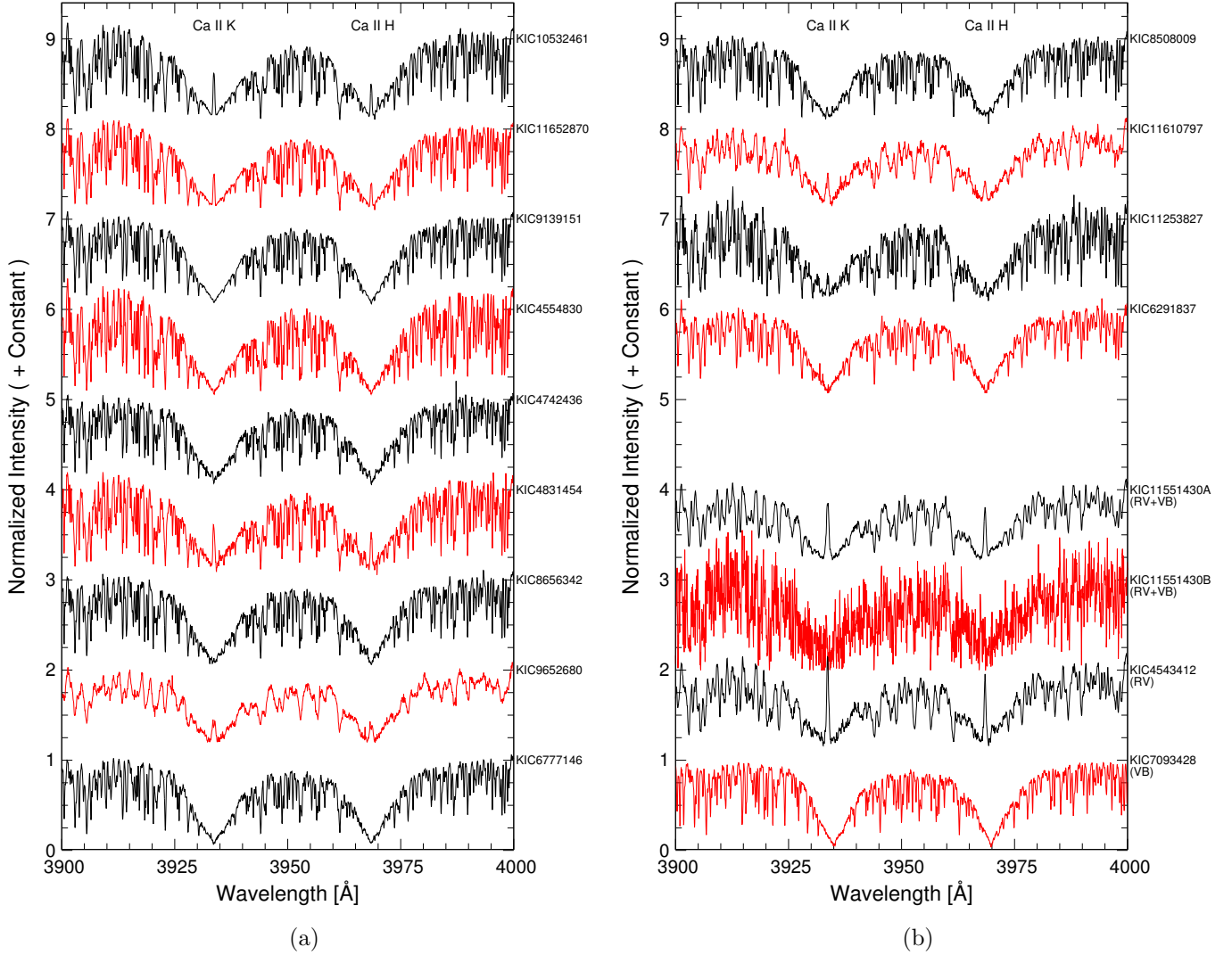


Figure 28. Spectra around Ca II H 3968Å and Ca II K 3934Å lines. The wavelength scale of each spectrum is adjusted to the laboratory frame. In (a) and the upper part of (b), 13 “single” superflare stars that show no evidence of binarity are plotted. Co-added spectra are used here in case that the star was observed multiple times (See Table 2). In the bottom of (b), the spectra of binary stars that do not show any double-lined profiles are plotted for reference. As for KIC11551430A and KIC4543412 among them, which only show radial velocity shifts, the co-added spectra are used. As for the spectra of KIC6291837 and KIC11551430B, datapoints heavily contaminated by cosmic-rays are removed to avoid confusions.

Since S -index varies over time for each star in the sample, the linear correlation between the S_{APO} and S_{MWO} can have some intrinsic spread as in Figure 29. Applying the least-square method to the data in Figure 29, finally we got $C_1 = 22.005$ and $C_2 = 0.009$. Such larger (e.g., $C_1 \sim 22$) conversion factors of S -indexes are commonly appeared in the researches using relatively high dispersion spectrograph. For example, Morris et al. (2017) using APO/ARCES data (the same instruments and same method as our study: $C_1 \sim 21.1$), Karoff et al. (2013) using NOT/FIES data ($R \sim 25,000$ and $C_1 \sim 16.6$), and Isaacson & Fischer (2010) using Keck/HIRES data ($R \sim 52,000$ and $C_1 \sim 31.5$). As described in the final paragraph of Section 3.6 of Karoff et al. (2013), the relatively large C_1 value in our study can be

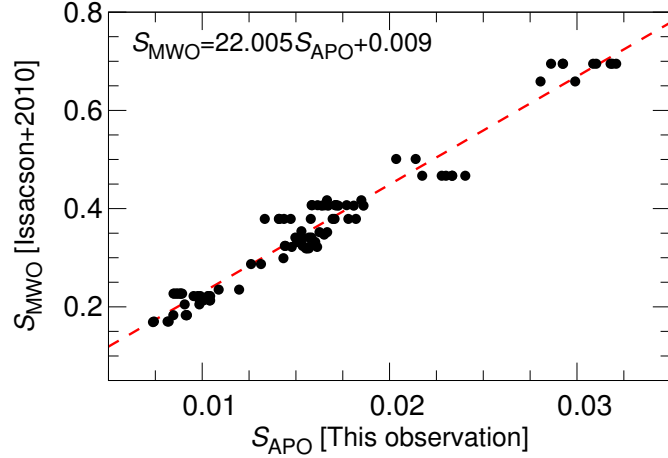


Figure 29. Calibration of S -index values measured from the APO data in this observation (S_{APO}) against the S -index values calibrated to the Mount Wilson Observatory (MWO) sample (S_{MWO}). S_{APO} values in this figure are from the spectroscopic data of multiple observations of the 28 bright solar-type comparison stars (Table 3). S_{MWO} values are the values reported in Isaacson & Fischer (2010).

mainly due to the higher spectral resolutions of APO data, compared with the original Mount Wilson observations (Duncan et al. 1991). Using Equations (A4) & (A5) and these C_1 & C_2 values, we finally estimated the calibrated S -index value of each spectrum ($S_{\text{HK}} \equiv S_{\text{MWO}}$) from each S_{APO} value. The S_{HK} values from the observations of comparison stars are listed in Table 3, and the resultant S_{HK} values of the target superflare stars from their spectral data (Figure 28) are listed in Table 5.

A.7. Measurements of Ca II H&K flux

S -index is known to be stellar temperature dependent (e.g., Noyes et al. 1984), and it is a purely empirical quantity. Then it can be advantageous to calculate chromospheric fluxes. Then in the following, we calculated Ca II H&K flux values from the S -index values with stellar colors, using the formulation described in Mittag et al. (2013). We summarize the method in the following.

The stellar surface fluxes emitted in the Ca II H&K lines (\mathcal{F}_{HK}) are expressed with S -index (S_{HK}) as:

$$\mathcal{F}_{\text{HK}} = \frac{\mathcal{F}_{\text{RV}}}{\alpha} S_{\text{HK}} , \quad (\text{A6})$$

where \mathcal{F}_{RV} is the surface flux in both continua (V and R region mentioned in Appendix A.5), and the factor α is a historical dimensionless conversion factor. Following Mittag et al. (2013), we use the value $\alpha = 19.2$. \mathcal{F}_{RV} is estimated from stellar color $B - V$ using the following empirical equation applicable to main-sequence and subgiant stars:

$$\log \left(\frac{\mathcal{F}_{\text{RV}}}{19.2} \right) = 8.25 - 1.67(B - V) . \quad (\text{A7})$$

As for the target *Kepler* superflare stars in Table 4 and the 15 comparison stars (among all the 28 comparison stars) with remarks (1) or (2) in Table 3, which were observed in Notsu et al. (2017),

$B - V$ values were calculated from T_{eff} and [Fe/H] using Equation (2) of Alonso et al. (1996). As for the remaining 13 stars, $B - V$ values reported in Table 1 of Isaacson & Fischer (2010) are used, and T_{eff} values used in the following are derived from $B - V$ values by using Equation (2) of Valenti & Fischer (2005).

We then estimated chromospheric excess flux of Ca II H&K lines (\mathcal{F}'_{HK}) by subtracting the photospheric flux contribution ($\mathcal{F}_{\text{HK,phot}}$) in the line center:

$$\mathcal{F}'_{\text{HK}} = \mathcal{F}_{\text{HK}} - \mathcal{F}_{\text{HK,phot}} . \quad (\text{A8})$$

$\mathcal{F}_{\text{HK,phot}}$ were derived from $B - V$ by using the following equations in Mittag et al. (2013):

$$\log \mathcal{R}_{\text{HK,phot}} = -4.898 + 1.918(B - V)^2 - 2.893(B - V)^3 \quad (\text{A9})$$

$$\mathcal{R}_{\text{HK,phot}} = \frac{\mathcal{F}_{\text{HK,phot}}}{\sigma T_{\text{eff}}^4} . \quad (\text{A10})$$

\mathcal{F}'_{HK} is frequently converted to the flux-related stellar activity index $\log R'_{\text{HK}}$ (Linsky et al. 1979a):

$$\mathcal{R}'_{\text{HK}} = \frac{\mathcal{F}_{\text{HK}} - \mathcal{F}_{\text{HK,phot}}}{\sigma T_{\text{eff}}^4} = \frac{\mathcal{F}'_{\text{HK}}}{\sigma T_{\text{eff}}^4} . \quad (\text{A11})$$

With this normalization, we can compare the activity level of stars with different effective temperatures and colors. The resultant values of \mathcal{F}'_{HK} and \mathcal{R}'_{HK} of the target superflare stars are listed in Table 5.

Schrijver (1987) introduced the concept of “basal flux” ($\mathcal{F}_{\text{HK,basal}}$), which is residual flux remaining in the core of the Ca II H&K lines of inactive stars after their photospheric line contribution ($\mathcal{F}_{\text{HK,phot}}$) is removed. Mittag et al. (2013) investigated \mathcal{F}'_{HK} values of very large number of main-sequence, subgiant, and giant stars, and measured the “lower” boundary of \mathcal{F}'_{HK} distribution as a function of $B - V$. Mittag et al. (2013) then reported the empirical scaling between $\mathcal{F}_{\text{HK,basal}}$ and $B - V$:

$$\log \mathcal{F}_{\text{HK,basal}} = a + b(B - V) + c(B - V)^2 , \quad (\text{A12})$$

where coefficients a , b , and c vary depending on $B - V$ and luminosity classes (V, IV, or III), and they are listed in Table 3 of Mittag et al. (2013). By subtracting this basal flux component $\mathcal{F}_{\text{HK,basal}}$ from \mathcal{F}'_{HK} , we can get new “pure” and universal activity indicators \mathcal{F}'_{HK} and $\log \mathcal{R}'_{\text{HK}}$ defined by

$$\mathcal{R}'_{\text{HK}} = \frac{\mathcal{F}'_{\text{HK}} - \mathcal{F}_{\text{HK,basal}}}{\sigma T_{\text{eff}}^4} = \frac{\mathcal{F}_{\text{HK}} - \mathcal{F}_{\text{HK,phot}} - \mathcal{F}_{\text{HK,basal}}}{\sigma T_{\text{eff}}^4} = \frac{\mathcal{F}'_{\text{HK}}}{\sigma T_{\text{eff}}^4} . \quad (\text{A13})$$

This $\log \mathcal{R}'_{\text{HK}}$ index allows comparisons of the activity levels of stars with different luminosity classes and different temperatures on the same scale (Mittag et al. 2013). The resultant values of \mathcal{F}'_{HK} and \mathcal{R}'_{HK} of the target superflare stars and the comparison stars are listed in Tables 5 and 3, respectively.

In Figures 30 (a)–(c), we compared the resultant values of the Ca II H&K indexes (S_{HK} index, $\log \mathcal{F}'_{\text{HK}}$ index, and $\log R'_{\text{HK}}$ index) with those of $r_0(8542)$ index (normalized intensity at the center of Ca II 8542Å line). As seen in these figures, Ca II 8542 index and Ca II H&K indexes have good correlations also for *Kepler* solar-type superflare stars, as expected from the previous studies (e.g., Takeda et al. 2012; Karoff et al. 2016). In particular, $\log R'_{\text{HK}}$ index (Figure 30 (c)) has the

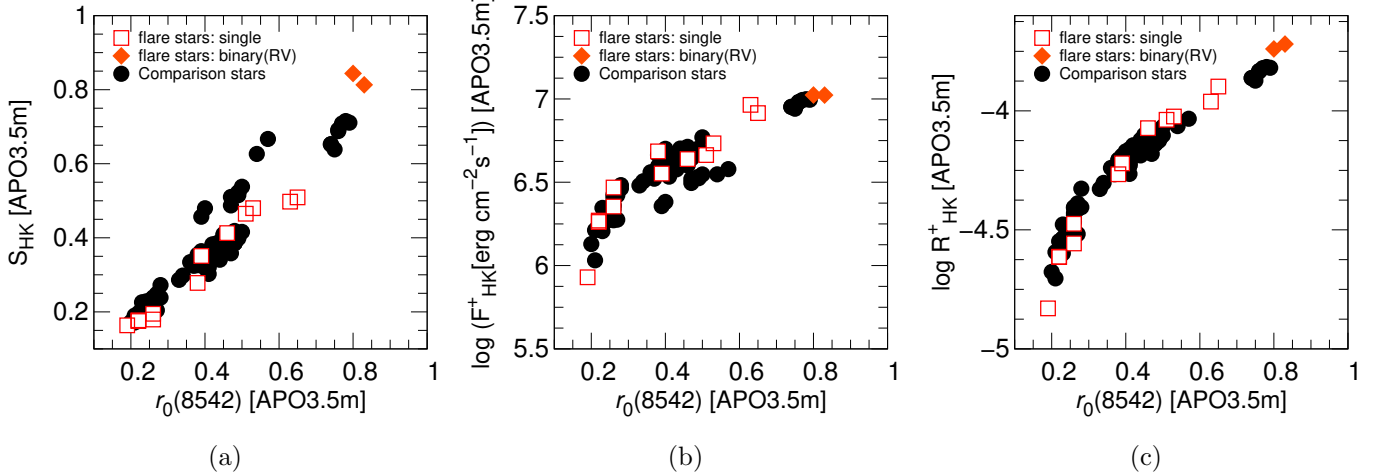


Figure 30. (a) $r_0(8542)$ vs. S_{HK} (b) $r_0(8542)$ vs. $\log F'_{\text{HK}}$ (c) $r_0(8542)$ vs. $\log R'_{\text{HK}}$

The white square points are the target superflare stars classified as single stars in Appendix A.1, and the orange diamonds correspond to the spectra of binary superflare stars that do not show any double-lined profiles (KIC11551430A and KIC4543412). Black circles show the values of comparison stars.

best correlation with Ca II 8542 index among these three Ca II H&K indexes. As for this $\log R'_{\text{HK}}$ index, stellar temperature (color) dependence and the contribution from photospheric/basal fluxes are removed (Equation (A13)). In addition, Figure 30 (c) might suggest that $\log R'_{\text{HK}}$ index is much more sensitive to the difference in the lower activity level region ($r_0(8542) \lesssim 0.3$), compared with $r_0(8542)$ index, as also suggested in Takeda et al. (2012). Then we mainly use this $\log R'_{\text{HK}}$ index when we discuss the measurement results of Ca II H&K lines in in Section 4.4.

A.8. Li abundances

The observed spectra of the target superflare stars around Li I 6708Å are shown in Figure 31. We measured the Li abundances [$A(\text{Li})$] of the stars using these spectra and the atmospheric parameters estimated in Appendix A.2. We used the automatic profile-fitting method that is basically the same as in our previous studies (Honda et al. 2015; Notsu et al. 2017). This is originally based on the method described in Takeda & Kawanomoto (2005). We summarize the method in the following.

In the process of calculating $A(\text{Li})$, we used the MPFIT program contained in the SPTOOL software package also used above. We assumed local thermodynamic equilibrium (LTE) and derived Li abundances using the synthesis spectrum with interpolated model atmospheres taken from Kucucz (1993). We also assumed ${}^6\text{Li}/{}^7\text{Li}=0$ throughout this study. The line data around the Li I 6708Å region adapted here are the same as those used in Section 2.2 of Takeda & Kawanomoto (2005). The estimated $A(\text{Li})$ values of the target stars are listed in Table 4. For the stars where Li features are absent (e.g., below the detectable limit), we estimated the upper limit values of $A(\text{Li})$ by applying the method that we described in Honda et al. (2015) and Notsu et al. (2017).

Our previous paper, Honda et al. (2015) and Notsu et al. (2017) discussed the typical errors of Li abundances by considering errors arising from multiple causes (errors linked to atmospheric parameters, uncertainties arising from profile fitting errors, and non-LTE effects). Since we conduct basically the same analyses as the above two papers, we here roughly assume that errors of $A(\text{Li})$ is ~ 0.15 dex, as in Notsu et al. (2017).

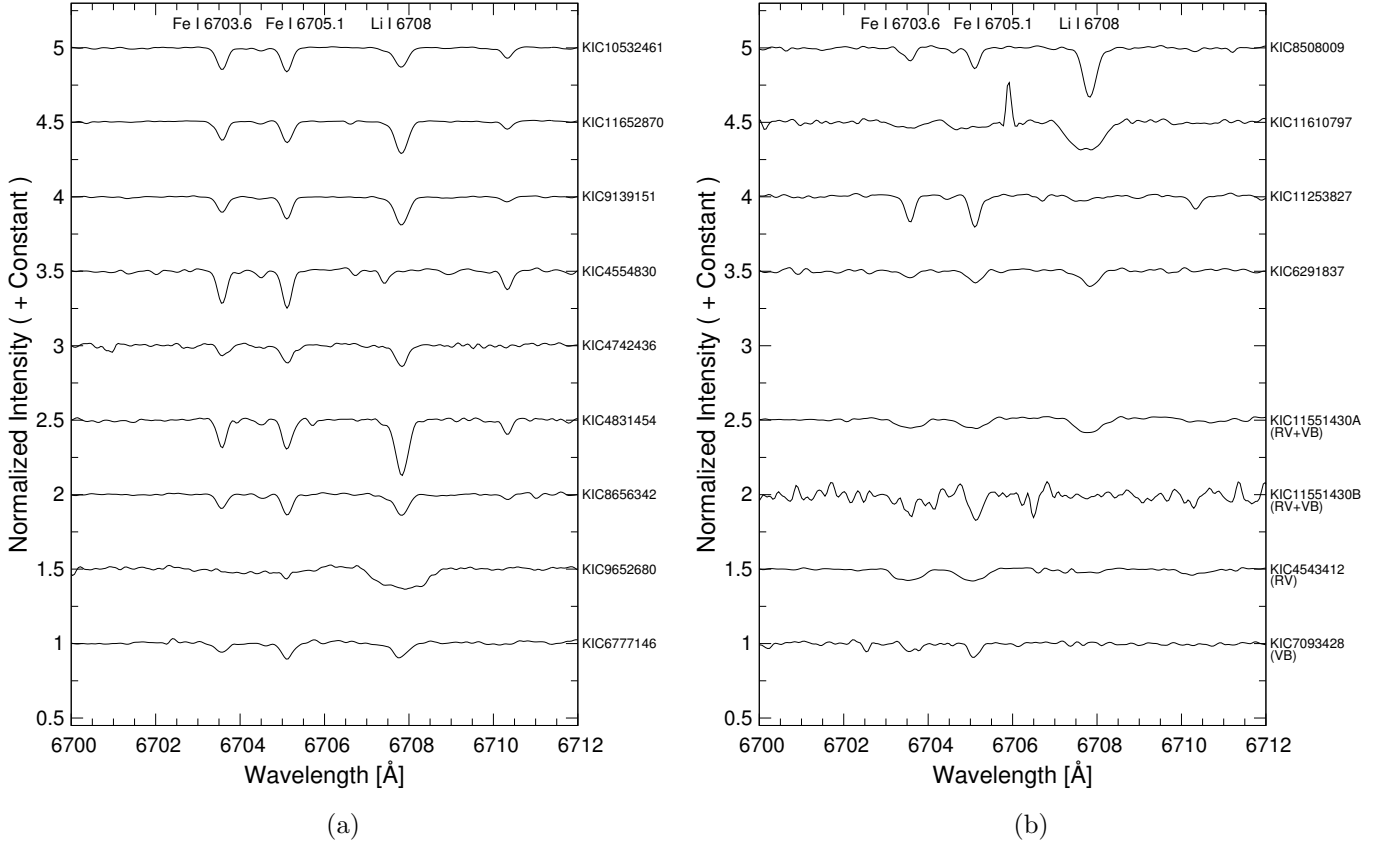


Figure 31. Spectra around Li I 6708 Å line. The wavelength scale of each spectrum is adjusted to the laboratory frame. In (a) and the upper part of (b), 13 “single” superflare stars that show no evidence of binarity are plotted. Co-added spectra are used here in case that the star was observed multiple times (See Table 2). In the bottom of (b), the spectra of binary stars that do not show any double-lined profiles are plotted for reference. As for KIC11551430A and KIC4543412 among them, which only show radial velocity shifts, the co-added spectra are used.

B. POTENTIAL DIFFERENCES BETWEEN THE RESULTS FORM THE *KEPLER* STARS AND THOSE FROM THE “REAL” SAMPLE OF FIELD STARS

As for Figure 15 in Section 5.4, we should note that there are many “inactive” stars with $A_{\text{spot}} < 10^{-3} A_{1/2\odot}$ ($A_{1/2\odot} \sim 3 \times 10^{22} \text{ cm}^2$: solar hemisphere). As shown in Table 9, approximately 76% ((49612–11594)/49612 = 37618/49212) of the solar-type stars are not plotted in Figure 15 since their brightness variation amplitude value is smaller than the detection limit. This also means that these $\sim 76\%$ “inactive” solar-type stars have no P_{rot} values in our sample, and this can cause biases when we discuss the relations of the superflare properties with the rotation period. For example, in Figure 14 (in Section 5.3), flare frequency distribution in each P_{rot} bin is calculated by using the number of the solar-type stars in each P_{rot} bin detected in McQuillan et al. (2014) (e.g., $N_P(P_{\text{rot}} < 5\text{d})$, $N_P(P_{\text{rot}} = 5\text{--}10\text{d})$, $N_P(P_{\text{rot}} = 10\text{--}20\text{d})$, and $N_P(P_{\text{rot}} \geq 20\text{d})$ in Table 9). However, it is possible that these N_P values does not show the actual P_{rot} distribution of field ordinary solar-type stars because of the following two reasons. (1) The above “inactive” stars with no P_{rot} values are expected to be dominated by old slowly-rotating stars, and the real number fraction of slowly-rotating stars to

Table 9. Number of stars that have P_{rot} and $\Delta F/F$ values (N_P) reported in McQuillan et al. (2014).

$T_{\text{eff,DR25}}$	$N_{\text{data}}^{\text{a}}$	$N_P(\text{all})^{\text{b}}$	$N_P(P_{\text{rot}} < 5\text{d})^{\text{c}}$	$N_P(P_{\text{rot}} = 5\text{--}10\text{d})^{\text{c}}$	$N_P(P_{\text{rot}} = 10\text{--}20\text{d})^{\text{c}}$	$N_P(P_{\text{rot}} \geq 20\text{d})^{\text{c}}$
5600–6000K	28329	5065	314 (6.2%)	786 (15.5%)	2325 (45.9%)	1640 (32.4%)
5100–5600K	20883	6529	175 (2.7%)	745 (11.4%)	2234 (34.2%)	3375 (51.7%)
5100–6000K	49212	11594	489 (4.2%)	1531 (13.2%)	4559 (39.3%)	5015 (43.3%)

^a Number of all newly classified solar-type stars among the stars in McQuillan et al. (2014), by using $T_{\text{eff,DR25}}$ and R_{Gaia} values

^b Number of stars that have P_{rot} and $\Delta F/F$ values reported in McQuillan et al. (2014).

^c Subgroups of N_P categorized with P_{rot} values. The numbers in the parentheses are the fractions of $N_P(P_{\text{rot}} < 5\text{d})$, $N_P(P_{\text{rot}} = 5\text{--}10\text{d})$, $N_P(P_{\text{rot}} = 10\text{--}20\text{d})$, and $N_P(P_{\text{rot}} \geq 20\text{d})$ to $N_P(\text{all})$, respectively.

Table 10. P_{rot} distribution of field ordinary solar-type stars estimated from the gyrochronological relation (cf. Equation (B14)).

$T_{\text{eff,DR25}}$	$N_{\text{star}}(P_{\text{rot}} < 5\text{d})/N_{\text{all}}$	$N_{\text{star}}(P_{\text{rot}} = 5\text{--}10\text{d})/N_{\text{all}}$	$N_{\text{star}}(P_{\text{rot}} = 10\text{--}20\text{d})/N_{\text{all}}$	$N_{\text{star}}(P_{\text{rot}} \geq 20\text{d})/N_{\text{all}}$
5800K	3% (<0.26 Gyr)	6% (0.26–0.89 Gyr)	21% (0.89–3.0 Gyr)	70% (≥ 3.0 Gyr)
5350K	2% (<0.17 Gyr)	4% (0.17–0.59 Gyr)	14% (0.59–2.0 Gyr)	80% (≥ 2.0 Gyr)

rapidly-rotating stars (e.g., the fraction of $N_P(P_{\text{rot}} \geq 20\text{d})$ to the other $N_P(P_{\text{rot}} < 5\text{d})$, $N_P(P_{\text{rot}} = 5\text{--}10\text{d})$, and $N_P(P_{\text{rot}} = 10\text{--}20\text{d})$ values) can become larger than the values used for the calculations in this study (e.g., Figure 14). (2) In a strict sense, it might be possible that P_{rot} and activity level distribution of *Kepler* stars can be (slightly) different from those of the field ordinary stars, because of the effects from the target selection (e.g., some active variables could be preferred in the Guest Observer programs).

In order to roughly evaluate the potential differences caused by the above points, we then roughly estimate the number fraction of solar-type stars in specific P_{rot} bins, by using the empirical gyrochronology relation (e.g., Mamajek & Hillenbrand 2008), which we have used in Maehara et al. (2017). The number of stars with $P_{\text{rot}} \geq P_0$ [$N_{\text{star}}(P_{\text{rot}} \geq P_0)$] can be estimated from the duration of the main-sequence phase (τ_{MS}), the gyrochronological age of the star [$t_{\text{gyro}}(P_0)$], and the total number of samples (N_{all}):

$$N_{\text{star}}(P_{\text{rot}} \geq P_0) = \left[1 - \frac{t_{\text{gyro}}(P_0)}{\tau_{\text{MS}}} \right] N_{\text{all}}, \quad (\text{B14})$$

assuming that the star formation rate around the *Kepler* field has been roughly constant over τ_{MS} . Using Equations (12)–(14) of Mamajek & Hillenbrand (2008), we roughly estimated the age values (t_{gyro}) of solar-type stars with $T_{\text{eff}} \sim 5800$ & 5350 K ($B - V \sim 0.63$ & 0.78 from Equation (2) of Valenti & Fischer 2005) and $P_{\text{rot}} \sim 5$, 10, & 20 days, as listed in the parentheses in Table 10. Using these t_{gyro} values and Equation (B14), we estimated the number fraction of stars with $P_{\text{rot}} < 5\text{d}$, $5\text{--}10\text{d}$, $10\text{--}20\text{d}$, and $\geq 20\text{d}$ as listed in Table 10. As a result, there are differences between the number fractions of slowly/rapidly-rotating stars in the *Kepler* sample from McQuillan et al. (2014) (Table 9)

and those estimated from the gyrochronology relation (Table 10). For example, the number fraction of $P_{\text{rot}} \geq 20\text{d}$ among all the sample stars with $T_{\text{eff}} = 5600\text{--}6000\text{ K}$ has a roughly factor two difference: $N_P(P_{\text{rot}} \geq 20\text{d})/N_P(\text{all}) \sim 32\%$ (Table 9) and $N_{\text{star}}(P_{\text{rot}} \geq 20\text{d})/N_{\text{all}} \sim 70\%$ (Table 10). This means that the flare frequency value of $T_{\text{eff}} = 5600\text{--}6000\text{ K}$ and $P_{\text{rot}} \geq 20\text{ days}$ in Figure 14 can become factor two smaller than the real value. We must note these potential errors of our study, and the exact values of the flare frequency estimated from our analyses should be treated carefully with cautions. However, the overall dependences (e.g., the results that flare frequency clearly depends on the rotation period) does not change and the differences are much smaller than one order of magnitude. Moreover, the estimates from the gyrochronology can also include several errors. One example is that the age–rotation relation (gyrochronology relation) of young (e.g., $t \lesssim 0.5\text{--}0.6\text{ Gyr}$) and old (e.g., $t > 5.0\text{ Gyr}$) solar-type stars can have a large scatter (e.g., Soderblom et al. 1993; Ayres 1997; Tu et al. 2015) and breakdown (van Saders et al. 2016; Metcalfe & Egeland 2018), respectively, as we have also mentioned in Section 5.3. We also assumed that the star formation rate around the *Kepler* field has been roughly constant over τ_{MS} in the above estimation, but this assumption is not necessarily correct. Because of these points, more investigations on the above potential differences (as large as factor two or three) between the results from the *Kepler* stars and those from the “real” sample of field stars are beyond the scope of this paper, and we expect future studies using new data (e.g., *TESS* data mentioned in Section 6.3). We note again here that we should keep in mind these potential errors when discussing the relation of superflare frequency with the rotation period (e.g., Figure 14 in Section 5.3 and Figures 16&17 in Section 5.5).

REFERENCES

- Aarnio, A. N., Matt, S. P., & Stassun, K. G. 2012, ApJ, 760, 9
- Airapetian, V. S., Glocer, A., Gronoff, G., Hébrard, E., & Danchi, W. 2016, Nature Geoscience, 9, 452
- Alonso, A., Arribas, S., & Martinez-Roger, C. 1996, A&A, 313, 873
- Aschwanden, M. J., Tarbell, T. D., Nightingale, R. W., et al. 2000, ApJ, 535, 1047
- Atri, D. 2017, MNRAS, 465, L34
- Aulanier, G., Démoulin, P., Schrijver, C. J., et al. 2013, A&A, 549, A66
- Ayres, T. R. 1997, J. Geophys. Res., 102, 1641
- Baliunas, S. L., Donahue, R. A., Soon, W. H., et al. 1995, ApJ, 438, 269
- Balona, L. A. 2015, MNRAS, 447, 2714
- Bastien, F. A., Stassun, K. G., Basri, G., & Pepper, J. 2016, ApJ, 818, 43
- Benz, A. O., & Güdel, M. 2010, ARA&A, 48, 241
- Benomar, O., Bazot, M., Nielsen, M. B., et al. 2018, Science, 361, 1231
- Berger, T. A., Huber, D., Gaidos, E., & van Saders, J. L. 2018, ApJ, 866, 99
- Berdyugina, S. V. 2005, Living Reviews in Solar Physics, 2, 8
- Bogdan, T. J., Gilman, P. A., Lerche, I., & Howard, R. 1988, ApJ, 327, 451
- Bressan, A., Marigo, P., Girardi, L., et al. 2012, MNRAS, 427, 127
- Brown, T. M., Latham, D. W., Everett, M. E., & Esquerdo, G. A. 2011, AJ, 142, 112
- Candelaresi, S., Hillier, A., Maehara, H., Brandenburg, A., & Shibata, K. 2014, ApJ, 792, 67
- Chang, H.-Y., Lin, C.-L., Ip, W.-H., et al. 2018, ApJ, 867, 78
- Crosby, N. B., Aschwanden, M. J., & Dennis, B. R. 1993, SoPh, 143, 275
- Crosley, M. K., & Osten, R. A. 2018, ApJ, 856, 39
- Davenport, J. R. A. 2016, ApJ, 829, 23
- Doyle, L., Ramsay, G., Doyle, J. G., Wu, K., & Scullion, E. 2018, MNRAS, 480, 2153
- Duncan, D. K., Vaughan, A. H., Wilson, O. C., et al. 1991, ApJS, 76, 383
- Eastwood, J. P., Biffis, E., Hapgood, M. A., 2017, Risk Analysis, 37, 2 (doi: 10.1111/risa.12765)

- Emslie, A. G., Dennis, B. R., Shih, A. Y., et al. 2012, *ApJ*, 759, 71
- Gershberg, R. E. 2005, Solar-Type Activity in Main-Sequence Stars (Berlin: Springer)
- Giles, H. A. C., Collier Cameron, A., & Haywood, R. D. 2017, *MNRAS*, 472, 1618
- Gizis, J. E., Burgasser, A. J., Berger, E., et al. 2013, *ApJ*, 779, 172
- Gray, D. F. 2005, The Observation and Analysis of Stellar Photospheres (3rd ed.; UK: Cambridge University Press)
- Güdel, M. 2007, *Living Reviews in Solar Physics*, 4, 3
- Hall, J. C. 2008, *Living Reviews in Solar Physics*, 5, 2
- Harra, L. K., Schrijver, C. J., Janvier, M., et al. 2016, *SoPh*, 291, 1761
- Hawley, S. L., Walkowicz, L. M., Allred, J. C., & Valenti, J. A. 2007, *PASP*, 119, 67
- Hawley, S. L., Davenport, J. R. A., Kowalski, A. F., et al. 2014, *ApJ*, 797, 121
- Hayakawa, H., Iwahashi, K., Ebihara, Y., et al. 2017, *ApJL*, 850, L31
- Hayakawa, H., Tamazawa, H., Uchiyama, Y., et al. 2017, *SoPh*, 292, 12
- Heinzel, P., & Shibata, K. 2018, *ApJ*, 859, 143
- Hirano, T., Sanchis-Ojeda, R., Takeda, Y., et al. 2012, *ApJ*, 756, 66
- Honda, S., Notsu, Y., Maehara, H., et al. 2015, *PASJ*, 67, 85
- Honda, S., Notsu, Y., Namekata, K., et al. 2018, *PASJ*, 70, 62
- Houdebine, E. R., Foing, B. H., Doyle, J. G., & Rodono, M. 1993, *A&A*, 274, 245
- Huber, D., Silva Aguirre, V., Matthews, J. M., et al. 2014, *ApJS*, 211, 2
- Hudson, H. S. 2015, *Journal of Physics Conference Series*, 632, 012058
- Isaacson, H., & Fischer, D. 2010, *ApJ*, 725, 875
- Jackman, J. A. G., Wheatley, P. J., Pugh, C. E., et al. 2018, *MNRAS*, 477, 4655
- Karoff, C., Metcalfe, T. S., Chaplin, W. J., et al. 2013, *MNRAS*, 433, 3227
- Karoff, C., Knudsen, M. F., De Cat, P., et al. 2016, *Nature Communications*, 7, 11058
- Katsova, M. M., Kitchatinov, L. L., Livshits, M. A., et al. 2018, *Astronomy Reports*, 62, 72
- Koch, D. G., Borucki, W. J., Basri, G., et al. 2010, *ApJL*, 713, L79
- Kowalski, A. F., Hawley, S. L., Holtzman, J. A., Wisniewski, J. P., & Hilton, E. J. 2010, *ApJL*, 714, L98
- Kowalski, A. F., & Allred, J. C. 2018, *ApJ*, 852, 61
- Kurucz, R. L. 1993, Kurucz CD-ROM No. 13, Atlas 9 Stellar Atmo-sphere Programs and 2 km/s Grid (Cambridge, MA: Harvard-Smithsonian Center for Astrophysics)¹⁹
- Leitzinger, M., Odert, P., Greimel, R., et al. 2014, *MNRAS*, 443, 898
- Lingam, M., & Loeb, A. 2017, *ApJ*, 848, 41
- Linsky, J. L., Worden, S. P., McClintock, W., & Robertson, R. M. 1979a, *ApJS*, 41, 47
- Linsky, J. L., Hunten, D. M., Sowell, R., Glackin, D. L., & Kelch, W. L. 1979b, *ApJS*, 41, 481
- Lockwood, G. W., Skiff, B. A., Henry, G. W., et al. 2007, *ApJS*, 171, 260
- Maehara, H., Shibayama, T., Notsu, S., et al. 2012, *Nature*, 485, 478
- Maehara, H., Shibayama, T., Notsu, Y., et al. 2015, *Earth, Planets, and Space*, 67, 59
- Maehara, H., Notsu, Y., Notsu, S., et al. 2017, *PASJ*, 69, 41
- Mamajek, E. E., & Hillenbrand, L. A. 2008, *ApJ*, 687, 1264
- Marigo, P., Girardi, L., Bressan, A., et al. 2017, *ApJ*, 835, 77
- Mathur, S., Huber, D., Batalha, N. M., et al. 2017, *ApJS*, 229, 30 (ERRATUM: 2018, *ApJS*, 234, 43)
- McLaughlin, J. A., Nakariakov, V. M., Dominique, M., Jelínek, P., & Takasao, S. 2018, *SSRv*, 214, 45
- McQuillan, A., Mazeh, T., & Aigrain, S. 2014, *ApJS*, 211, 24
- Metcalfe, T. S., & Egeland, R. 2018, *ApJ*, 871, 39
- Mittag, M., Schmitt, J. H. M. M., & Schröder, K.-P. 2013, *A&A*, 549, A117
- Miyake, F., Nagaya, K., Masuda, K., & Nakamura, T. 2012, *Nature*, 486, 240
- Miyake, F., Masuda, K., & Nakamura, T. 2013, *Nature Communications*, 4, 1748
- Morris, B. M., Hawley, S. L., Hebb, L., et al. 2017, *ApJ*, 848, 58
- Morris, B. M., Curtis, J. L., Douglas, S. T., et al. 2018, *AJ*, 156, 203

¹⁹ <http://kurucz.harvard.edu/programs.html>

- Moschou, S.-P., Drake, J. J., Cohen, O., Alvarado-Gomez, J. D., & Garraffo, C. 2017, *ApJ*, 850, 191
- Namekata, K., Sakaue, T., Watanabe, K., et al. 2017, *ApJ*, 851, 91
- Namekata, K., Maehara, H., Notsu, Y., et al. 2019, *ApJ*, 871, 187
- Neupert, W. M. 1968, *ApJL*, 153, L59
- Nogami, D., Notsu, Y., Honda, S., et al. 2014, *PASJ*, 66, L4
- Notsu, S., Honda, S., Notsu, Y., et al. 2013a, *PASJ*, 65, 112
- Notsu, Y., Shibayama, T., Maehara, H., et al. 2013b, *ApJ*, 771, 127
- Notsu, Y., Honda, S., Maehara, H., et al. 2015a, *PASJ*, 67, 32
- Notsu, Y., Honda, S., Maehara, H., et al. 2015b, *PASJ*, 67, 33
- Notsu, Y., Honda, S., Maehara, H., et al. 2017, *PASJ*, 69, 12
- Noyes, R. W., Hartmann, L. W., Baliunas, S. L., Duncan, D. K., & Vaughan, A. H. 1984, *ApJ*, 279, 763
- Osten, R. A., & Wolk, S. J. 2015, *ApJ*, 809, 79
- Osten, R. A., Kowalski, A., Drake, S. A., et al. 2016, *ApJ*, 832, 174
- Paudel, R. R., Gizis, J. E., Mullan, D. J., et al. 2018, *ApJ*, 861, 76
- Perryman, M. A. C., Brown, A. G. A., Lebreton, Y., et al. 1998, *A&A*, 331, 81
- Pugh, C. E., Armstrong, D. J., Nakariakov, V. M., & Broomhall, A.-M. 2016, *MNRAS*, 459, 3659
- Pye, J. P., Rosen, S., Fyfe, D., & Schröder, A. C. 2015, *A&A*, 581, A28
- Rauer, H., Catala, C., Aerts, C., et al. 2014, *Experimental Astronomy*, 38, 249
- Reid, I. N., & Hawley, S. L. 2005, *New Light on Dark Stars : Red Dwarfs, Low-Mass Stars, Brown Stars* (Chichester: Praxis Publishing)
- Rich, E. A., Wisniewski, J. P., McElwain, M. W., et al. 2017, *MNRAS*, 472, 1736
- Riley, P., Baker, D., Liu, Y. D., et al. 2018, *SSRv*, 214, 21
- Pinsonneault, M. H., An, D., Molenda-Żakowicz, J., et al. 2012, *ApJS*, 199, 30
- Ramsay, G., & Doyle, J. G. 2015, *MNRAS*, 449, 3015
- Ricker, G. R., Winn, J. N., Vanderspek, R., et al. 2015, *Journal of Astronomical Telescopes, Instruments, and Systems*, 1, 014003
- Roettenbacher, R. M., & Vida, K. 2018, *ApJ*, 868, 3
- Royal Academy of Engineering, 2013, *Extreme Space Weather: Impacts on Engineered Systems and Infrastructure* (London: Royal Academy of Engineering) <https://www.raeng.org.uk/publications/reports/space-weather-full-report>
- Sammis, I., Tang, F., & Zirin, H. 2000, *ApJ*, 540, 583
- Schaefer, B. E., King, J. R., & Deliyannis, C. P. 2000, *ApJ*, 529, 1026
- Schmieder, B. 2018, *Journal of Atmospheric and Solar-Terrestrial Physics*, 180, 46
- Schrijver, C. J. 1987, *A&A*, 172, 111
- Schrijver, C. J., Cote, J., Zwaan, C., & Saar, S. H. 1989, *ApJ*, 337, 964
- Schrijver, C. J., Beer, J., Baltensperger, U., et al. 2012, *Journal of Geophysical Research (Space Physics)*, 117, A08103
- Schrijver, C. J. 2015, *Space Weather*, 13, 524
- Segura, A., Walkowicz, L. M., Meadows, V., Kasting, J., & Hawley, S. 2010, *Astrobiology*, 10, 751
- Shibata, K., & Magara, T. 2011, *Living Reviews in Solar Physics*, 8, 6
- Shibata, K., Isobe, H., Hillier, A., et al. 2013, *PASJ*, 65, 49
- Shibayama, T., Maehara, H., Notsu, S., et al. 2013, *ApJS*, 209, 5
- Shimizu, T. 1995, *PASJ*, 47, 251
- Skumanich, A. 1972, *ApJ*, 171, 565
- Soderblom, D. R., Stauffer, J. R., MacGregor, K. B., & Jones, B. F. 1993, *ApJ*, 409, 624
- Takahashi, T., Mizuno, Y., & Shibata, K. 2016, *ApJL*, 833, L8
- Takeda, Y. 1995, *PASJ*, 47, 287
- Takeda, Y., Ohkubo, M., & Sadakane, K. 2002, *PASJ*, 54, 451
- Takeda, Y., & Kawanomoto, S. 2005, *PASJ*, 57, 45
- Takeda, Y., Ohkubo, M., Sato, B., Kambe, E., & Sadakane, K. 2005, *PASJ*, 57, 27
- Takeda, Y., Sato, B., & Murata, D. 2008, *PASJ*, 60, 781
- Takeda, Y., Honda, S., Kawanomoto, S., Ando, H., & Sakurai, T. 2010, *A&A*, 515, A93
- Takeda, Y., Tajitsu, A., Honda, S., et al. 2012, *PASJ*, 64, 130
- Takeda, Y., Honda, S., Ohnishi, T., et al. 2013, *PASJ*, 65, 53

- Thompson, S. E., et al. 2015, *Kepler* Data Release 24 Notes (KSCI-19064-002), (Moffett Field, CA: NASA Ames Research Center)
- Toriumi, S., Schrijver, C. J., Harra, L. K., Hudson, H., & Nagashima, K. 2017, ApJ, 834, 56
- Tsurutani, B. T., & Lakhina, G. S. 2014, Geophys. Res. Lett., 41, 287
- Tu, L., Johnstone, C. P., Güdel, M., & Lammer, H. 2015, A&A, 577, L3
- Usoskin, I. G. 2017, Living Reviews in Solar Physics, 14, 3
- Van Doorsselaere, T., Shariati, H., & Debosscher, J. 2017, ApJS, 232, 26
- van Saders, J. L., Ceillier, T., Metcalfe, T. S., et al. 2016, Nature, 529, 181
- Valenti, J. A., & Fischer, D. A. 2005, ApJS, 159, 141
- Vaughan, A. H., Preston, G. W., & Wilson, O. C. 1978, PASP, 90, 267
- Vida, K., Kriskovics, L., Oláh, K., et al. 2016, A&A, 590, A11
- Walkowicz, L. M., Basri, G., Batalha, N., et al. 2011, AJ, 141, 50
- Wang, S.-i., Hildebrand, R. H., Hobbs, L. M., et al. 2003, Proc. SPIE, 4841, 1145
- Wichmann, R., Fuhrmeister, B., Wolter, U., & Nagel, E. 2014, A&A, 567, A36
- Wilson, O. C. 1978, ApJ, 226, 379
- Wright, N. J., Drake, J. J., Mamajek, E. E., & Henry, G. W. 2011, ApJ, 743, 48
- Wu, C.-J., Ip, W.-H., & Huang, L.-C. 2015, ApJ, 798, 92
- Yang, H., Liu, J., Gao, Q., et al. 2017, ApJ, 849, 36
- Ziegler, C., Law, N. M., Baranec, C., et al. 2018, AJ, 155, 161